# Shape Memory Alloy Cellular Solids

by

**Petros A. Michailidis**

**A dissertation submitted in partial fulfillment**
**of the requirements for the degree of**
**Doctor of Philosophy**
**(Aerospace Engineering)**
**in The University of Michigan**
**2009**

**Doctoral Committee:**

**Associate Professor John A. Shaw, Co-Chair**
**Professor Nicolas Triantafyllidis, Co-Chair**
**Assistant Professor Samantha Daly**
**Professor David S. Grummon**

# Acknowledgements

I wish to thank all who made this work possible.... Professors Triantafyllidis and Shaw, my colleagues Jesse Thomas, Chris Churchill, Ben Reedlunn, the staff at the Department of Aerospace Engineering, my friends and relatives, and people who funded the project.

# Table of Contents

**Chapter**

**Appendix**

# List of Figures

**Figure**

# List of Tables

**Table**

## Chapter I

# Introduction

Low density cellular solids, particularly metallic ones, are widely used in engineering applications [3, 10], since they can be designed to have high stiffness-to-mass ratios and desirable energy absorption characteristics. Cellular structures made from shape memory alloys (SMA's) are especially interesting for their potential to deliver superelasticity and shape memory in a light-weight material. While porous forms of NiTi (Nitinol) have been produced [11, 19, 20], the difficulty of joining Nitinol to itself has historically prevented the fabrication of NiTi-based cellular honeycombs with useful adaptive properties. Other attempts to fabricate SMA honeycombs have been done by mechanical fasteners or gluing [14, 23], and a few modeling and design studies, focussing mostly on stiffness and poisson ratio, have been performed [7].

An enabling metallurgical bonding method was discovered recently, however, by [12], which led to the construction and testing of the first NiTi honeycomb specimens showing robust properties. Two different cell geometries, hexagonal and wavy-corrugated, were produced by shape setting NiTi strips into corrugated forms, bonding them together at high temperature using a Niobium-based braze, and then heat-treating the resulting structures at moderate temperature. Compressive isothermal experiments on the specimens exhibited superelasticity with over macroscopic 50 % strain recovery [26], and non-isothermal shape memory experiments demonstrated stress-free recovery of similar macroscopic strains [29].

A low-density cellular architecture made of an SMA has several advantages. The maximum tensile strain recovery of a monolithic Nitinol polycrystal is in the range of 5 to 8 % in the low-cycle limit and less than 2.5 % for high cycle loading. These limits can be substantially amplified structurally by exploiting bending of the thin walls in an open cell topology. Moreover, thermal inertia, which tends to dominate the response time of SMA actuators and cause hypersensitive superelastic rate-dependencies (see, for example, [18, 27, 28]), scales with the material's volume-to-surface ratio and can thus be potentially reduced by adopting a low-density architecture.

Compared to conventional honeycombs, SMA honeycombs offer potentially new modes of use. The enhanced shape memory effect could be used in an active mode in thermal actuators, where the very large force capability of monolithic SMAs has been traded for amplified displacement capability. When used as energy absorbers, most metallic honeycombs are used as sacrificial elements that are thrown away after one-time use. With SMA honeycombs, however, the enhanced superelasticity can be used as reusable energy absorbers under overload conditions. This could be a more cost effective alternative if many overload events (yet still relatively rare) are expected during the life of the structure to be protected. In addition, this could be important for shape critical components, such as airfoils or control surfaces of aircraft, where an overload condition results in a tolerable momentary deviation from the design configuration, but without permanent deformation that would be otherwise catastrophic in flight.

This work is aimed at modeling SMA honeycombs under compressive loads, considering both the superelasticity and the shape memory effect. To our knowledge these are the FIRST simulations of SMA honeycombs to include large deformation behavior, investigate stability aspects, and guide the design of potential recoverable energy absorbers or thermal actuators. This work will focus on quasi-static compression in one load orientation (the one used in experiments in [26])

This thesis is organized as follows. In Chapter II a superelastic honeycomb with a hexagonal unit cell is investigated. A thorough investigation of the influence of the different material properties and the presence of imperfections in the response and the stability of a finite and infinite honeycomb is performed. All of the work presented in this chapter has been published in [22].

In Chapter III, the modeling capabilities developed in Chapter II are used to perform a design study. A family of generalized hexagonal cells is studied and their kinetic energy absorption capability is computed, constrained to operate within recoverable strain limits to ensure reusability. Finally, in Chapter IV, a thermo-mechanical SMA material model is presented that can be used to simulate the shape memory effect in an SMA honeycomb, along with some analysis and implementation details of it. A few examples are presented to exhibit it's behavior and the potential of using such a honeycomb as an actuator.

# Chapter II

# Superelastic Honeycombs

## 2.1 Introduction

The goal of the present chapter is to explore in detail the isothermal, superelastic response of a hexagonal unit cell, to investigate the instabilities of the overall honeycomb structure under compressive loading-unloading, and to study the influence of different material properties and imperfections at various scales.

The presentation of the work is outlined as follows. Section 2.2 presents the kinematic structural model, the material model, and the methods used to establish the stability of the infinite (using Bloch waves) and finite (perfect and imperfect) honeycombs. Section 2.3 describes the numerical approach and material parameters used. Simulation results are presented in Section 2.4, which investigates the choice of constitutive model parameters and then demonstrates the responses of infinite-perfect, finite-perfect and finite geometrically imperfect honeycomb structures. The section ends with the selection of material parameters for a finite element simulation of an experiment on a fabricated SMA honeycomb.

## 2.2 Modeling

The structural and material models employed in numerical simulations of in-plane compression are presented in this section. The first part presents the geometry of the honeycomb structure and the kinematics of cell wall deformation. The second part describes the constitutive model for isothermal, superelastic deformations. The last part describes the methods and criteria to determine stability of infinite-perfect, finite-perfect and finite-imperfect honeycomb structures.

### 2.2.1 Kinematics

A typical planar section of a perfectly periodic honeycomb, consisting of a regular hexagonal lattice, is shown in the undeformed (reference) configuration in Figure 2.1(a). The cell walls have thickness $t$ (except for $2t$ along the $X_1$ direction) and length $L$. A cutout of a periodic unit cell is also shown in the figure, which is used for stability calculations discussed later in Section 2.2.3. In all simulations of this chapter the aspect ratio of cell wall thickness to length was fixed at $t/L = 1/30$, corresponding to one of the hexagonal honeycombs presented in [26]. Upon in-plane mechanical compression (for now, we consider loading along the $X_2$-axis), the cell walls deform primarily through bending with some axial loading, so each ligament is idealized as a small strain, nonlinear beam capable of sustaining arbitrarily large displacements and rotations. The structural model has already been presented elsewhere (see [33]), but for completeness, a brief description is included below.

Consider an initially straight beam of length $l$ and thickness $t$ as shown in Figure 2.1(b)

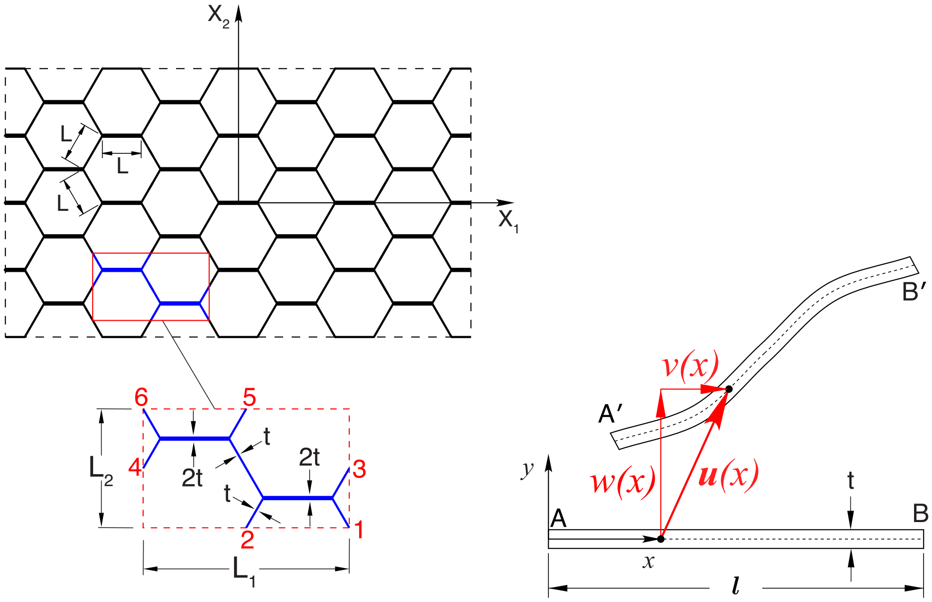

(a)

(b)

Figure 2.1: (a) Reference configuration geometry and global coordinates $(X_1, X_2)$ of the perfect SMA honeycomb. The honeycomb is compressed along the $X_2$ direction. The magnified view is the periodic unit cell used in stability calculations for the infinite-perfect honeycomb. (b) Kinematics of cell-wall deformations with respect to local coordinates $(x, y)$, showing displacements $(v, w)$ between reference configuration $(AB)$ and current configuration $(A'B')$.

(with unit out-of-plane width). During loading, a material point initially at local axial coordinate $x$ on the beam's undeformed mid-line (dotted line) moves to a new position on the deformed mid-line by displacements $v(x)$ and $w(x)$ along the local tangential $(x)$ and normal $(y)$ directions of the initial configuration, respectively. By adopting the classic Bernoulli-Euler assumption where cross-sections normal to the undeformed mid-line remain normal in its deformed counterpart and undergo small strain extension, the axial strain of a material point with initial local coordinates $(x, y)$ is given by

$$\varepsilon(x, y) = e(x) + y\kappa(x), \tag{2.1}$$

where the mid-line axial strain $e(x)$ and the bending curvature $\kappa(x)$ are expressed in terms of the displacements $v(x)$ and $w(x)$ by

$$
\begin{aligned}
e &= \left[(1+\frac{dv}{dx})^2 + (\frac{dw}{dx})^2\right]^{1/2} - 1, \\
\kappa &= \left[\frac{dw}{dx}\frac{d^2v}{dx^2} - (1+\frac{dv}{dx})\frac{d^2w}{dx^2}\right] \Big/ \left[(1+\frac{dv}{dx})^2 + (\frac{dw}{dx})^2\right].
\end{aligned} \tag{2.2}
$$

The contribution of internal virtual work from each ligament in the weak form of the equilibrium equations is given by

$$
\delta W_l^I = \int_0^l (N\delta e + M\delta\kappa)\,dx; \quad \text{with } N \equiv \int_{-t/2}^{t/2} \sigma\,dy, \quad \text{and } M \equiv \int_{-t/2}^{t/2} \sigma y\,dy, \tag{2.3}
$$

where $N(x)$ and $M(x)$ are the axial force and bending moment resultants, respectively, and $\sigma(x, y)$ is the local axial stress in the cell wall. The Euler-Lagrange equations corresponding to (2.1)–(2.3) have been shown to coincide with the exact equilibrium equations of the beam in the current configuration, thus making this structural theory a consistent one (the interested reader is referred to [31] for a detailed discussion).

### 2.2.2 Constitutive Model

Since only isothermal deformations of the SMA honeycomb are presently considered (consistent with slow superelastic loading-unloading), a small strain, one-dimensional, rate-independent, isothermal, hysteretic, constitutive model is described below. As is common in SMA modeling, an internal variable formulation is used to describe the extent of stress-induced phase transformation. The uniaxial constitutive model employed here has only one internal variable $\xi \in [0, 1]$, which represents the martensite phase fraction at a material point $(x, y)$. Pure austenite ($A$) and pure martensite, either tensile $M^+$ or compressive $M^-$, are represented by $\xi = 0$ and $\xi = 1$, respectively[1]. We note that the constitutive model has similarities to a conventional elasto-plastic constitutive law, but it has important differences in that the internal field variable is bounded in our case, unlike plasticity, and the unloading behavior is quite different, leading to superelasticity in our case. Both differences lead to interesting stability changes in the honeycomb structure, as will be shown in Section 2.4, where stability can be lost but then regained as phase transformation saturates in either direction. Furthermore, this model can be readily generalized to include temperature-induced transformations and consequent shape memory behavior, although this is left for future work.

In its simplest form the constitutive law for the local stress, $\sigma(x, y)$, is

$$\sigma = \begin{cases} E(\varepsilon - \beta^+ \xi), & \text{for } \varepsilon \geq 0 \\ E(\varepsilon - \beta^- \xi), & \text{for } \varepsilon < 0 \end{cases} \tag{2.4}$$

where $\varepsilon(x, y)$ is the local fiber strain corresponding to eq. (2.1) and $\xi(x, y)$ is the local fiber martensite phase fraction. The remaining parameters are material constants, in which, $E$ is the effective uniaxial elastic modulus[2] (phase independent, here) and $\beta^+$ and $\beta^-$ are the

---

[1] We assume that the temperature is sufficiently high such that $M^-$ and $M^+$ never exist simultaneously at any material point.

[2] We have assumed the local stress to be purely uniaxial, so $E$ is to be interpreted as the Young's modulus if the ligament out-of-plane depth is small. If the ligament depth cannot be neglected, as is the case for the actual honeycomb specimen considered later, it can alternatively be interpreted approximately as the modulus for cylindrical plate bending, $E/(1 - \nu^2)$, consistent with our 2-D context. In any case, the results in this work are presented in dimensionless form where stresses have been normalized by $E$.

respective transformation strains (material constants) in tension and compression[3]. Allowing different transformation behavior in compression vs. tension provides the flexibility to capture tension-compression asymmetry, which is a known phenomenon in textured SMA polycrystals [8]. For elastic loading-unloading the internal variable $\xi$ remains constant, i.e., $\dot{\xi} = 0$ (where $\dot{(\ )}$ denotes the time derivative $d(\ )/dt$). The onset of phase transformation during mechanical loading from $A \rightarrow M$ occurs at a nucleation strain of $\varepsilon_n^+$ in tension ($\varepsilon > 0$ and $\dot{\varepsilon} > 0$) or $\varepsilon_n^-$ in compression ($\varepsilon < 0$ and $\dot{\varepsilon} < 0$). Phase transformation evolves along two-phase stress paths (see Figure 2.2) according to

$$\sigma = \begin{cases} \hat{\sigma}_l^+(\xi), & \text{for } A \rightarrow M^+ \\ \hat{\sigma}_u^+(\xi), & \text{for } A \leftarrow M^+ \\ \hat{\sigma}_u^-(\xi), & \text{for } A \leftarrow M^- \\ \hat{\sigma}_l^-(\xi), & \text{for } A \rightarrow M^-, \end{cases} \tag{2.5}$$

where subscripts $l$ and $u$ refer to "loading" and "unloading", respectively, in the sense that "loading" is associated with the direction $A \rightarrow M$ (either $M^+$ or $M^-$). Phase transformation hysteresis is parameterized with material constants $\Delta\sigma_A^+$, $\Delta\sigma_M^+$, $\Delta\sigma_A^-$, $\Delta\sigma_M^-$. Loading and unloading paths are related by

$$\begin{aligned} \hat{\sigma}_l^+(\xi) &= \hat{\sigma}_u^+(\xi) + (1-\xi)\Delta\sigma_A^+ + \xi\Delta\sigma_M^+ \\ \hat{\sigma}_u^-(\xi) &= \hat{\sigma}_l^-(\xi) + (1-\xi)\Delta\sigma_A^- + \xi\Delta\sigma_M^- \end{aligned} \tag{2.6}$$

---

[3] From here on, quantities associated with the tensile or compressive behavior are denoted by a $+$ or $-$ superscript, respectively. Absence of the $+$ or $-$ superscript means that the parameter applies to both tensile and compressive parts of the constitutive behavior.

where $\Delta\sigma_M^+$ $(\Delta\sigma_M^-)$ is related to $\Delta\sigma_A^+$ $(\Delta\sigma_A^-)$ and the loading, unloading tangent moduli in tension (compression) $E_l^+$, $E_u^+$ $(E_l^-, E_u^-)$ by

$$\begin{aligned} \Delta\sigma_M^+ &= \Delta\sigma_A^+ + \beta^+ \left[1/(1/E_l^+ - 1/E) - 1/(1/E_u^+ - 1/E)\right] \\ \Delta\sigma_M^- &= \Delta\sigma_A^- + \beta^- \left[1/(1/E_l^- - 1/E) - 1/(1/E_u^- - 1/E)\right] \end{aligned} \tag{2.7}$$

For simplicity the functions $\hat{\sigma}(\xi)$, are chosen such that the tangent moduli during the loading $(E_l)$ or unloading $(E_u)$ phase transformation are material constants[4]. Consequently

$$\dot{\xi} = \begin{cases} \dfrac{E - E_l^+}{E}\dfrac{\dot{\varepsilon}}{\beta^+} : & \text{if} \quad \dot{\varepsilon} > 0, \quad \sigma = \hat{\sigma}_l^+(\xi), \quad \text{and } \xi < 1 \\ \dfrac{E - E_u^+}{E}\dfrac{\dot{\varepsilon}}{\beta^+} : & \text{if} \quad \dot{\varepsilon} < 0, \quad \sigma = \hat{\sigma}_u^+(\xi), \quad \text{and } \xi > 0 \\ \dfrac{E - E_l^-}{E}\dfrac{\dot{\varepsilon}}{\beta^-} : & \text{if} \quad \dot{\varepsilon} < 0, \quad \sigma = \hat{\sigma}_l^-(\xi), \quad \text{and } \xi < 1 \\ \dfrac{E - E_u^-}{E}\dfrac{\dot{\varepsilon}}{\beta^-} : & \text{if} \quad \dot{\varepsilon} > 0, \quad \sigma = \hat{\sigma}_u^-(\xi), \quad \text{and } \xi > 0 \end{cases} \tag{2.8}$$

All the constants involved in the definition of the constitutive law are shown in Figure 2.2. Specific values of the material constants will be chosen in Section 2.4.

---

[4] When $E_u^+ = E_l^+$ $(E_u^- = E_l^-)$ the corresponding tangent modulus during phase transformation is denoted by $E_t^+$ $(E_t^-)$.

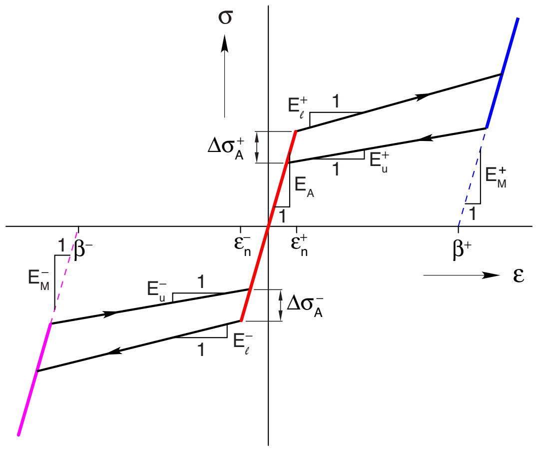

Figure 2.2: Uniaxial superelastic response of SMA material and associated constitutive parameters. Subscripts $A$ or $M$ refer to Austenite or Martensite while superscripts $(\cdot)^+$ or $(\cdot)^-$ indicate association with tensile or compressive response, respectively.

### 2.2.3 Stability of the SMA Honeycomb Structure

A deep understanding of the behavior of the SMA honeycomb structure requires the investigation of its stability. Specifically, we seek the stability of the principal solutions of the infinite and finite perfect structures, both having equilibrium solutions where all unit cells undergo identical (periodic) deformations. The stability of the former is studied with the help of Bloch wave representation theory while the stability of the latter includes the effects of boundary conditions on the finite structure. Both are key ingredients to help explain the behavior of the actual finite, imperfect SMA structure.

Based on the constitutive model formulated, we are interested in the stability of the principal equilibrium path of a rate-independent, yet path-dependent, "elastoplastic" solid. Following [15], the stability of the rate-independent solid considered here is governed by the criterion of positive definiteness of the quadratic functional [5,6]

$$\varphi(\lambda, \Delta \boldsymbol{u}) = \Delta \boldsymbol{u}^* \bullet K(\lambda) \bullet \Delta \boldsymbol{u}, \tag{2.9}$$

where $\boldsymbol{K}$ is the incremental stiffness matrix of the structure evaluated at an equilibrium solution along the principal path, which is a function of the scalar parameter $\lambda$, and $\Delta \boldsymbol{u}$ is any kinematically admissible generalized displacement perturbation (i.e. contains displacement as well as rotation degrees of freedom).

### Stability of the Infinite, Perfect Honeycomb

Making use of the periodicity of the principal solution and using static condensation to eliminate internal degrees of freedom (DOFs) of the unit cell, the stability of the infinite structure requires the positive definiteness of the quadratic form defined on the unit cell

$$\hat{\varphi}(\lambda, \Delta \boldsymbol{u}) = \sum_{i,j=1}^{6} \Delta \boldsymbol{u}_i^* \bullet \boldsymbol{K}_{ij}(\lambda) \bullet \Delta \boldsymbol{u}_j, \tag{2.10}$$

where the $4 \times 4$ stiffness matrix $\boldsymbol{K}_{ij}$ is associated with the generalized force perturbation at boundary node $i$ of the unit cell due to generalized displacement perturbation $\Delta \boldsymbol{u}_j$ at boundary node $j$ (see again Figure 2.1(a) for the numbering of the six exterior unit cell nodes). The stability investigation further requires the Bloch wave representation theory

---

[5] From here on bold-face symbols denote vectors and matrices while a (•) denotes a simple contraction (inner product).

[6] The superscript $(^*)$ denotes complex conjugation of the transpose quantity. The extension to the complex domain of the quadratic form associated with the stability of the structure enables the efficient use of the Bloch wave representation theorem.

for the displacement perturbations, since it probes all wavelengths and directions. This approach simplifies the problem considerably, since it requires only the incremental response of the unit cell. Although the corresponding methodology is explained in detail in [32] for rectangular grillages, [33] for hexagonal honeycomb structures and [30] for the continuum case, a brief description is included here for completeness.

From Bloch wave representation theory the generalized displacement perturbation $\Delta \boldsymbol{u}$ takes the form

$$\Delta \boldsymbol{u}(X_1, X_2) = \exp\left[i\left(\omega_1 X_1 + \omega_2 X_2\right)\right] \boldsymbol{p}(X_1, X_2), \tag{2.11}$$

where $i = \sqrt{-1}$, $\omega_I$ is the wavenumber of the perturbation along the direction $X_I$, and $\boldsymbol{p}(\boldsymbol{X})$ is a doubly periodic complex-valued vector function of the spatial coordinates $X_1$ and $X_2$ with periods equal to the unit cell dimensions, i.e. $\boldsymbol{p}(X_1, X_2) = \boldsymbol{p}(X_1 + m_1 L_1, X_2 + m_2 L_2)$ for any pair of integers $(m_1, m_2)$.

From (2.11) one deduces the following relation between the displacement perturbations at the boundary nodes

$$\begin{bmatrix} \Delta \boldsymbol{u}_4 \\ \Delta \boldsymbol{u}_5 \\ \Delta \boldsymbol{u}_6 \end{bmatrix} = \begin{bmatrix} \mathbf{0} & \mathbf{0} & \exp(-i\omega_1 L_1)\boldsymbol{I} \\ \mathbf{0} & \exp(i\omega_2 L_2)\boldsymbol{I} & \mathbf{0} \\ \exp(-i\omega_1 L_1 + i\omega_2 L_2)\boldsymbol{I} & \mathbf{0} & \mathbf{0} \end{bmatrix} \begin{bmatrix} \Delta \boldsymbol{u}_1 \\ \Delta \boldsymbol{u}_2 \\ \Delta \boldsymbol{u}_3 \end{bmatrix} \tag{2.12}$$

where $\mathbf{0}$ and $\boldsymbol{I}$ are $4 \times 4$ null and identity matrices, respectively. The above equation can be rewritten in the more concise form

$$\Delta \boldsymbol{u}_\beta = \boldsymbol{A}(\omega_1 L_1, \omega_2 L_2) \bullet \Delta \boldsymbol{u}_\alpha \tag{2.13}$$

where the $12 \times 1$ vectors $\Delta \boldsymbol{u}_\alpha$, $\Delta \boldsymbol{u}_\beta$ and the $12 \times 12$ matrix $\boldsymbol{A}(\omega_1 L_1, \omega_2 L_2)$, which relates $\Delta \boldsymbol{u}_\beta$ to $\Delta \boldsymbol{u}_\alpha$, are given in (2.12). Using the definition for $\hat{\varphi}$ in (2.9) and the above introduced grouping of boundary perturbations $\Delta \boldsymbol{u}_j$, $j = 1, ...6$ into the two sets $\Delta \boldsymbol{u}_\alpha$ and $\Delta \boldsymbol{u}_\beta$, one can rewrite

$$\hat{\varphi} = \begin{bmatrix} \Delta \boldsymbol{u}_\alpha^* & \Delta \boldsymbol{u}_\beta^* \end{bmatrix} \begin{bmatrix} \boldsymbol{K}_{\alpha\alpha}(\lambda) & \boldsymbol{K}_{\alpha\beta}(\lambda) \\ \boldsymbol{K}_{\beta\alpha}(\lambda) & \boldsymbol{K}_{\beta\beta}(\lambda) \end{bmatrix} \begin{bmatrix} \Delta \boldsymbol{u}_\alpha \\ \Delta \boldsymbol{u}_\beta \end{bmatrix} \tag{2.14}$$

where the $12 \times 12$ submatrices $\boldsymbol{K}_{\alpha\alpha} = \boldsymbol{K}_{\alpha\alpha}^T$, $\boldsymbol{K}_{\alpha\beta} = \boldsymbol{K}_{\beta\alpha}^T$, $\boldsymbol{K}_{\beta\beta} = \boldsymbol{K}_{\beta\beta}^T$ are formed by grouping the corresponding $\boldsymbol{K}_{ij}$'s.

Upon substituting (2.13) into (2.14), the stability problem for the infinite perfect structure reduces to checking the positive definiteness of the following quadratic form

$$\begin{aligned} \hat{\varphi} &= \Delta \boldsymbol{u}_\alpha^* \bullet \widehat{\boldsymbol{K}}(\lambda; \omega_1 L_1, \omega_2 L_2) \bullet \Delta \boldsymbol{u}_\alpha \\ \widehat{\boldsymbol{K}} &\equiv \boldsymbol{K}_{\alpha\alpha} + \boldsymbol{K}_{\alpha\beta} \bullet \boldsymbol{A} + \boldsymbol{A}^* \bullet \boldsymbol{K}_{\beta\alpha} + \boldsymbol{A}^* \bullet \boldsymbol{K}_{\beta\beta} \bullet \boldsymbol{A} \end{aligned} \tag{2.15}$$

where $\boldsymbol{A}^*$ denotes the adjoint of $\boldsymbol{A}$ (i.e. the complex conjugate of its transpose). From the symmetry properties of $\boldsymbol{K}_{\alpha\alpha}$, $\boldsymbol{K}_{\alpha\beta}$, $\boldsymbol{K}_{\beta\alpha}$, $\boldsymbol{K}_{\beta\beta}$ one can verify that the stiffness matrix $\widehat{\boldsymbol{K}}$ is Hermitian ($\widehat{\boldsymbol{K}} = \widehat{\boldsymbol{K}}^*$) and thus has real eigenvalues. This reduces the stability investigation of an infinite, perfectly periodic structure to that of an equivalent but simpler problem involving half the boundary of the unit cell.

The case of a perturbation that has $L_I$ translational symmetry along the $X_I$ direction, i.e. $\omega_I L_I = 0$ for $I = 1$ or 2, admits from (2.12) a rigid body translation in the $X_I$ direction, i.e. $\Delta u_{iI} =$ const. for $i = 1, ..6$, $I = 1$ or 2. This case is included in the general numerical algorithm described above by imposing, in addition to (2.12) the condition $\Delta u_{1I} = 0$ for $I = 1$ or 2.

The scalar parameter $\lambda$ is a monotonically increasing "time-like" parameter that characterizes the deformed configuration of the unit cell in the infinite, perfect structure ($\lambda = 0$ corresponds to undeformed, stress-free configuration). If, for a given value of $\lambda$, $\widehat{\boldsymbol{K}}(\lambda; \omega_1 L_1, \omega_2 L_2)$ is positive definite for all dimensionless wave-numbers $(\omega_1 L_1, \omega_2 L_2) \in (0, 2\pi) \times (0, 2\pi)$ the configuration corresponding to $\lambda$ is stable. Consequently for each pair $(\omega_1 L_1, \omega_2 L_2)$, a minimum load $\lambda_m(\omega_1 L_1, \omega_2 L_2)$ may be found at which $\widehat{\boldsymbol{K}}$ looses positive definiteness. The critical load $\lambda_c$ at which the structure first looses stability in a monotonically loading process, is the infimum[7] (i.e. the highest lower bound) of $\lambda_m$ over the Fourier domain $(0, 2\pi) \times (0, 2\pi)$.

A remark about the nature of the eigenmode corresponding to the critical load $\lambda_c$ is in order at this point. The surface $\lambda_m(\omega_1 L_1, \omega_2 L_2)$ might exhibit a singular point at the origin $(0, 0)$. The physical reason for this singularity is the fact that in the neighborhood of $(0, 0)$ one finds, by inspecting (2.12) two different types of modes: (1) the finite wavelength modes for $(\omega_1 L_1, \omega_2 L_2) = (0, 0)$ with period one unit cell $\Delta \boldsymbol{u}(\boldsymbol{X}) = \boldsymbol{p}(\boldsymbol{X})$

---

[7] The concept of infimum is needed in view of a potential singularity at $(0, 0)$ of $\lambda_m(\omega_1 L_1, \omega_2 L_2)$, defined in the open domain $(0, 2\pi) \times (0, 2\pi)$. The value of $\lambda_m(\omega_1 L_1, \omega_2 L_2)$ as $(\omega_1 L_1, \omega_2 L_2) \rightarrow (0^+, 0^+)$ depends on the ratio $\omega_1 L_1 / \omega_2 L_2$ and one must consider $\lambda_m$ along all radial paths near $(0, 0)$ to find $\lambda_c$

and (2) the infinite wavelength modes for $(\omega_1 L_1, \omega_2 L_2) \rightarrow (0^+, 0^+)$ that are associated with nearly uniform modes with respect to the unit cell dimensions. When the lowest point of the $\lambda_m(\omega_1 L_1, \omega_2 L_2)$ surface is away from $(0, 0)$ the finite wavelength eigenmode requires no special numerical considerations. In the case when the infimum occurs as $(\omega_1 L_1, \omega_2 L_2) \rightarrow (0^+, 0^+)$ the critical mode may be a long wavelength one and another numerical technique is needed. Stability is checked in this case by the positive definiteness of the structure's homogenized incremental moduli (for proof see [9]). Consequently the structure's stability in the neighborhood of $(\omega_1 L_1, \omega_2 L_2) = (0, 0)$ is checked by two different, but complementary calculations.

A final remark: the methodology discussed here pertains to the onset of the first instability at $\lambda_c$ during the loading of the structure starting at $\lambda = 0$ and is based on calculating $\lambda_m(\omega_1 L_1, \omega_2 L_2)$, the minimum value of $\lambda$ at which $\widehat{\boldsymbol{K}}(\lambda; \omega_1 L_1, \omega_2 L_2)$ in (2.15) loses its positive definiteness. In general the structure might regain its stability upon further loading for adequately high values of $\lambda > \lambda_C$. The corresponding critical load $\lambda_C$, where stability is regained, can be determined in a similar fashion by finding the supremum (i.e. the lowest upper bound) of $\lambda_M(\omega_1 L_1, \omega_2 L_2)$ over $(0, 2\pi) \times (0, 2\pi)$ where $\lambda_M$ is the largest load parameter above which $\widehat{\boldsymbol{K}}(\lambda; \omega_1 L_1, \omega_2 L_2)$ regains positive definiteness for a given $(\omega_1 L_1, \omega_2 L_2)$.

## Stability of the Finite Honeycomb

The stability of the finite structures, perfect or imperfect, is a simpler task that depends on checking the positive definiteness of the entire structure's tangent stiffness matrix $\boldsymbol{K}(\lambda)$

(see (2.9)). Since this matrix is always available as part of the incremental Newton-Raphson procedure, checking for positive definiteness is a straightforward task that requires the diagonal matrix $\boldsymbol{D}$ of the $\boldsymbol{LDU}$ decomposition of $\boldsymbol{K}$. A matrix $\boldsymbol{D}$ with all positive diagonal entries corresponds to a stable structure.

## 2.3 Numerical Approach

The model described in the previous section is employed to predict the response of the SMA honeycomb under a uniaxial compression load-unload cycle along the $X_2$ direction. This section includes a presentation of selected constitutive parameters, the finite element discretization used, and a description of the numerical algorithm

### 2.3.1 Constitutive Parameters

Three different types of uniaxial constitutive laws are used in this study: a symmetric tension–compression law (Model 1), a more realistic asymmetric law to capture the behavior of textured polycrystals (Model 2), and a model calibrated to a specific honeycomb experiment (Model 3). Table 2.1 provides specific parameters used as base cases for the parameter study that follows. When studying the influence of a specific parameter on the SMA honeycomb response, the values of the parameter that are different from the base case value appearing in the table will be indicated on the corresponding response curve.

Table 2.1: Constitutive models

| | Model 1 | Model 2 | Model 3 |
|---|---|---|---|
| $E_A = E_M^+ = E_M^-$ | 1 | 1 | 75 GPa |
| $E_l^+$ | 0.05 | 0.05 | 11.25 GPa |
| $E_u^+$ | 0.05 | 0.05 | 10.3646 GPa |
| $E_l^-$ | 0.05 | 0.15 | 15 GPa |
| $E_u^-$ | 0.05 | 0.15 | 16.2766 GPa |
| $\beta^+$ | 0.0418 | 0.0418 | 0.031025 |
| $\beta^-$ | -0.0418 | -0.02125 | -0.0184 |
| $\varepsilon_n^+$ | 0.006 | 0.006 | 0.0035 |
| $\varepsilon_n^-$ | -0.006 | -0.012 | -0.007 |
| $\Delta\sigma_A^+$ | 0.002 | 0.002 | 0.1875 GPa |
| $\Delta\sigma_A^-$ | 0.002 | 0.002 | 0.2625 GPa |

### 2.3.2 Finite Element Discretization and Numerical Algorithm

The numerical algorithm employed in the subsequent calculations is based on the finite element method (FEM) and the discretization of the 1-D beam model given in eqs. (2.1) – (2.3). Our FEM model was implemented in the FEAP research software framework, [6]. The approach is a fairly standard incremental procedure; however, a few relevant details are presented here.

Each cell wall was divided into 20 elements of equal length, except for the calculations for the special case $E_t = 0$ which required 160 equal length elements to capture the concentration of curvature near the two ends of each deforming ligament. Within each element, a Hermitian cubic interpolation was used for the displacements $v(x)$, $w(x)$, resulting in four degrees of freedom (DOFs) per node, i.e. $v(x_n)$, $v_{,x}(x_n)$, $w(x_n)$, $w_{,x}(x_n)$. A four point Gauss quadrature was used for numerical integrations in the $x$-direction of each element. When the principal solution under monotonic loading was of interest, the through the thickness integrations were computed analytically (e.g. Figure 2.3 to Figure 2.5). In subsequent cases when hysteretic solutions were calculated, a 51-point trapezoidal rule with equi-distant points was used for thickness integrations in the $y$-direction. This rather large number of points in the $y$ direction was required to capture the evolution and precise locations of phase mixture boundaries.

The elements' translational degrees of freedom $v$ and $w$ must be transformed to the global coordinate system to enforce displacement continuity at the junction nodes. It can be shown that the rotation angle $\psi$ satisfies (in local coordinates) $\tan\psi = w_{,x}/(1 + v_{,x})$. Of the several choices that one can impose rotation continuity between adjacent elements at the junction nodes (three kinematic conditions but four DOFs available) the simplest one is by imposing continuity of the local derivatives ($v_{,x}$ and $w_{,x}$), treating these now as global DOFs, since they still maintain rotary continuity between adjacent beam elements (see again [33]).

An incremental Newton-Raphson procedure was employed to solve the resulting equations. In all but the final experiment simulations top and bottom displacement boundary conditions were enforced directly (by reduction of the equilibrium equations) while lateral edges were unconstrained. For the final simulations of the actual honeycomb structure a penalty-based contact algorithm with regularized Coulomb friction was used to capture nonuniform contact and frictional effects of the platens. The loading increment was approximately 0.14 $\%$ macroscopic strain for the infinite structures stability calculations, while it was occasionally lowered to help the convergence of the finite sized structures.

## 2.4 Results and Discussion

The results of several FEM simulations are now presented, progressing from the infinite-perfect honeycomb to the finite-perfect honeycomb and then to the finite-imperfect honeycomb. We proceed incrementally, starting with the infinite-perfect structure, since the principal path configurations are simple, periodic ones and the analysis gives one a sense of the "bulk" (many cell) behavior independent of boundary issues. It is a convenient context to perform a parameter study of the material law. The finite-perfect structure cases help to address the added influence of boundary constraints on the behavior, and the finite-imperfection structure cases helps to quantify the imperfection sensitivity of the response. Stability issues and the influence of constitutive parameters are discussed for each case. The monotonically increasing loading parameter $\lambda$ of Section 2.2.3 is taken to be $\delta/H$ for loading phase ($\dot{\delta} > 0$) and $2(\delta/H)_{max} - \delta/H$ for unloading ($\dot{\delta} < 0$) where $\delta/H$ is the macroscopic strain.

### 2.4.1 Principal Branch of the Infinite, Perfect Honeycomb

We studied the influence of constitutive parameters on the response of the infinite-perfect honeycomb as shown in Figure 2.3 to Figure 2.8, where at this point, all deformations were assumed to be cell-periodic. Results are plotted in diagrams of compressive, dimensionless macroscopic stress $F/EA$ vs. macroscopic strain $\delta/H$. The cross-sectional area, $A$, was taken as the total inclusive reference (initial) area of the footprint of the envelope of the honeycomb, to obtain an average-homogenized stress measure. The influence of material parameters associated with the loading part of the constitutive law, i.e. $\varepsilon_n$ and

$E_t$, is presented in Figure 2.3 to Figure 2.5, while the influence of the hysteretic part of the constitutive law is investigated in Figure 2.6 to Figure 2.8. Since all cells deform identically (cell-periodic) in the principal solution of the infinite-perfect structure, due to the symmetry of geometry and loading, only a quarter of the unit cell, shown as an insert in these figures, was required in the calculations. In fact, only the slanted ligament was needed, since the horizontal cell walls remained unstressed. The different uniaxial constitutive laws used are shown as inserts in the corresponding figures.

The influence of the nucleation strain $\varepsilon_n$ on the principal solution under loading, for the case of a symmetric (tension-compression) uniaxial response, is shown in Figure 2.3(a). As expected, increasing $\varepsilon_n^+ = \varepsilon_n^-$ from $0.002$ to $0.010$ (centered on the base case of Model 1, $\varepsilon_n = 0.006$) results in delaying the deviation of the structure's response away from the initial, nearly linear regime. Moreover, while increasing $\varepsilon_n$ raises the stress at the onset of the $A \to M$ transformation, it softens the initial tangent modulus (plateau regime, near $0.1 < \delta/H < 0.4$). The responses then stiffen at larger macroscopic strains ($\delta/H > 0.5$). Limit loads, both local maxima and minima, are shown by $\wedge$ and $\vee$, respectively, in the figure. Note that no such limit load exists for the lowest value of $\varepsilon_n = 0.002$. Points are also shown where the local maximum tensile strain has reached $0.025$, a commonly imposed limit for high cycle fatigue life of Nitinol. This shows the "strain amplification" achieved by the thin walled honeycomb, since it occurs at macroscopic strains near $0.1$. The initial softening of the response is due to a geometric effect of the deforming cell walls which results in the appearance, above a certain value of $\varepsilon_n$, of a local maximum in the macroscopic stress-strain response, despite the fact that the underlying constitutive response of the material is strictly stable, i.e. $E > E_t > 0$.

Figure 2.3(b) shows contours of phase fraction ($\xi$), local strain ($\varepsilon$), and normalized local stress ($\sigma/E$) in the slanted cell wall at four values of compressive strain ($\delta/H$). It shows that transformation is concentrated at the ends of the ligament, especially in the corners. The phase fraction and strain have nearly linear distributions across the thickness, but the stress has a nonlinear distribution, as one would expect from the constitutive law. We recognize that the maximum stress at the largest macroscopic compressive strain shown ($\delta/H = 0.7$) is unrealistically large (near 2 GPa for a typical value of $E = 75$ GPa), indicating that local plasticity and significant "locked-in" martensite (not modeled here) would actually exist at such large macroscopic strains, thereby preventing perfect superelasticity upon unloading.

The usual figures-of-merit for honeycombs made of conventional metals are specific stiffness and energy absorption capability, but the use of SMAs now allows us to additionally consider the more ambitious goal of recovering the macroscopic strain after significant deformation. One should, therefore, consider the material's strain recovery limitations to ensure macroscopic strain recovery can actually be realized. Figure 2.3(c) plots the maximum local tensile strain ($\varepsilon_{\max}$), i.e., worst case of all $(x, y)$ points in the structure, as a function of macroscopic compressive strain ($\delta/H$) for the various parameters of $\varepsilon_n$. With relatively large values of $\varepsilon_n$ the maximum local strain is roughly tri-linear. For the base case of Model 1 ($\varepsilon_n = 0.006$), the maximum local strain grows linearly until about $\delta/H = 0.05$, then grows more steeply until about $\delta/H = 0.18$, and then levels off at a lower slope. At a maximum local strain of 0.025 (approximate high cycle strain limit for NiTi) the corresponding macroscopic strain is about 0.094. At a maximum local strain of 0.06 (a reasonable local strain limit for low cycle operation) the corresponding macroscopic strain is about 0.417, giving a sense of the strain amplification of the honeycomb structure. Thus, Fig. 2.3(c) provides guidelines for the range of macroscopic (global) strains that can be accommodated by local martensitic transformation in the SMA material without incurring significant plasticity that would otherwise impede reverse transformation upon unloading.

Figure 2.3(c) also shows the advantage of an SMA over a conventional metallic (e.g. aluminum) honeycomb. Since the yield strain for aluminum is typically of the order of $0.002$, the maximum reversible macroscopic strain (elastic range) for an aluminum honeycomb would be, according to Figure 2.3(c), less than $\delta/H = 0.02$, over 20 times lower than the corresponding value for an SMA honeycomb of the same geometry ($\delta/H = 0.417$). Alternatively, one could reduce the $t/L$ ratio to keep the conventional honeycomb within its elastic range, but as noted in [26] this would sacrifice stiffness by a factor of over 1000, since the stiffness of the honeycomb scales roughly by $(t/L)^3$, thereby making this an impractical prospect.

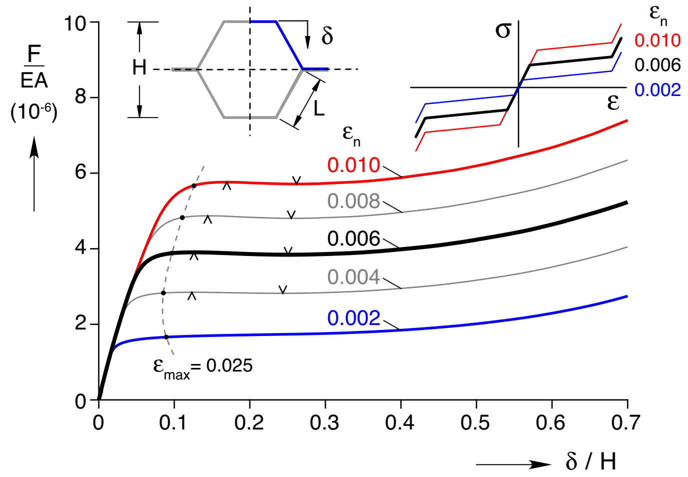

(a)

Figure 2.3: (a) Principal branches of the dimensionless macroscopic compressive stress $(F/EA)$ vs. compressive strain $(\delta/H)$ response of the infinite-perfect honeycomb, based on constitutive Model 1 (right inset), showing the influence of nucleation strain $(\varepsilon_n)$.

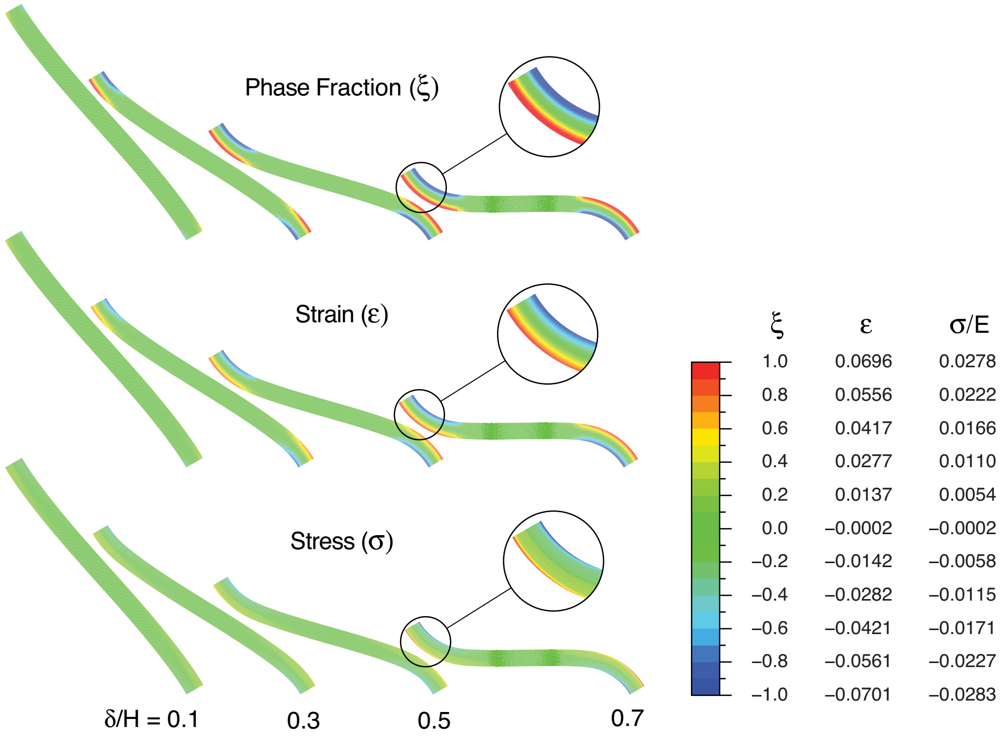

(b)

Figure 2.3: (b) Contours of phase fraction $(\xi)$, local strain $(\varepsilon)$, and local stress $(\sigma/E)$ in the slanted cell wall (Model 1, $\varepsilon_n = 0.006$).

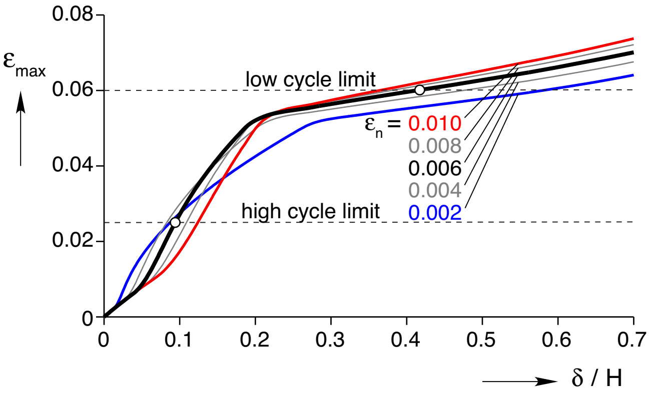

(c)

Figure 2.3: (c) Maximum local tensile strain ($\varepsilon_{\max}$) as a function of macroscopic compression ($\delta/H$) for the same constitutive laws of 2.3(a).

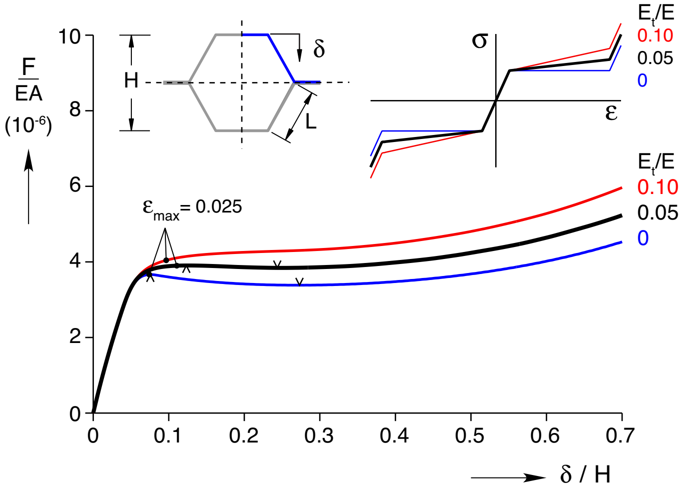

Figure 2.4: Principal branches of the dimensionless macroscopic compressive stress $(F/EA)$ vs. compressive strain $(\delta/H)$ response of the infinite-perfect honeycomb, based on constitutive Model 1 (right inset), showing the influence of transformation tangent modulus $(E_t)$.

The influence of the transformation tangent modulus $E_t$ on the perfect structure's principal loading solution, for the symmetric uniaxial response is presented in Figure 2.4. As expected, increasing $E_t/E$ stiffens uniformly the $A \rightarrow M$ transformation regime. However, it is worth noticing that for $E_t/E = 0$ a maximum exists in the macroscopic stress-strain response soon after the structure deviates from its linear regime. The load maximum persists even for the case of the strictly monotonic uniaxial response at $E_t/E = 0.05$, albeit at a larger macroscopic strain. Upon further increase to $E_t/E = 0.1$ the macroscopic stress-strain response is monotonic (no limit loads), thus implying that the constitutive stiffening overcomes the geometric softening effect. We should mention here that, not surprisingly, numerical difficulties were encountered for the case of $E_t/E = 0$. The deformed shape of the cell involved extreme bending localization at the ends of the slanted wall. The cell wall's curvature experienced a sharp change, which required a higher number of elements 160 elements along the cell wall length).

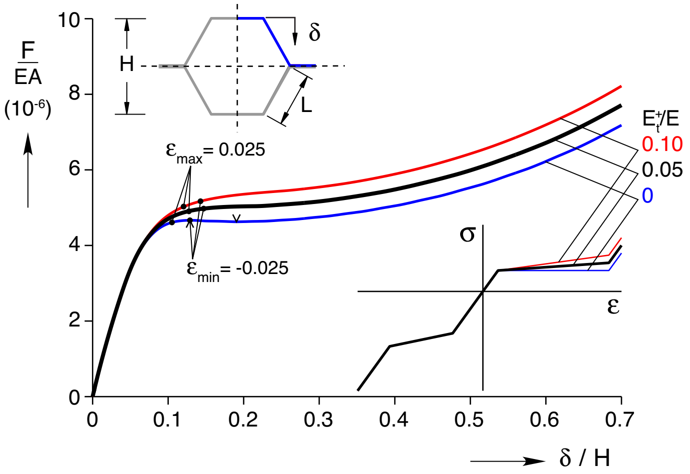

Figure 2.5: Principal branches of the dimensionless macroscopic compressive stress $(F/EA)$ vs. compressive strain $(\delta/H)$ response of the infinite-perfect honeycomb, based on asymmetric constitutive Model 2 (right inset), showing the influence of tensile transformation tangent modulus $(E_t^+)$.

The influence of the tensile transformation tangent modulus $E_t^+$ on the infinite-perfect structure's principal solution under loading, but for the asymmetric constitutive law (Model 2), is presented in Figure 2.5. The material's stiffer response in compression ($E_t^-/E = 0.15$), as compared to tension, resulted in about 25 % higher macroscopic stresses for a given macroscopic strain than occurs for the its symmetric counterpart in Figure 2.4. Since the bending of cell walls involves compressive as well as tensile stresses, the higher stiffness of the compressive transformation zone ($E_t^-/E > E_t^+/E$) as well as its smaller transformation strain ($\beta^- > \beta^+$) resulted in a higher macroscopic tangent moduli for a given macroscopic strain as seen in Figure 2.5 compared to Figure 2.4. Notice that the structure's macroscopic stress-strain response shows a limit load only for $E_t^+/E = 0$, but weaker than in Figure 2.4.

The influence of the amplitude of the hysteresis loop $\Delta\sigma$ for a symmetric uniaxial material law is presented in Figure 2.6, where unloading for all cases start at macroscopic

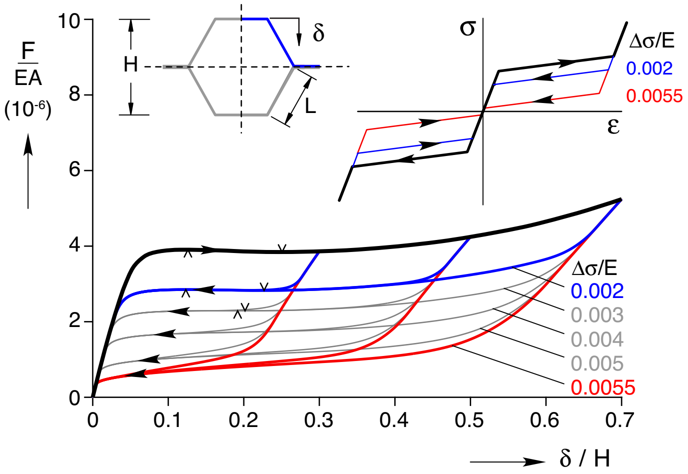

Figure 2.6: Principal branches of the dimensionless macroscopic compressive stress $(F/EA)$ vs. compressive strain $(\delta/H)$ load-unload responses of the infinite-perfect honeycomb, based on hysteretic constitutive Model 1 (right inset), showing the influence of stress hysteresis $(\Delta\sigma/E)$. Unloading paths shown start at macroscopic strains $\delta/H = 0.3, 0.5, 0.7$.

strains $\delta/H = 0.3$, 0.5 and 0.7. Notice that the initial slope of the unloading branch decreases as the macroscopic strain at unloading increases, due to the resulting geometric change of the unit cell. Also notice that for the smallest amplitude of hysteresis $\Delta\sigma/E = 0.002$ the unloading branch starting from the lower strains $\delta/H = 0.3$ and $\delta/H = 0.5$ converge rapidly to the corresponding unloading branch that starts at $\delta/H = 0.7$. As $\Delta\sigma$ increases, the discrepancies between the different unloading paths progressively increase. Also, hysteresis values greater than 0.003 eliminate any possibility of limit loads in the unloading curves.

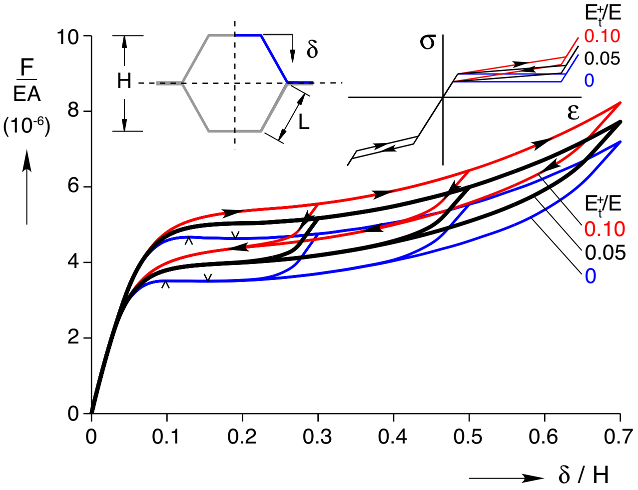

Figure 2.7: Principal branches of the dimensionless macroscopic compressive stress $(F/EA)$ vs. compressive strain $(\delta/H)$ load-unload responses of the infinite-perfect honeycomb, based on asymmetric, hysteretic constitutive Model 2 (right inset), showing the influence of tensile transformation modulus $(E_t^+)$.

The influence of the tensile transformation tangent modulus $E_t^+$, but for the asymmetric constitutive law (Model 2), is presented in Figure 2.7, where as in Figure 2.6, unloadings at $\delta/H = 0.3$, 0.5 and 0.7 were considered. As expected from the results of Figure 2.5, an increase in $E_t^+/E$ results in an overall stiffer response, occurring at progressively higher macroscopic stress levels (for the same macroscopic strains). Notice that, similar to Figure 2.6, the initial slope of the unloading branch decreases with increasing strain at unloading but is independent of $E_t^+$, i.e. unloading branches starting at the same macroscopic strain are approximately initially parallel to each other, since the deformed geometries are comparable at this point.

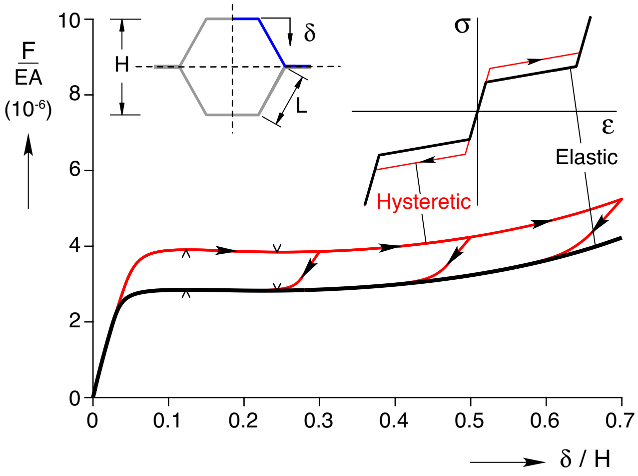

Figure 2.8: Principal branches of the dimensionless macroscopic compressive stress $(F/EA)$ vs. compressive strain $(\delta/H)$ response of the infinite-perfect honeycomb, based on constitutive Model 1 (right inset), comparing the unloading response of the hysteretic model with an “elastic” one.

A noteworthy feature of the results presented in Figure 2.6 is the near independence of the unloading branch on the structure’s deformation history, since all three unloading branches converge to the same curve, after some initial elastic unloading. To further illustrate the near load-path independence of the principal solution’s unloading branch, Figure 2.8 compares, for the symmetric constitutive law, the unloading paths obtained by reversing the macroscopic strain at $\delta/H = 0.3$, 0.5 and 0.7 to the loading path of the same structure with an "elastic" constitutive response that coincides with the unloading branch of the hysteretic model (see insert of Figure 2.8). The comparison indeed confirms that the response during active $A \leftrightarrow M$ transformation is nearly independent of the loading path, i.e. the response eventually tends towards a fundamental "outer-loop" response, consistent with the chosen material law.

### 2.4.2 Stability of the Infinite, Perfect Honeycomb

The next set of calculations, presented in Figure 2.9 to Figure 2.14 address the stability of the principal solution of the infinite-perfect structure under displacement ($\delta/H$) control (stiff loading device) for the same constitutive laws used previously in Figure 2.3 to Figure 2.8. The full unit cell (shown as an insert in these figures) was now required to perform the Bloch wave stability calculations. Stable equilibrium paths are indicated with a bold line, while unstable paths are drawn with a thin line. Limits loads are indicated as before with $\wedge$ and $\vee$. Critical points, where the stability of the path changes, are shown with open circles.

The stability of the loading path of the principal (unit cell-periodic) solution of the infinite-perfect structure for a symmetric constitutive response, but with different nucleation strains $\varepsilon_n$, is shown in Figure 2.9. Notice that for sufficiently low $\varepsilon_n \leq 0.001$, the principal solution is stable for all strains. Interestingly, the case of $\varepsilon_n = 0.002$ has critical bifurcation points, yet no limit loads. As $\varepsilon_n$ increases further, and the correspond-

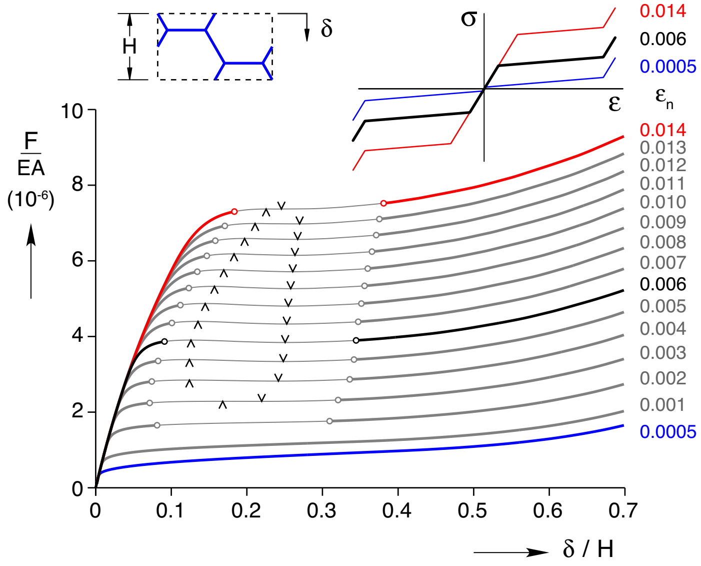

Figure 2.9: Stability of macroscopic compressive stress-strain, $(F/EA)$ vs. $(\delta/H)$, responses for the perfect, infinite honeycomb under $\delta/H$ control, showing the influence of nucleation strain ($\varepsilon_n$). Stable and unstable segments are indicated by thick and thin lines, respectively, and stability changes are shown with circles on the paths.

ing macroscopic tangent modulus softens, an unstable zone appears. At sufficiently large strains, however, it restabilizes as transformation saturates and the increased material stiffness overwhelms the kinematic softening of the cell. Additionally, note that in each case for $\varepsilon_n \geq 0.003$ the onset of instability precedes the maximum load, i.e., while the response still has a positive slope, and then the path regains stability after the local minimum. The presence of an unstable region in the principal solution of the infinite-perfect structure has important implications for the behavior of finite structures, perfect and imperfect, as will be seen subsequently.

Some comments are in order about the nature of the critical modes at the two end points of the unstable zones, i.e., at the first onset of instability and termination of instability along the principal path. In both cases the critical mode is a long wavelength mode. Figure 2.10

presents an analysis for the case of Model 1 (base case of Figure 2.9), showing the critical macroscopic strain as a function of dimensionless wavenumbers $(\omega_1 L_1, \omega_2 L_2)$, i.e surface $\lambda_m(\omega_1 L_1, \omega_2 L_2)$ corresponding to the first loss of positive definiteness of $\widehat{\boldsymbol{K}}$ as defined in sub-section 2.2.3. The onset of instability occurs at $\delta/H = 0.092$ with the minimum load corresponding to wavenumbers near the origin, indicating a possible long wave length mode. The origin $(\omega_1 L_1, \omega_2 L_2) \to (0, 0)$ is a singularity of the Bloch wave analysis, so the critical mode shown here does not quite reach the origin due to the discretization of wave numbers used. Consequently, the long wave length mode was confirmed by a separate analysis of the homogenized moduli. A similar situation occurs at the termination of the unstable range at $\delta/H = 0.342$, where the instability mode is again a long wavelength one. At intermediate strains the path is unstable, as shown in Figure 2.9.

These characteristics are typical of the instability of the principal load path in all cases considered in this chapter. The fact that the eigenmode corresponding to $\lambda_c$ is a “global”, i.e. long wavelength mode, and not a “local” one is due to the particular loading orientation and is perhaps not surprising in view of results by [33] (same geometry, similar bilinear constitutive law). Other load orientations would likely exhibit instability with respect to modes of finite wavelength. Indeed, in a series of in–plane crushing experiments of Aluminum honeycomb, [24] compressed the structure along the $X_1$ direction and found that the corresponding critical mode is a “local” one, a fact that was verified subsequently by the Bloch wave analysis of [33].

The influence of the tangent modulus $E_t$ for the symmetric constitutive law (Model 1) on the stability of the loading path of the principal solution of the infinite-perfect structure is shown in Figure 2.11. As expected, increasing $E_t/E$ results in decreasing the extent of the unstable zone. As seen before, for cases cases $E_t/E = 0, 0.05$ the extent of instability extends beyond the range of negative slope in the principal path (between limit loads). Even for the case ($E_t/E = 0.10$), where the path maintains a positive slope, a significant regime of instability exists. Despite the risk of belaboring a (perhaps) obvious point, we wish to emphasize here that monotonicity of the principal path is clearly not a sufficient criterion for stability.

The results in Figure 2.12 demonstrate the stability of the principal solution for the infinite-perfect structure, but for the asymmetric constitutive response (Model 2). As expected from the stiffer response of the material in compression, the extent of the unstable zones is considerably smaller compared to corresponding results in Figure 2.11 for the same $E_t^+/E$.

The stability for both the loading and the unloading branches of the principal solution of the infinite perfect structure is presented for the symmetric and asymmetric hysteretic constitutive laws respectively in Figure 2.13 and Figure 2.14. The influence of hysteresis $\Delta\sigma/E$ (same range as in Figure 2.6) on the stability of the loading-unloading path (using the symmetric Model 1) is presented in Figure 2.13. Except for the highest value $\Delta\sigma/E = 0.0055$, instability regions exist in both the loading and unloading paths. Figure 2.14 shows the the influence of $E_t^+/E$ on the stability of the principal solution of the infinite perfect structure having the same hysteretic, asymmetric constitutive laws (based on Model 2) as in Figure 2.7. In this case only the loading paths have unstable regions, while all the unloading paths shown are stable, even for the case where $E_t^+/E = 0$.

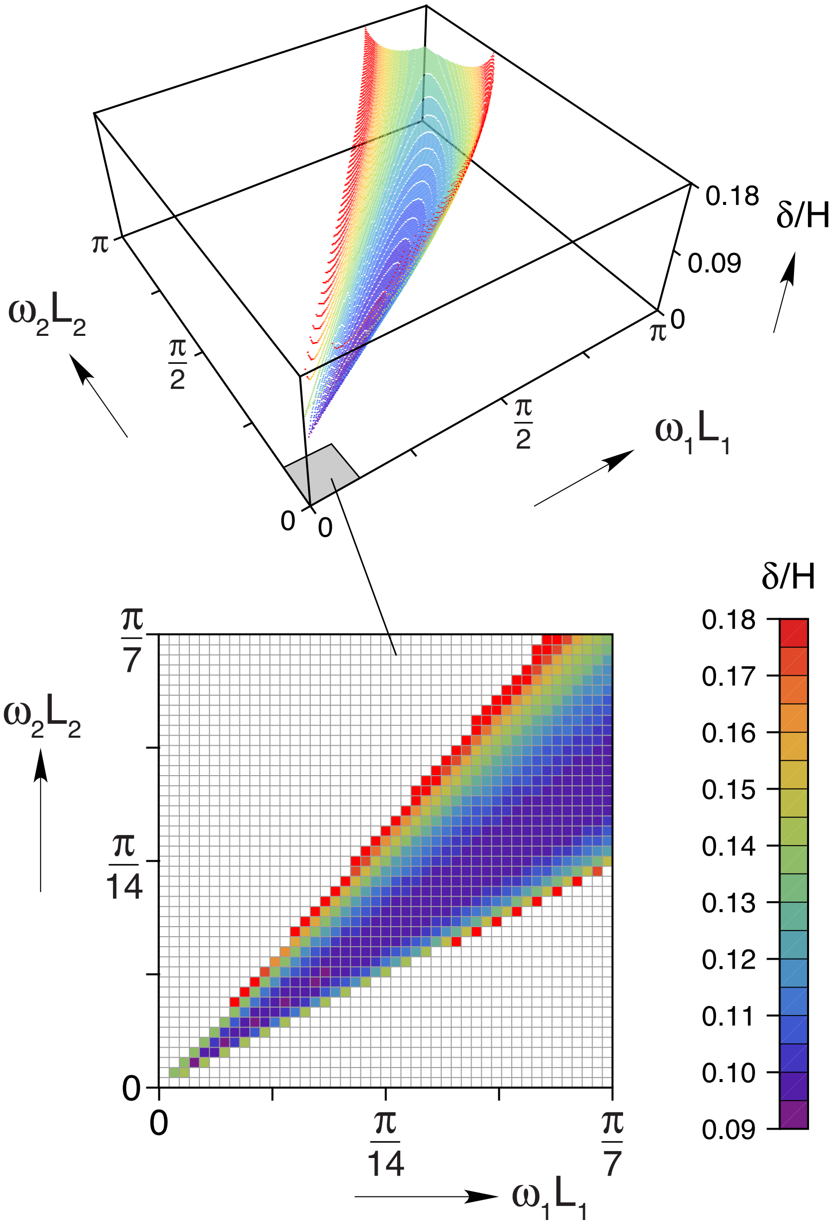

Figure 2.10: Lowest strain $(\delta/H)$ as a function of dimensionless wave numbers $(\omega_1 L_1, \omega_2 L_2)$ on the onset of instability of the infinite-perfect honeycomb calculated along the principal path with a symmetric, "elastic" constitutive law (Model 1). The minimum $(\delta/H = 0.092)$ occurs as $(\omega_1 L_1, \omega_2 L_2) \rightarrow (0, 0)$, indicating a long wavelength critical mode, which is confirmed from a loss of ellipticity calculation of the homogenized incremental moduli.

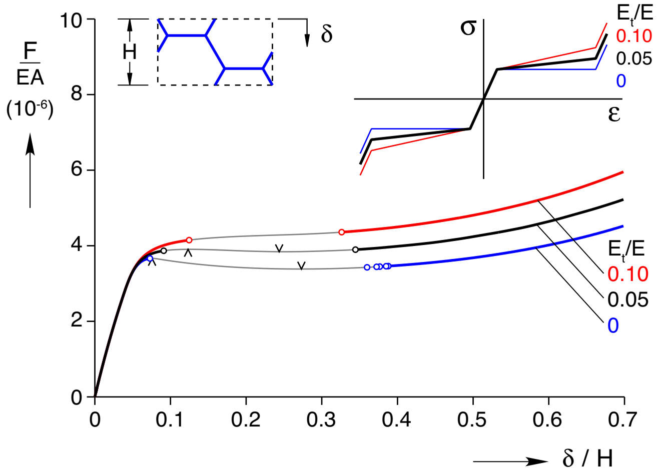

Figure 2.11: Stability of macroscopic compressive stress-strain, $(F/EA)$ vs. $(\delta/H)$, responses for the perfect, infinite honeycomb under $\delta/H$ control, showing the influence of transformation modulus $(E_t)$ using Model 1 as the base case. Note, multiple changes in stability occur along the response for $E_t = 0$.

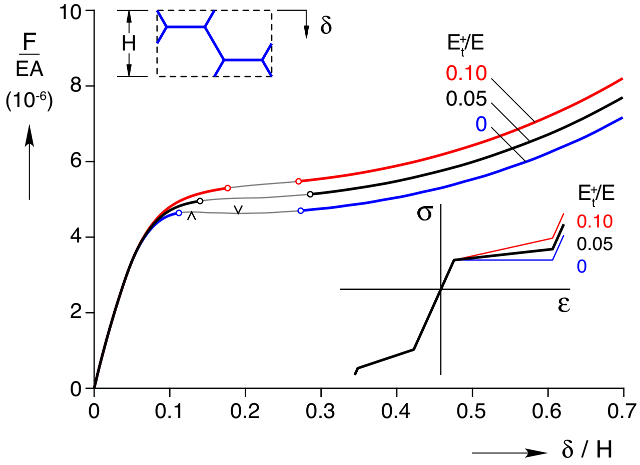

Figure 2.12: Stability of macroscopic compressive stress-strain, $(F/EA)$ vs. $(\delta/H)$, responses for the perfect, infinite honeycomb under $\delta/H$ control based on asymmetric Model 2, showing the influence of tensile transformation modulus $(E_t^+)$.

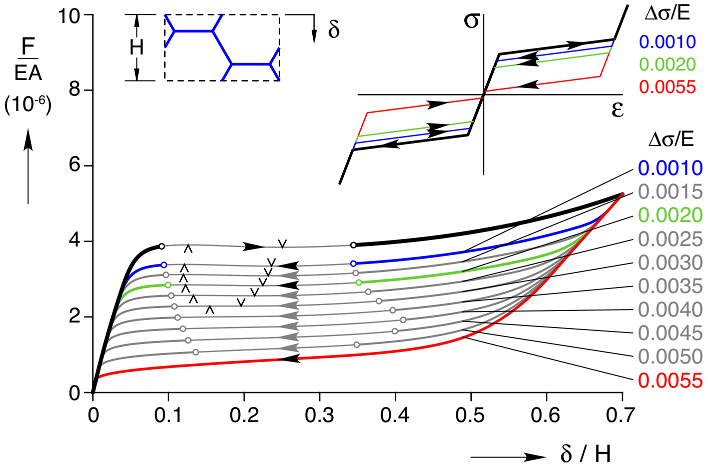

Figure 2.13: Stability of macroscopic compressive stress-strain, $(F/EA)$ vs. $(\delta/H)$, load-unload responses for the perfect, infinite honeycomb under $\delta/H$ control, showing the influence of stress hysteresis ($\Delta\sigma/E$) for symmetric, hysteretic material.

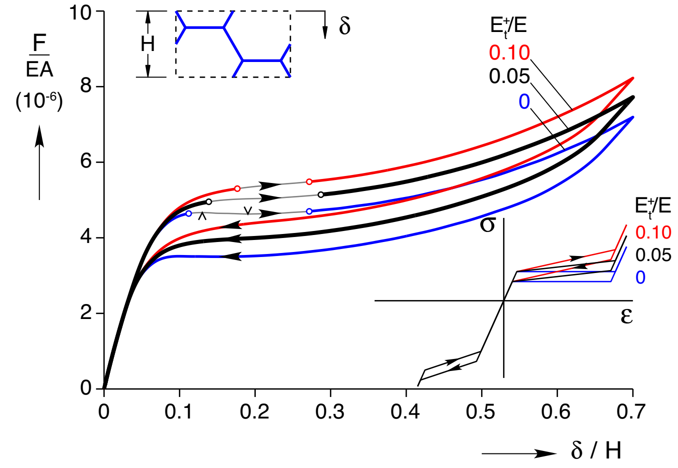

Figure 2.14: Stability of macroscopic compressive stress-strain, $(F/EA)$ vs. $(\delta/H)$, load-unload responses for the perfect, infinite honeycomb under $\delta/H$ control, showing the influence of tensile transformation modulus ($E_t^+$) for asymmetric, hysteretic material (based on Model 2).

### 2.4.3 Response of the Finite, Perfect Honeycomb

Finite element simulations of perfect honeycombs of finite size are presented in Figure 2.15 and Figure 2.16 to investigate the influence of boundary conditions. The selected geometry corresponds to the topology (but with an idealized, perfect geometry) and overall dimensions of the fabricated specimen used in the isothermal experiment of [26], to be presented later in Section 2.4.5.

The response of the finite size, perfect structure under uniaxial compression calculated for a symmetric, hysteretic constitutive law (Model 1) is presented in Figure 2.15. The loading device was modeled as frictionless. The principal solution of the finite, perfect structure has all cells deforming identically and hence coincides with the principal solution of the infinite perfect structure (yet the stress-free lateral edges may have new implications for stability). For comparison the response of the principal solution for the infinite-perfect structure is also shown in the same figure. The macroscopic force-displacement loading-unloading curves for both (infinite and finite) structures are given in Figure 2.15(a). The infinite honeycomb response has unstable segments during loading and unloading, yet the finite honeycomb response does not. The responses of the two structures are similar, but start diverging on the loading and unloading branches near the onset of instability of the infinite structure. It is not surprising that the responses of the finite-perfect and infinite-periodic structures coincide again at macroscopic strains well above or below the strain levels where the paths of the infinite-periodic solution are stable.

A better, quantitative measure of the deviation between the finite and infinite honeycomb solutions is shown in Figure 2.15(b). The relative $\mathrm{L}_2$ norm of the two solutions,

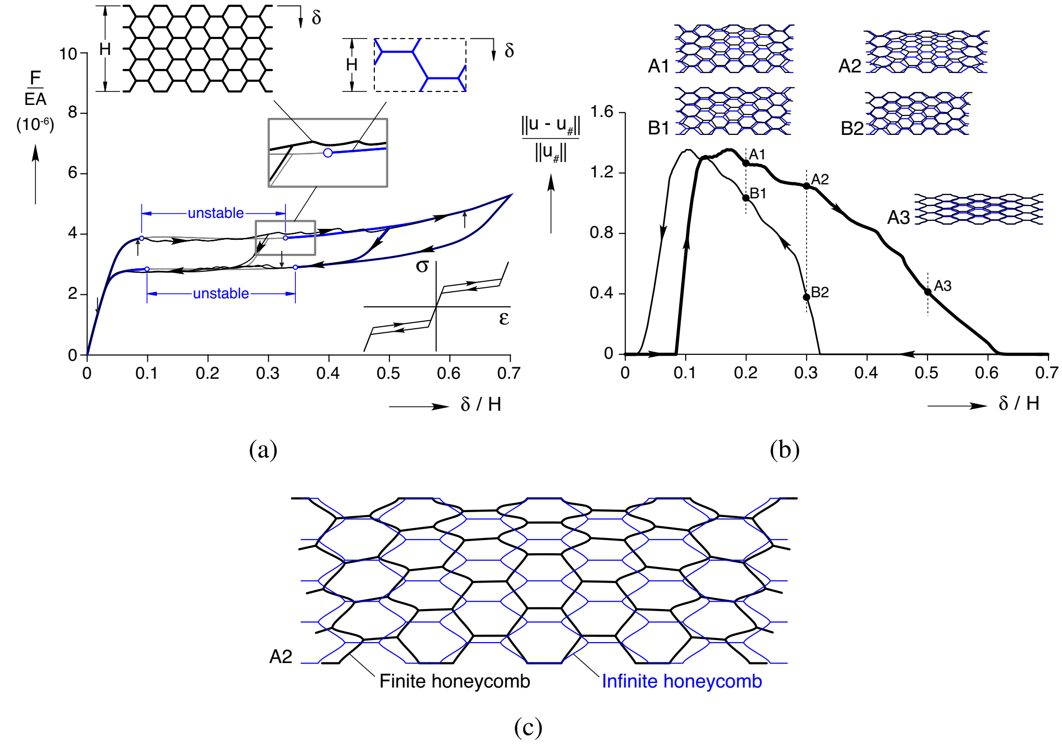

(a)

(b)

(c)

Figure 2.15: (a) Comparison of compressive loading-unloading responses of the finite (upper left inset) and infinite (upper right inset) perfect honeycombs with a symmetric, hysteretic constitutive response (Model 1). (b) Relative deviation $\|\boldsymbol{u}-\boldsymbol{u}_{\#}\|/\|\boldsymbol{u}_{\#}\|$ of the finite honeycomb's deformation ($\boldsymbol{u}$) from the infinite honeycomb's principal path deformation ($\boldsymbol{u}_{\#}$) vs. macroscopic compressive strain ($\delta/H$). The finite and periodic configurations are shown in insets at strains 0.2, 0.3 and 0.5 (loading path configurations A1, A2, A3 and the unloading path configurations B1 and B2.) (c) Magnified view of configuration A2 for the finite and infinite (periodic) configurations.

$\|\boldsymbol{u}-\boldsymbol{u}_{\#}\|/\|\boldsymbol{u}_{\#}\|$, is plotted against the macroscopic strain, where

$$\begin{aligned}
\|\boldsymbol{u}_{\#}\|^2 &\equiv \int_{\text{cell walls}} [v_{\#}^2(x)+w_{\#}^2(x)]dx, \\
\|\boldsymbol{u}-\boldsymbol{u}_{\#}\|^2 &\equiv \int_{\text{cell walls}} [(v(x)-v_{\#}(x))^2+(w(x)-w_{\#}(x))^2]dx, \qquad (2.16)
\end{aligned}$$

and $(v, w)$ and $(v_{\#},\, w_{\#})$ are the respective displacements of the finite and infinite (periodic) honeycombs. The integrals over the cell walls are calculated numerically using the same

Gaussian quadrature used in the equilibrium calculations.

The deviation of the finite honeycomb's equilibrium path in Figure 2.15(b) from its periodic counterpart during loading occurs at $\delta/H = 0.084$, (denoted by $\uparrow$ in Figure 2.15(a)) which just precedes the first instability at $\delta/H = 0.092$ encountered of the infinite structure[8]. The deviation disappears near $\delta/H = 0.624$ well after the final bifurcation point at $\delta/H = 0.328$. Upon unloading, deviation between the two paths appears at $\delta/H = 0.322$ soon after the bifurcation point at $\delta/H = 0.344$ and then disappears at $\delta/H = 0.018$ well after the final bifurcation point at $\delta/H = 0.099$.

The deformed configurations of the finite and infinite honeycombs are shown in Figure 2.15(b) at five different states: points A1, A2 and A3 on the loading branch ($\delta/H = 0.20, 0.30, 0.5$) and points B2 and B1 ($\delta/H = 0.30, 0.20$) on the unloading branch. The numerical calculations for the hysteretic, finite sample were obtained by a straightforward incremental algorithm with small step sizes (typically $\Delta\delta/H$ between about $3 \times 10^{-5}$ and $9 \times 10^{-5}$). This standard procedure, without any special modification, was adequate to allow the finite structure to take a particular, non-periodic, equilibrium path. As can be seen in the magnified view of state A2 in Figure 2.15(c) the overall shape of the finite honeycomb takes a roughly trapezoid shape, with cells flattening at the top more than at the bottom. Of course, other equilibrium paths exist, which are symmetry related to the calculated equilibrium path. The presence of internal variables in the model introduces numerical imperfections, thus selecting one of the geometrically equivalent paths. Other equilibrium paths are likely to exist (after all, the periodic solution has a high number of

---

[8] Instability of the finite-perfect structure precedes the onset of instability of the infinite counterpart, since it is not laterally constrained

symmetries), but the ease with which numerical solutions were found (without any overt imperfections included) leads us to believe, although without proof at this time, that the numerical solution found here is the energetically preferred path in a continuous loading process of the structure. Furthermore, the deformed patterns obtained are reminiscent of the configurations observed in experiments [26].

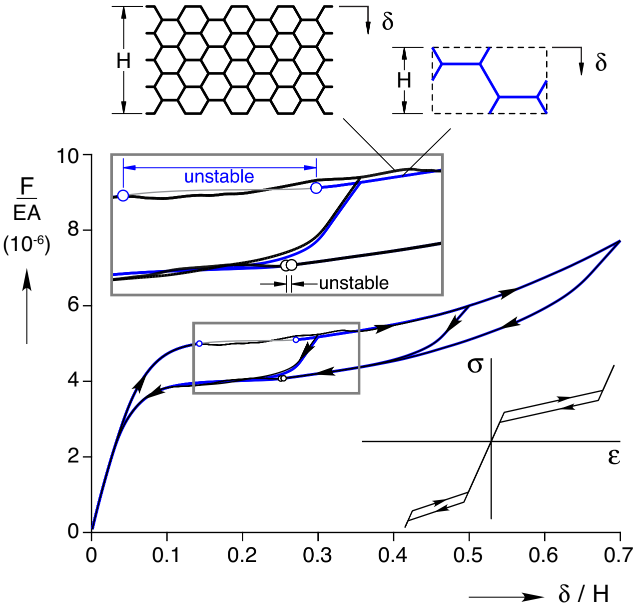

Figure 2.16: Comparison of compressive loading-unloading responses for the finite (upper left inset) and infinite (upper right inset) perfect honeycombs with an asymmetric, hysteretic constitutive response (Model 2).

The mechanical response of the finite honeycomb using the asymmetric constitutive response (Model 2) is presented in Figure 2.16. For comparison purposes the results are overlaid on the stability results for the corresponding infinite periodic case (from Figure 2.14). As before the finite honeycomb's force-displacement curve deviates from its periodic counterpart near the onset of first instability. However, a deviation of the finite size structure's response from the corresponding periodic results is found on the unloading path as well. This discrepancy is unexpected, in view of the stability of the entire unloading path of the infinite, periodic solution found according to the results in Figure 2.14. However, this mystery can be explained by the presence of the tiny unstable region on the principal unloading branch of the finite structure. (In fact, this unstable region was not initially detected until a more detailed calculation was performed with very fine increments.) Interestingly, the infinite honeycomb response has an unstable segment during loading but not unloading, yet the finite honeycomb response is stable during loading but has this short unstable segment during unloading.

### 2.4.4 Response of Finite, Imperfect Honeycombs

The influence of imperfections on the response of the actual, finite size structure is shown in Figure 2.17 and Figure 2.18 for the symmetric and asymmetric constitutive response, respectively. The construction of a “hypothetical” imperfect structure was achieved by randomly perturbing the location of the internal cell junctions of the perfect structure. Each node of the perfect specimen was displaced within a disc of radius $\Delta r = \zeta L$ (where L is the unit cell side), where the radius and the angle for the nodal perturbation vector were chosen randomly in the respective intervals $[0, \Delta r)$ and $[0, 2\pi)$.

Figure 2.17(a) shows the macroscopic stress-strain responses of the perfect ($\zeta = 0$) and two imperfect ($\zeta = 0.01$, $0.1$) structures. The paths are similar, undulating about a plateau stress at intermediate strains, yet all the paths shown are stable everywhere. The figure reveals little influence of the imperfection for the small imperfection amplitude ($\zeta = 0.01$) but more significant deviations from the perfect responses for the larger amplitude ($\zeta = 0.1$), especially at large strains ($\delta/H > 0.5$). The same conclusion can be reached from Figure 2.17(b), where the relative deviation between the finite and periodic solution is plotted as a function of macroscopic strain. As expected, the loading-unloading curve for the smaller imperfection ($\zeta = 0.01$) is closer to the perfect case ($\zeta = 0$) than the corresponding curve for the larger imperfection ($\zeta = 0.1$). Figure 2.17(b) shows that the configurations diverge from each other at small macroscopic strains initially (say, $\delta/H < 0.05$), but then tend to converge somewhat toward the perfect case as strains near $\delta/H = 0.1$. The largest differences between the three cases are apparent in Figure 2.17(b) upon unloading (from $\delta/H = 0.7$ down to about $\delta/H = 0.2$), but then they converge closely to the perfect case at small strains ($\delta/H < 0.1$).

The comparison of the macroscopic stress-strain response of the finite, perfect ($\zeta = 0$) and two imperfect ($\zeta = 0.01,\ 0.1$) structures for the case of the asymmetric constitutive law (Model 2) is presented in Figure 2.18. Again, all paths shown are stable everywhere, showing that while the path undulates for much of the path, imperfections help to suppress the possibility of instability. Consistent with the results of Figure 2.17, there is little difference between the behavior of the perfect ($\zeta = 0$) and the slightly imperfect ($\zeta = 0.01$) structures, and a more apparent difference with the more imperfect structure ($\zeta = 0.1$).

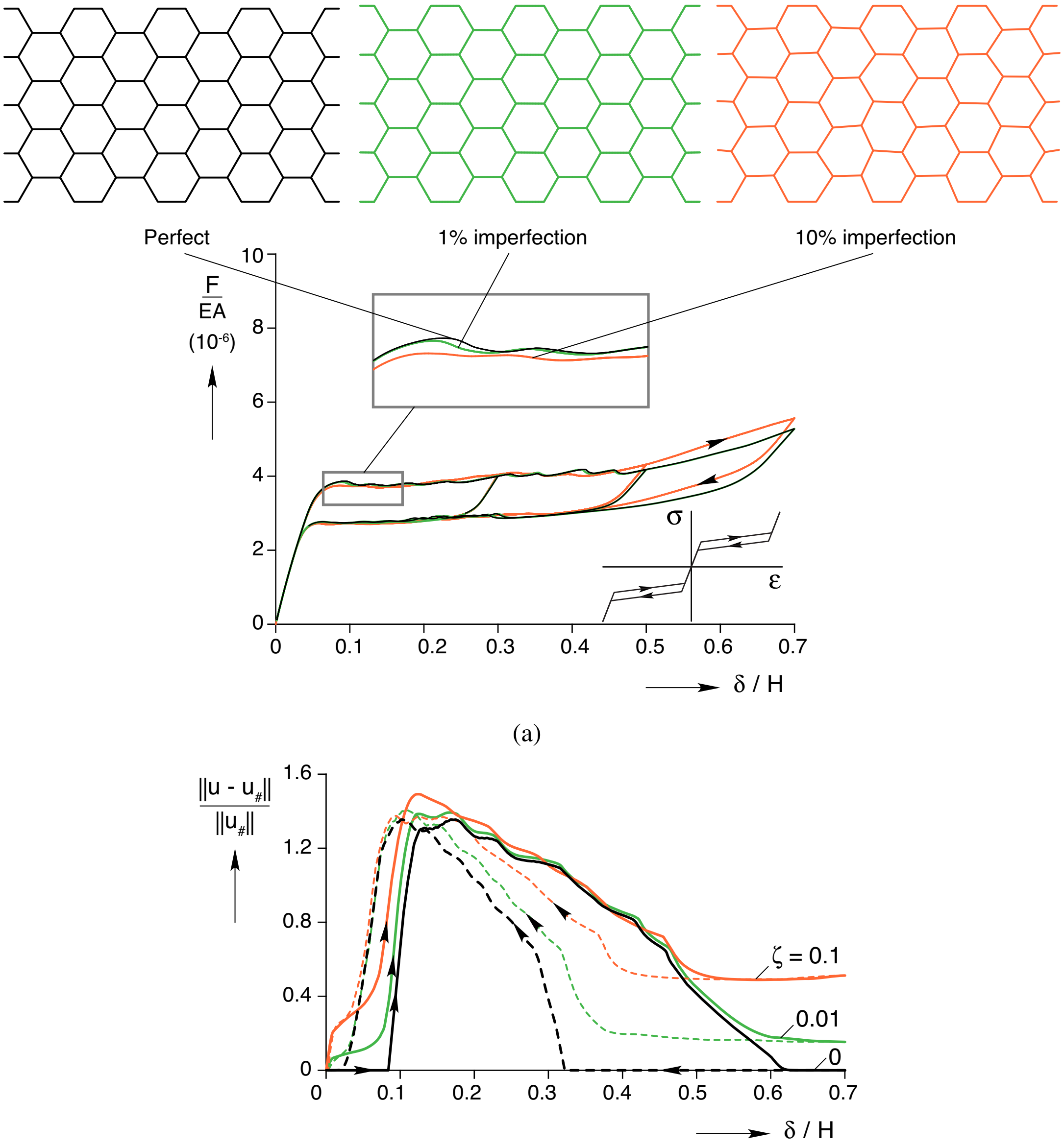

(a)

(b)

Figure 2.17: (a) Comparison of compressive loading-unloading responses for finite perfect and imperfect honeycombs ($\zeta = 0, 0.01, 0.1$) with a symmetric, hysteretic constitutive response (Model 1). (b) Relative deviation $\|\boldsymbol{u} - \boldsymbol{u}_\#\|/\|\boldsymbol{u}_\#\|$ of the finite perfect and imperfect honeycomb deformations vs. macroscopic compressive strain $(\delta/H)$.

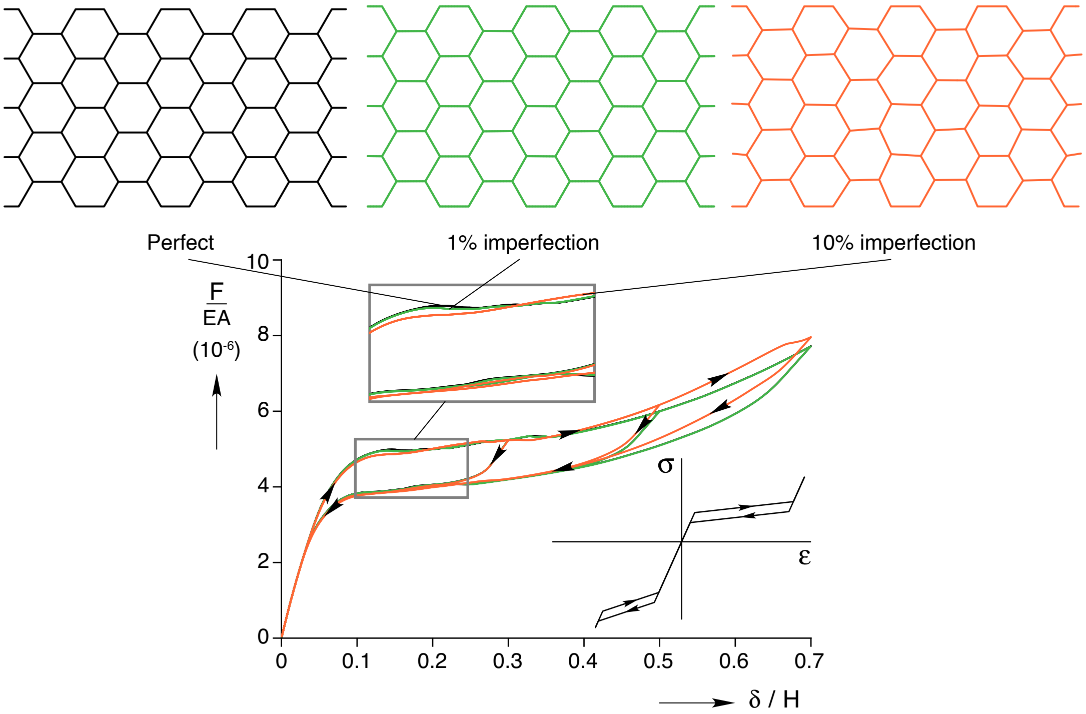

Figure 2.18: Comparison of compressive loading-unloading responses for finite perfect and imperfect honeycombs ($\zeta = 0, 0.01, 0.1$) with an asymmetric, hysteretic constitutive response (Model 2).

### 2.4.5 Response of the Fabricated Nitinol Honeycomb

Finally, we turn to superelastic simulations of an actual SMA honeycomb. All the above presented results pertain to various idealized SMA structures. The following results are calculated for the actual SMA honeycomb specimen shown in Figure 2.19(a), having overall in-plane dimensions $40.6 \times 21.5$ mm with 4-1/2×7 cells, out-of-plane depth $5.2$ mm, and nominal ligament thickness $t = 0.1$ mm, except for the double layer bonds at the horizontal lands. The uniaxial macroscopic stress-strain response to several compressive load cycles is shown in Figure 2.19(b) (data redrawn from Figure 5 of [26]). The actual geometry of the specimen in Figure 2.19(a) was digitized as accurately as possible and was discretized by up to 20 beam elements per ligament. The cell ligaments of the SMA honeycomb specimen are noticeably curved, especially at the junctions, thus requiring more finite elements to accurately capture the initial geometry.

The local stress-strain behavior of the as-fabricated honeycomb walls is, unfortunately, not directly available at this time, and this would be challenging task to obtain for a number of reasons. The post heat-treated properties are likely different from the virgin NiTi strip material used in their construction, so one would want properties of wall samples excised from the honeycomb. One could only hope to get tensile data, not compression data, since buckling would be difficult to avoid. Obtaining accurate bending data on such small specimens would also be difficult, and while potentially useful for local bending moment-curvature behavior, the true stress-strain behavior could still only be inferred indirectly. Furthermore, the specimen in the experiment exhibited noticeable shakedown behavior (as is commonly seen in uniaxial experiments of Nitinol, at least for initial loading cycles), and some permanent strain existed as the strain increments were increased. Nevertheless, experimental work to independently obtain meaningful material property data on individual ligaments will be pursued in the future.

Consequently, we chose cycle 6 of Figure 2.19(b), taken to 30 % strain, to simulate and performed several trial simulations with different material laws to calibrate Model 3. We recognize that our uniaxial constitutive model contains a large number of parameters that can be used to fit the specimen's response, so no claim is made currently that Model 3 is necessarily the optimal one. Considering the reasonable agreement with both the mechanical response and the deformation pattern observed in Fig. 2.20, however, indicates that it is a credible one. Furthermore, Model 3 has certain expected features of NiTi behavior, namely asymmetric tension-compression behavior with lower transformation stresses and larger transformation strains in tension vs. compression, yet both having positive tangent moduli consistent with material that has experienced some shakedown cycling. Overall, we believe we can proceed with some confidence to investigate the effects of boundary conditions and geometric imperfections.

Another "sticky" issue is the potential effects of platen-honeycomb friction at the top and bottom of the specimen, so friction was included in the simulations. A friction coefficient of $\mu = 0.3$ was chosen such that the response of the finite, imperfect honeycomb reasonably matched the experimental results. This value is considered realistic for the dry, steel platens used. The same model was simulated frictionless, in order to quantify the effect of friction as well as to be comparable to the finite sample results presented earlier. A frictional or standard contact algorithm was used for the two cases respectively, since the

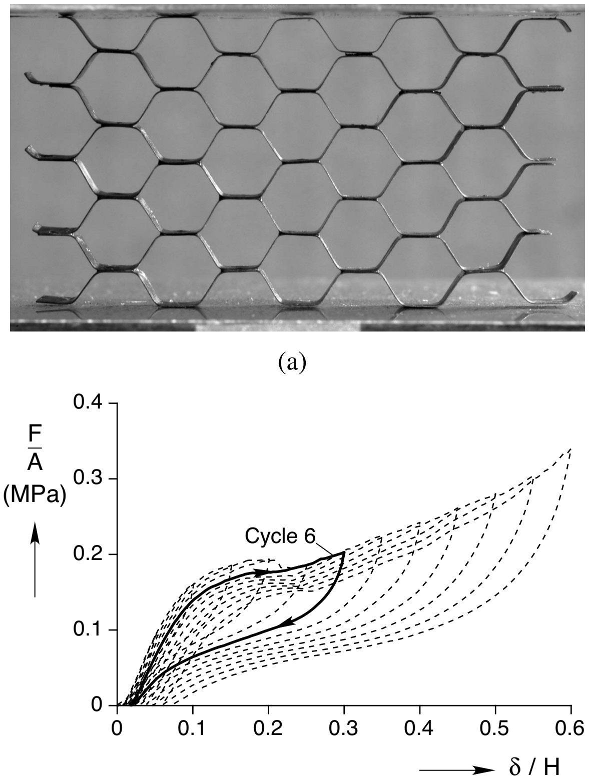

(a)

(b)

Figure 2.19: (a) Photograph of Nitinol honeycomb specimen. (b) Experimental isothermal compressive, displacement-controlled response subjected to load-unload cycles in progressively larger 5 % strain increments (data taken from Figure 5 of [26].)

actual honeycomb top and bottom surfaces were not precisely planar, causing some cells to contact the platens before others at the initiation of loading. This was the cause of the concave curvature and delayed upturn in the experimental response near $\delta/H = 0.01$, as settling occurs between the honeycomb top/bottom ends and the platens. After this "slack" was exhausted the structure stiffened to a roughly linear response up to about $\delta/H = 0.05$.

The case of $\mu = 0.3$ results in quite satisfactory agreement with the experimental response as seen in Figure 2.20(a). Not surprisingly, the presence of friction acts to stiffen the overall response as shown in the three responses of finite, imperfect honeycombs. The response of the infinite-perfect honeycomb is also shown for comparison, being the stiffest of the structures considered. Obviously, the presence of imperfections is a strong effect, softening the response considerably compared to the perfect case. All cases were stable for their entire paths for this choice of constitutive law (Model 3). The case of $\mu = 0.3$ for the finite, imperfect honeycomb fits the experimental results very well, except for a minor deviation near $\delta/H = 0.2$ during loading. Similarities are also apparent in Figure 2.20(b) between the simulated ($\mu = 0.3$) and experimental configurations near the maximum strain, $\delta/H = 0.3$. The overall shapes are roughly trapezoidal with cells flattened at the top, although the distortion is somewhat more severe in the experiment. Notice that the center cell in the bottom row is relatively undeformed in both cases. Overall, we consider the agreement between the simulation and experimental results to be quite satisfactory.

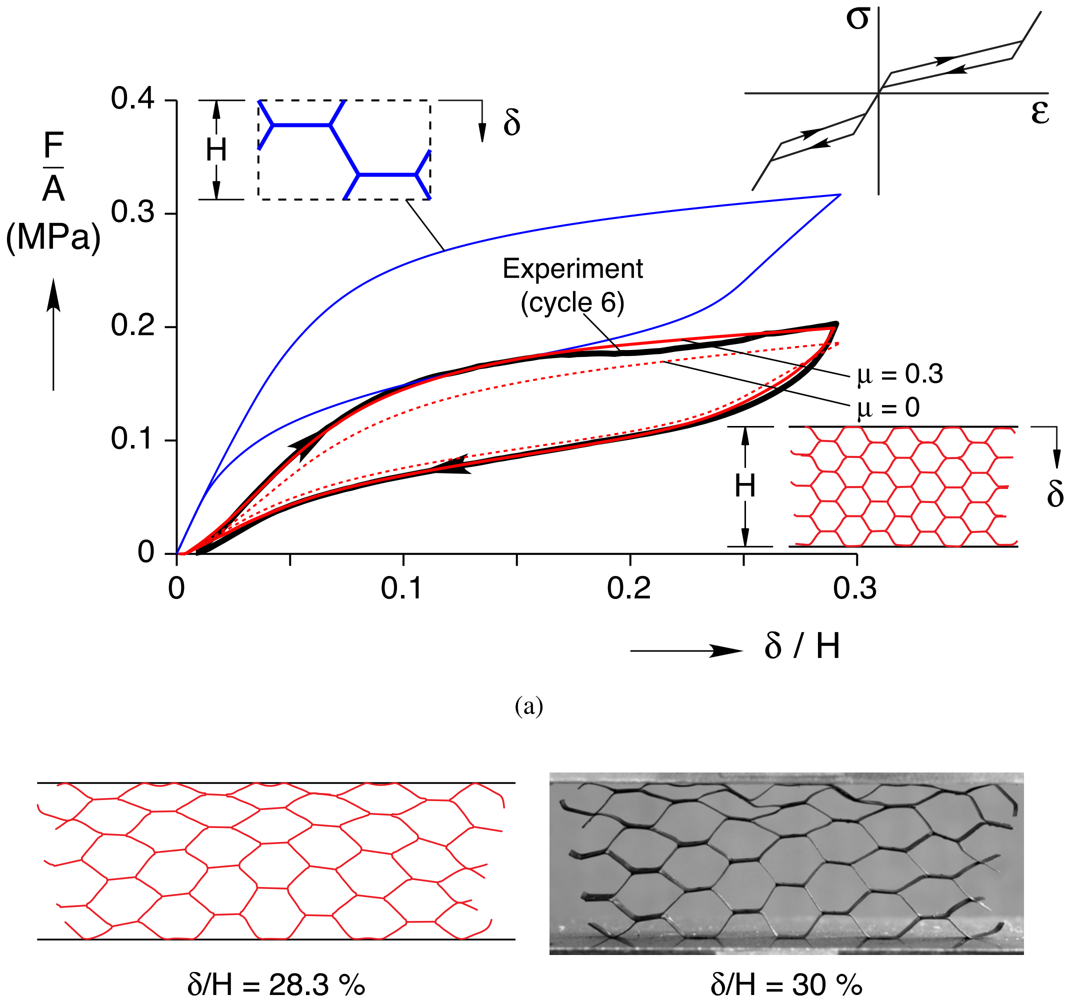

(a)

(b)

Figure 2.20: (a) Macroscopic load-unload stress-strain responses: experimental measurement from cycle 6 of Figure 2.19(b) (bold line) and FEM simulations (actual geometry using Model 3) with two values of friction coefficient, $\mu = 0$ (dotted line), $\mu = 0.3$ (thin solid line). The infinite-perfect honeycomb (upper left inset) principal path (thin line) is also shown for comparison. (b) Simulated configuration ($\mu = 0.3$) and experimental image near 30 % strain.

## Chapter III

# Design for Energy Absorption

Energy absorbers are used for packaging, crash or blast protection [3] in order to protect valuable, fragile components/occupants from damaging acceleration/decceleration. The origins of such accelerations may be a drop from a equipment handler, a parachute drop, a launch of a rocket, a vehicle crash or from a blast in a military situation. The function of the energy absorber is to absorb kinetic energy of a moving object (e.g delicate instruments or an armor plate) without transmitting a large stress. This is conventionally achieved by the use of hollow tubes, metal honeycombs (loaded parallel to the axis of the hexagonal cells) or metal foams, due to the long, flat stress-strain curve they exhibit when plastically crushed. The ideal design should have the greatest absorbed energy per unit volume or mass (or unit cost) while still not exceeding a given limit in transmitted stress.

While traditional absorbers are capable of offering protection to a valuable object, their use is limited to a single time, after which they are thrown away. This is because their attractive flat load-deflection curve comes at the cost of severe irreversible plastic deformation. Therefore, if protection is needed more than once, the damaged element has to be replaced, a task that could be costly or impossible (e.g for an element on a launched rocket).

In this Chapter, the superelasticity of SMA honeycombs is exploited in the design of energy absorbers, resulting into elements that can be repeatedly crushed without permanent damage. The simulation methods presented in Chapter II are adopted to examine the performance of different honeycomb designs. Using a parametrized hexagonal unit-cell, charts are constructed that guide the selection of parameters to accomplish optimal characteristics (e.g. maximum energy absorption per unit mass of honeycomb).

The design objectives and constraints of such a reusable energy absorption honeycomb are presented in the first Section. These are followed by the description of the type of unit cells that were considered in this study. Finally, the results of a parametric study are presented and conclusions are drawn.

## 3.1 Design Objectives

The objective of the design study is to specify the unit cell geometry of a honeycomb such that once crushed in its own plane, it absorbs the maximum kinetic energy per unit mass or volume[1]. In addition to absorbing kinetic energy, the honeycomb should satisfy two more constraints:

1. The honeycomb is not permanently damaged.
2. The maximum reaction force during crushing does not exceed a predefined limit.

---

[1] Although both objectives were investigated, only the absorbed energy per unit mass (more precisely absorbed energy per unit cell's material volume, which differs by a factor of the solid material's density) is presented in the parameter study in Section 3.3. For the absorbed energy per unit volume the reader is invited to consult Appendix A

The first requirement is equivalent to a restriction on the maximum local strain seen anywhere in the honeycomb. A calculation leading to a plot similar to one seen in Figure 2.3(c) can be used to detect the macroscopic strain $\left(\delta/H|_{\varepsilon_{\max}}\right)$ where this occurs, along the principal solution. If, however, the structure deviates from the principal path, more complex deformation modes, possibly exhibiting localizations, are expected. Since these configurations are difficult to predict due to the continuum of bifurcation points leading to a myriad of equilibrium paths, a conservative additional restriction is imposed here, namely not to crush the honeycomb past it's first bifurcation point. The corresponding macroscopic strain is denoted as $\left(\delta/H|_{\text{stability}}\right)$, and its prediction is made using the Bloch wave calculations of a unit cell.

There is an underlying assumption here, namely that the honeycomb is large enough to be modeled by an infinite one. This may be justified by the encouraging result presented in Figure 2.15(a), where the first bifurcation points for an infinite and a finite honeycomb are shown to be very close to each other, even though the finite case considered is only $4 \times 7\frac{1}{2}$ cells large. Similar agreement is captured in Figure 2.16 for a different constitutive law.

The second requirement essentially protects adjacent bodies (whose kinetic energy is being absorbed) from being overloaded. To satisfy this, first the reaction force (per reference area) of the honeycomb during crushing is monitored and once macroscopic strain reaches $\left(\delta/H|_{\varepsilon_{\max}}\right)$ or $\left(\delta/H|_{\text{stability}}\right)$, the maximum reaction value that has occurred is reported. Therefore, the performance of the honeycomb is 'rated' and different designs can be compared.

Upon determining the maximum allowable macroscopic strain, calculation of the energy absorbed by the honeycomb is a straightforward task. Specifically, from the dimensionless macroscopic stress - macroscopic strain plot for the unit cell, the dimensionless energy per unit cell enclosed volume[2] is just the area under the curve, namely

$$\frac{W}{EV} = \int_0^{\delta/H|_{\text{max}}} \frac{F\left(u\right)}{EA}\,\mathrm{d}u \tag{3.1}$$

where $\delta/H|_{\text{max}} = \min\{\ \delta/H|_{\text{stability}}\ ,\ \delta/H|_{\varepsilon_{\text{max}}}\}$. The modulus $E$ appearing here is taken as the austenite's modulus of elasticity ($E_A$). The absorbed energy is denoted by $W$, while $A$ is the reference area defined by the footprint of the unit cell. In the case when the dimensionless energy per unit material volume is sought:

$$\frac{W}{EV_{\text{mat}}} = \frac{1}{v_{\text{eff}}} \int_0^{\delta/H|_{\text{max}}} \frac{F(u)}{EA}\,\mathrm{d}u \tag{3.2}$$

with $v_{\text{eff}} = \frac{\text{volume of material in a cell}}{\text{overall volume of cell}}$. Equation 3.1 should be used when maximizing absorbed energy per overall honeycomb volume (homogenized energy density) is of interest, while Equations 3.2 is useful when maximizing absorbed energy per honeycomb mass (specific energy). For the latter, Equation 3.2 should be multiplied by $E$ and divided by NiTi density $\rho$, thus giving

$$\frac{W}{V_{\text{mat}}\rho} = \frac{E}{v_{\text{eff}}\rho} \int_0^{\delta/H|_{\text{max}}} \frac{F(u)}{EA}\,\mathrm{d}u \tag{3.3}$$

---

[2] To understand which volume is used, consider Figure 2.1(a). The rectangle defined by the diagonal 1-6, multiplied by the depth gives the enclosed volume of the unit cell.

Figure 3.1 plots the local strain vs. the macroscopic strain for a unit cell superelastic honeycomb, demonstrating the selection of the limiting macroscopic strain values $\left(\delta/H|_{\varepsilon_{\max}}\right)$ and $\left(\delta/H|_{\text{stability}}\right)$. Using the minimum of these (denoted as $\delta/H|_{\max}$), Figure 3.2 presents the calculation of the absorbed energy (shaded area) as well as the maximum dimensionless reaction force.

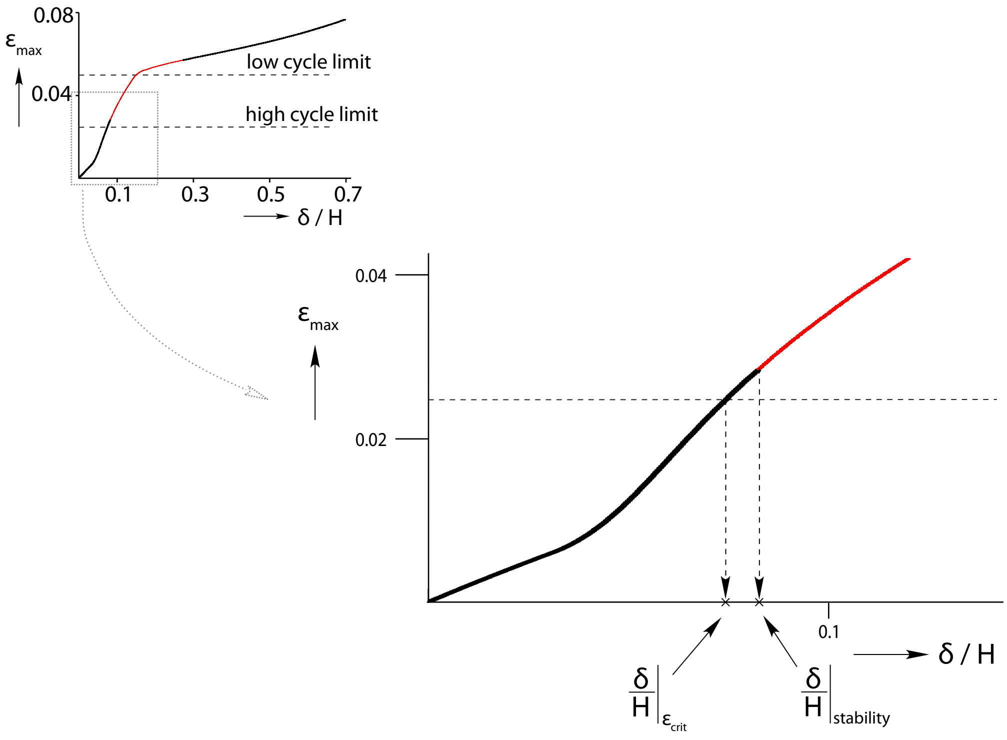

Figure 3.1: Principal branch of the maximum local strain $\varepsilon_{\max}$ seen anywhere in the structure vs. compressive strain $(\delta/H)$.

Repeating the above procedure for honeycombs of various shapes or material properties, a performance table can be constructed, that classifies each honeycomb according to its dimensionless energy absorption capability and the corresponding maximum dimensionless reaction. This is done later in this chapter, and convenient design contour plots are presented.

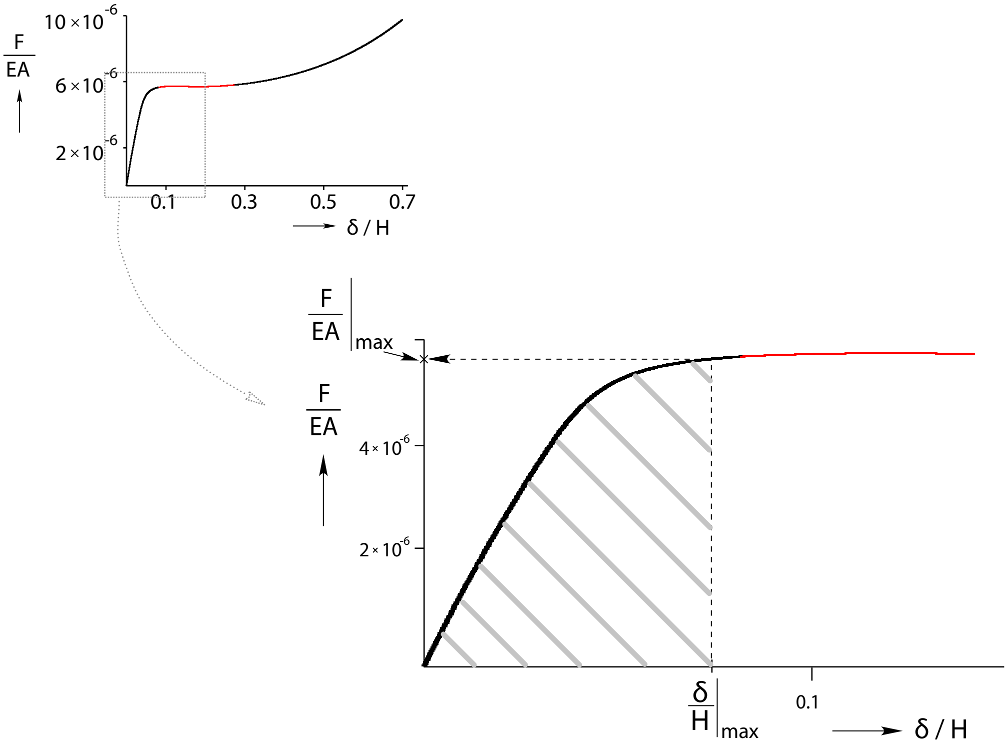

Figure 3.2: Calculation of the absorbed energy by compressing honeycomb up to $(\delta/H)|_{\text{max}}$.

Depending on the exact function of the honeycomb, other objectives and constraints could be employed. For example, in thermal actuator or positioning applications maximizing allowable macroscopic strain could be sought without any further constraints. Or, if thermal effects are taken into account, a larger material surface area to volume ratio could be desirable for fast actuation/reset operation.

## 3.2 Family of Shapes

The basic unit cell can be parametrized to give a family of shapes, covering from simple hexagonal to auxetic geometries. Two samples of this family are shown in Figures 3.3

and 3.4, along with the notation used for their dimensions. This generalized cell, while including as a subcase the standard hexagonal cell used in Chapter II, also can give radically different shapes (like the reentrant geometry shown in Figure 3.4) and still lend itself for manageable construction.

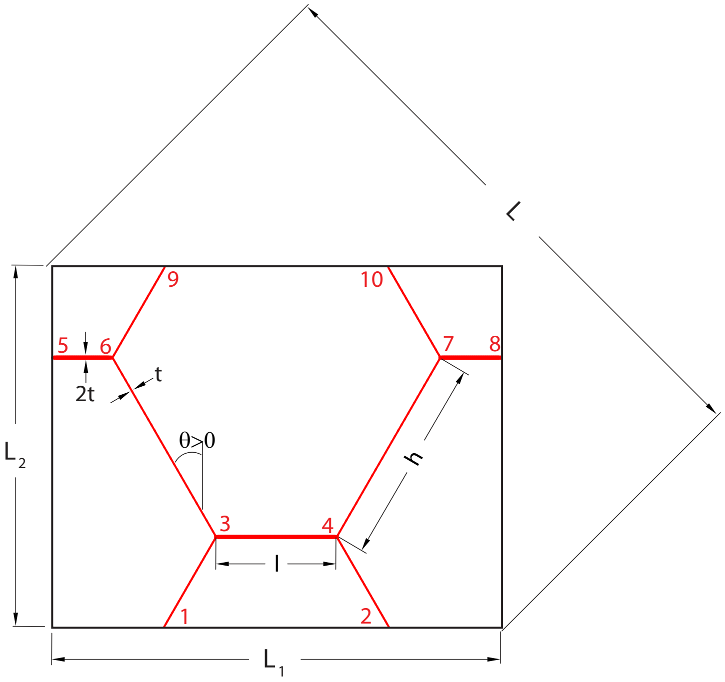

Figure 3.3: Sample of unit cell used in parameter study for energy absorption, showing the definition of some useful parameters. Here a case with $\theta > 0$ is depicted.

Four parameters are necessary to fully describe the cell. A fixed diagonal dimension is assumed ($L = 1$), a size measure that is independent of the exact shape of the cell. The aspect ratio of the unit cell's circumscribed rectangle is now treated as a free parameter, i.e $r = L_2/L_1$. Lastly, the wall thickness (expressed as $t/h$) and the angle $\theta$ of the slanted ligament are used to fully describe the cell (a unit out-of-plane depth is assumed). Keeping the number of cases to study at a relatively low number, the parameter values described in

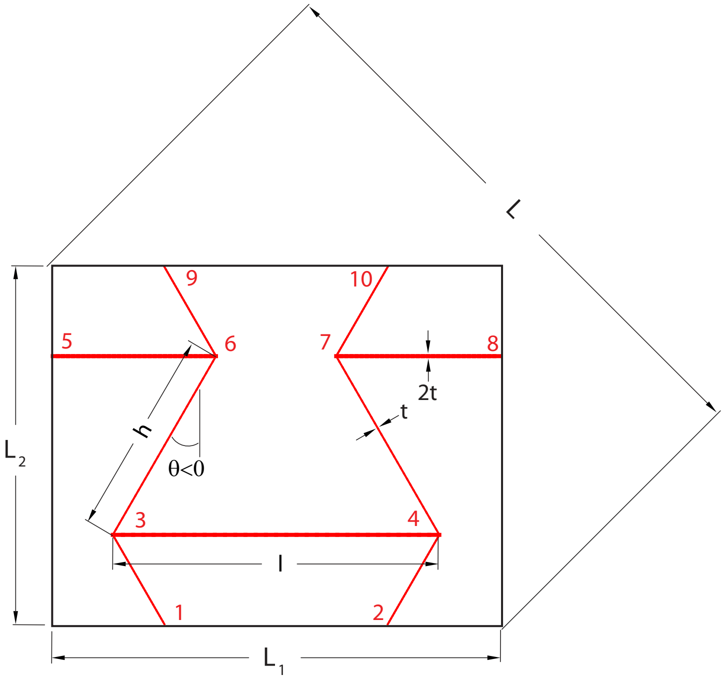

Figure 3.4: Sample of unit cell used in parameter study for energy absorption, showing the definition of some useful parameters. Here a case with $\theta < 0$ is depicted.

Table 3.1 were selected.

Table 3.1: Unit cell geometry parameter values

| Parameter | Values |
|---|---|
| $L$ | 1 |
| $\theta$ | $\pm 15^\circ \quad \pm 30^\circ$ |
| $r$ | $0.1\,,0.3\,,\sqrt{3}/3\,,0.6\,,0.9\,,1.2\,,1.5\,,1.8\,,2.1\,,2.4\,,2.7\,,3.0$ |
| $t/h$ | $0.005\,,0.010\,,0.020\,,0.040\,,0.060\,,0.080\,,0.100$ |

One should realize that combinations of very high aspect ratios $r$ with $\theta < 0$ lead to non-physical geometries (i.e interpenetrating geometries). Those combinations are naturally excluded from the calculations. It should also be mentioned here that when $\theta < 0$ (re-entrant cells) an additional constraint has to be added to the ones described in Section 3.1.

During compression, contact may occur between the joints of the opposing slanted walls. Although this could be modeled, in reality the two joints would slip towards opposing (vertical) directions, thus the honeycomb would leave the principal path. This mode could interact with slips in neighboring cells and lead to an unpredictable global mode for a large honeycomb. Therefore, consistent with the conservative approach outlined in Section 3.1, an additional constraint for the re-entrant geometries is to terminate the simulation once contact occurs.

## 3.3 Energy Absorption Results

Applying the methodology described in Section 3.1 in honeycombs with all the different unit cells presented above, and plotting the results leads to a design aid for a honeycomb energy absorber. These are presented in Figures 3.5–3.12 in the form of contour plots. Although the objective chosen here is maximization of absorbed energy per unit material volume, the alternative criterion of absorbed energy per overall volume is considered in Appendix A. For the study, the basis constitutive law (Model 1, see Section 2.3.1 for constitutive parameter values) is adopted.

For each of the four values of the angle $\theta$ correspond two contour plots. One using a limiting maximum local strain of 0.025, associated with high cycle loading-unloading, and one with maximum local strain of 0.05, more appropriate for few harder blows. For the case of $\theta = \pm 30^\circ$, the aspect ratio has to be limited to $r \leq 1.5$ to guarantee physically meaningful shapes (interpenetrating geometries occur otherwise). In total, 42 simulations were used to construct each of the $\theta = \pm 30^\circ$ plots while 77 for the $\theta = \pm 15^\circ$ (in total 238 runs).

Each plot contains contours of dimensionless absorbed energy per unit cell material volume ($\frac{W}{EV_{\text{mat}}}$, solid lines) for different combinations of the thickness ($t/h$) and cell aspect ratio ($r$, $y$-axis) parameters of the unit cell used. Overlaid on the same plot, contours of the maximum dimensionless reaction force appear ($\frac{F}{EA}\Big|_{\text{max}}$) as dotted lines.

The designer should start by locating the contour (dotted line) of the maximum allowable dimensionless reaction $\frac{F}{EA}\Big|_{\text{max}}$. Along this path, the $(t/h\,,\,r)$ region with the highest absorbing dimensionless energy ($\frac{W}{EV_{\text{mat}}}$, solid contour lines) is the most desirable one. After that, the precise values of the $(t/h\,,\,r)$ parameters to be selected may be influenced by other considerations, like thermal performance or any safety margin in the design.

As an example, assume that the optimal energy absorber with a unit cell that has $\theta = 15^\circ$ is sought. The absorber is to remain operating even after many cycles of loading-unloading, but the maximum transmitted dimensionless stress is not allowed to exceed $10 * 10^{-6}$ (i.e. $\frac{F}{EA} \leq 10 * 10^{-6}$). Consulting Figure 3.5 one locates the dotted contour corresponding to 10 and finds that the plot region with the highest absorbed energy (of $5 * 10^{-6}$) corresponds to $r = 3$ and $t.h = 0.04$. Any other area either has a lower energy absorbing capacity or violates the low stress requirement.

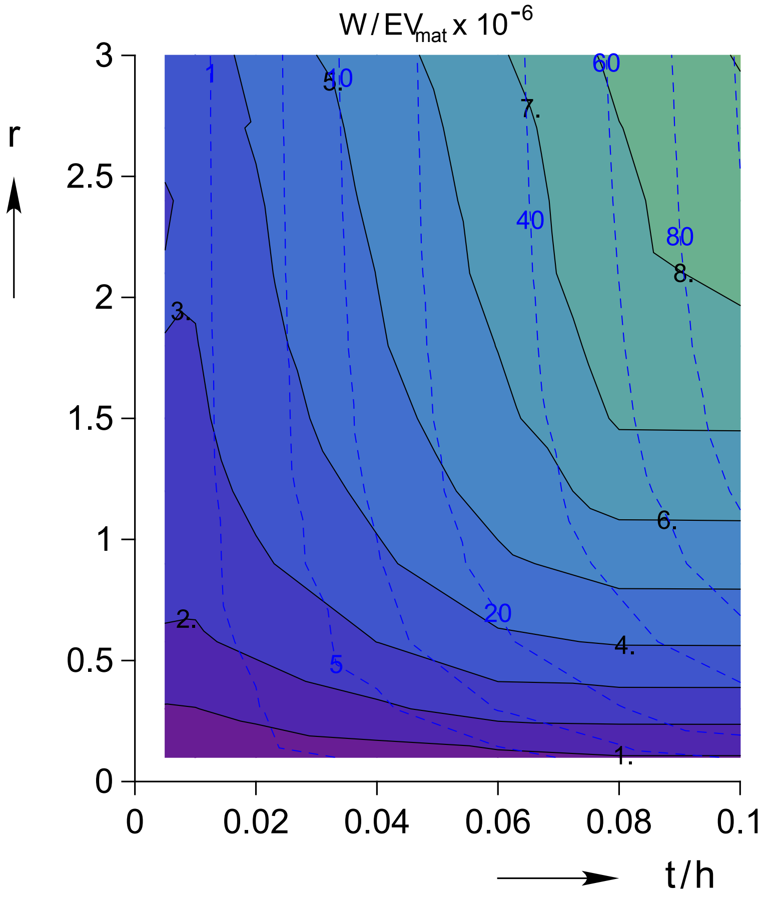

Figure 3.5: Design chart of dimensionless energy absorption per unit cell material volume for cells with $\theta = 15°$. A limiting local strain value of $\varepsilon_{\max} = 0.025$ is assumed.

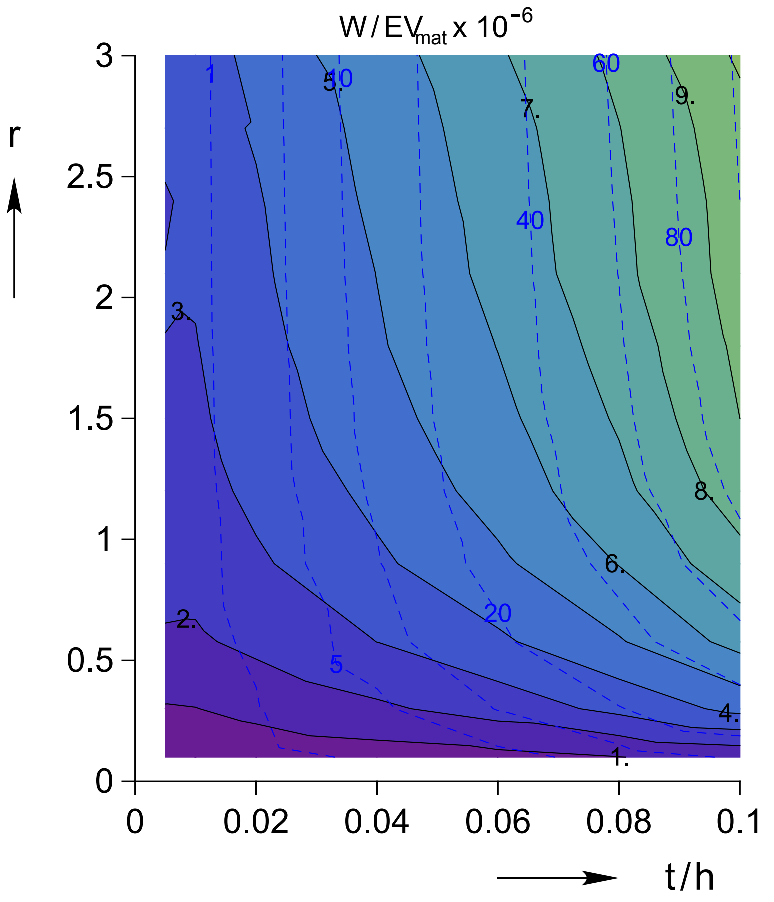

Figure 3.6: Design chart of dimensionless energyabsorption per unit cell material volume for cells with $\theta = 15°$. A limiting local strain value of $\varepsilon_{\max} = 0.050$ is assumed.

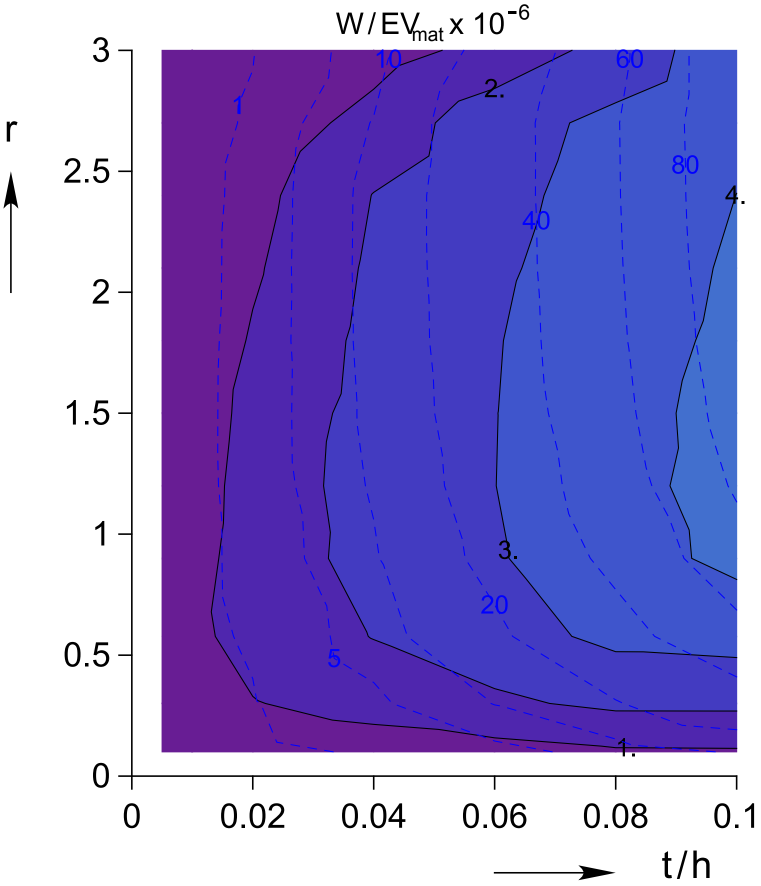

Figure 3.7: Design chart of dimensionless energy absorption per unit cell material volume for cells with $\theta = -15°$. A limiting local strain value of $\varepsilon_{\max} = 0.025$ is assumed.

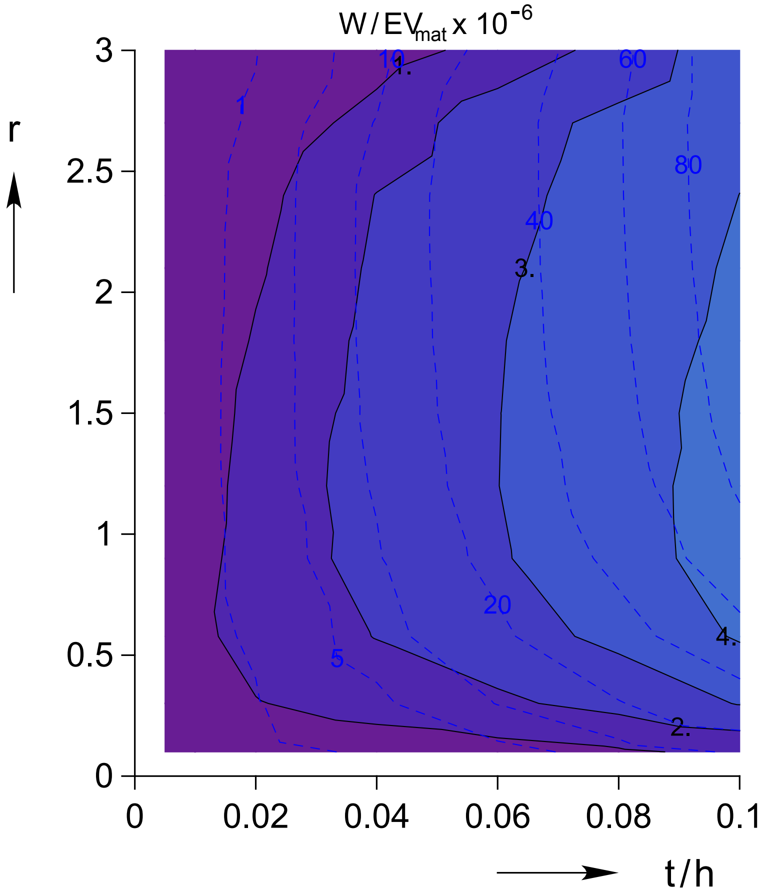

Figure 3.8: Design chart of dimensionless energy absorption per unit cell material volume for cells with $\theta = -15°$. A limiting local strain value of $\varepsilon_{\text{max}} = 0.050$ is assumed.

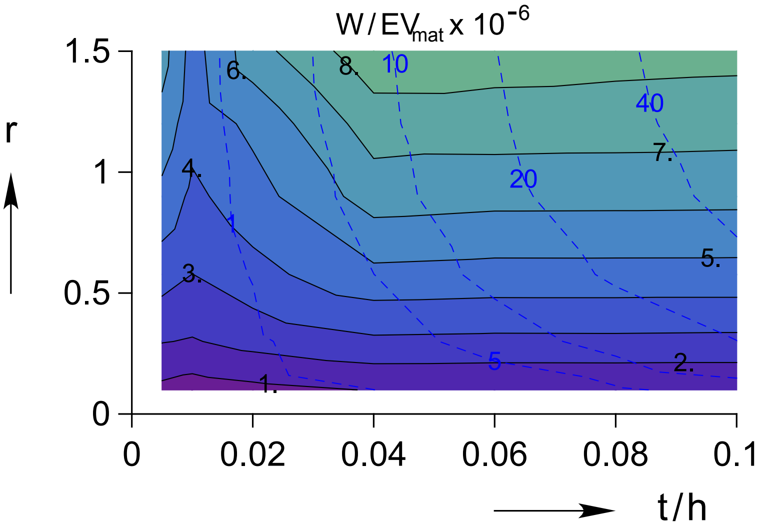

Figure 3.9: Design chart of dimensionless energy absorption per unit cell material volume for cells with $\theta = 30°$. A limiting local strain value of $\varepsilon_{\max} = 0.025$ is assumed.

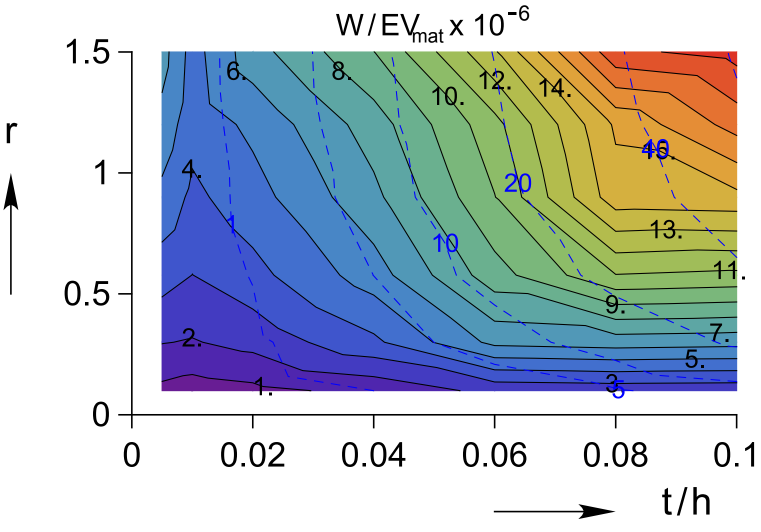

Figure 3.10: Design chart of dimensionless energy absorption per unit cell material volume for cells with $\theta = 30°$. A limiting local strain value of $\varepsilon_{\max} = 0.050$ is assumed.

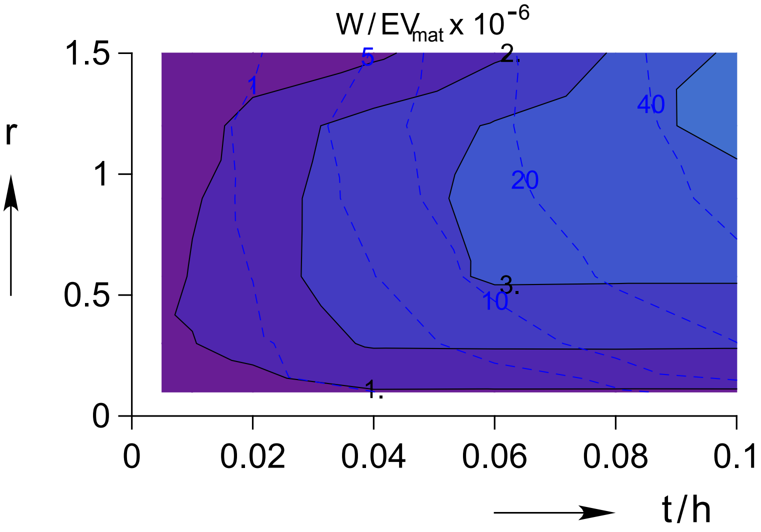

Figure 3.11: Design chart of dimensionless energy absorption per unit cell material volume for cells with $\theta = -30°$. A limiting local strain value of $\varepsilon_{\max} = 0.025$ is assumed.

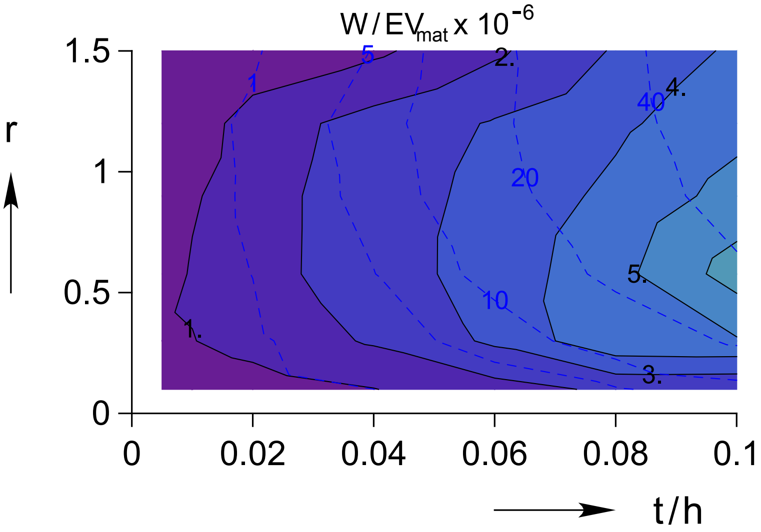

Figure 3.12: Design chart of dimensionless energy absorption per unit cell material volume for cells with $\theta = -30°$. A limiting local strain value of $\varepsilon_{\max} = 0.050$ is assumed.

Studying Figure 3.5, which corresponds to cells with $\theta = 15°$ and a limiting local strain value of $\varepsilon_{\text{max}} = 0.025$, one concludes that for a given limit in reaction force, the optimal cells have the highest possible aspect ratio $r = 3$. An exception occurs in the region with $r \approx 2.5$ and $t/h \approx 0.01$. Although there is a tendency for short wavelength instability modes for higher $r$'s and lower $t/h$'s, in the aforementioned region exists an 'island' of long wavelength modes. Since long wavelength modes can be associated with lower energies than the short wavelength ones, they also probably occur earlier as well, thus undermining further compression of the cells and energy absorption. Yet, one should note that the sparsity of parameters grid used in the study is not adequately dense to study such a small region in detail, thus no conclusive explanation can be given.

As expected, increasing the limiting local strain value at $\varepsilon_{\text{max}} = 0.050$ (Figure 3.6), allows further compression of cells with high thickness ratios $t/h$. Even then though, the increased allowed local strain cap is not fully exploited, since instabilities precede.

In the case of $\theta = -15°$, one immediately deduces that energy absorption per unit cell material volume is substantially lower (Figures 3.7 and 3.8). These cells are severely limited by instability. The C-shape of the contours is the result of increase in absorbed energy (per unit cell's material volume) as the aspect ratio $r$ increases, and the abrupt limiting in further compression due to contact for the highest values of $r$. By the increase of the allowable local strain value at $\varepsilon_{\text{max}} = 0.050$, only few cells with low aspect ratios $r$ and high thickness ratios $t/h$ benefit.

Superior performance is observed for the cells with $\theta = 30°$ (Figures 3.9 and 3.10). Again, cells with high $t/h$ ratios are limited by local strain development in bending ligaments, while for low $t/h$ instability precedes. A striking observation is the high energy absorption of these cells for $t/h = 0.01$ compared to the ones with $t/h = 0.02$. The very thin walled cells surprisingly showed no instabilities even when compressed down to 0.7 macroscopic strain. For the cells with $\theta = -30^{\circ}$ (Figures 3.11 and 3.12) the C-shaped contours that appear resemble those of their $-15^{\circ}$ counterparts. Same explanation holds.

Overall, superior performance is observed for the cells with $\theta = 30^{\circ}$. Overall, the lightest energy absorber, among the cases studied, would almost certainly have $\theta = 30^{\circ}$, $r \rightarrow 1.5$, and $t/h$ dictated from the maximum allowable reaction. Interestingly, this points towards a rhombic unit cell, but such a case is not considered here.

The guidelines provided above pertain to maximizing absorbed energy per unit cell material volume, a figure-of-merit to be adopted when the honeycomb's mass is of concern. Alternatively, if limitation of the honeycomb's volume is of concern, one could maximize the absorbed energy per unit cell overall volume. Such results are included in Appendix A. Additionally, the overall poisson ratio of the honeycomb at maximum allowable macroscopic strain is shown there (for more details refer to Appendix A).

## Chapter IV

# Shape Memory Honeycombs

## 4.1 Introduction

The previous chapters addressed only the isothermal superelastic behavior of SMA honeycombs. This chapter presents a first step to extend the material model/FEA to simulate shape memory behavior of SMA honeycombs that could be used in future actuator applications and smart structures.

There is an abundance of shape memory alloy constitutive models in the literature. Roughly categorizing some recent efforts, there are those which use volume fractions of martensite variants to capture continuum-level behavior [2,13], polycrystalline microstructural models [21], Ginzburg-Landau models to simulate microstructural evolution [1], and even quantum-mechanical models to evaluate the relative stability of different crystal structures [16,34].

In this chapter, the constitutive law used in the simulations is a 1D phenomenological model, similar to the one proposed in [25]. The 1D continuum model is based on a free energy function that involves two internal field variables (two variants of martensite phase fractions) and is adequate to capture the SMA behavior in uniaxial experiments. The model is based on [4], but is modified to ignore time-dependent effects and to stabilize its response.

The material is organized as follows: First the SMA constitutive model used is presented, followed by a discussion of its numerical implementation. The last section presents results of calculations of an SMA honeycomb structure.

## 4.2 Constitutive Model

In this section a thermodynamically-based SMA constitutive model is described. The model is based on a 1-D Helmholtz free energy with two internal variables to identify phase fractions and is used to model the essentially uniaxial loading of the SMA honeycomb cell walls. Three phases are considered: two variants of martensite ($M^+$ and $M^-$), with mass fractions of $\xi_1$ and $\xi_2$ respectively, and austenite ($A$) with mass fraction $\xi_3$. The model is based on [4] but has been modified mostly to exclude strain gradient effects and to enable control of the slope of (isothermal) transformation paths. Also, no rate effects are taken into account in the version employed here, consistent with the quasi-static thermomechanical loading of the SMA honeycomb experiments of interest [29].

For simplicity, the tensile and compressive response of the material is assumed to be the same. Furthermore, the assumption is made that pure austenite and saturated martensite (either variant) have the same elastic modulus. While employing an asymmetric in tension-compression constitutive law would have an effect on a honeycomb's response (as demonstrated earlier for the superelastic case, see Chapter II), adopting a different modulus for pure austenite and pure martensite proved to have a minor effect in the response of a compressed honeycomb (at least for the macroscopic strain levels investigated in this thesis).

In what follows, $\boldsymbol{\xi}$ denotes the phase fraction vector $(\xi_1, \xi_2)$.

### 4.2.1 Phase fraction space

Three phases are present: two martensitic, with mass fractions $\xi_1$ and $\xi_2$ and an austenitic with mass fraction $\xi_3$. These can be represented graphically by a point in the $(\xi_1, \xi_2)$ space by a vector $\boldsymbol{\xi}$, given that mass conservation dictates $\xi_3 = 1 - \xi_1 - \xi_2$. Each phase can have a mass fraction from $0$ to $1$, therefore the admissible region for them is a triangle as shown in grey in Figure 4.1. In the same figure, the numbering adopted for the vertices and edges is shown, along with the unit normal and tangential vectors for each edge (useful in determining phase evolution described later). Thus, pure austenite $(A)$ is mapped on vertex 1, tensile martensite $(M^+)$ on vertex 2, compressive martensite $(M^-)$ on vertex 3, while twinned martensite $\left(M^{+/-}\right)$ with same mass fraction of each variant, is represented by the point $(\xi_1, \xi_2) = (0.5, 0.5)$.

As an example of the path followed in $\boldsymbol{\xi}$ space during a phase transformation cycle, consider the superelastic transformation path modeled in Chapter II. This would take place along the edges 3 (for tension) and 2 (for compression). A more involved path exhibiting the shape memory effect is shown in Figure 4.2. Material initially at $(\xi_1, \xi_2) = (0.5, 0.5)$ (twinned martensite) is loaded in tension and thus de-twinns (vertex 2). Upon unloading there is no phase transformation, therefore material is still mapped at vertex 2 in the $(\xi_1, \xi_2)$ space. Heating transforms martensite into austenite (path from vertex 2 to 1) and subsequent cooling brings the material back to twinned martensite.

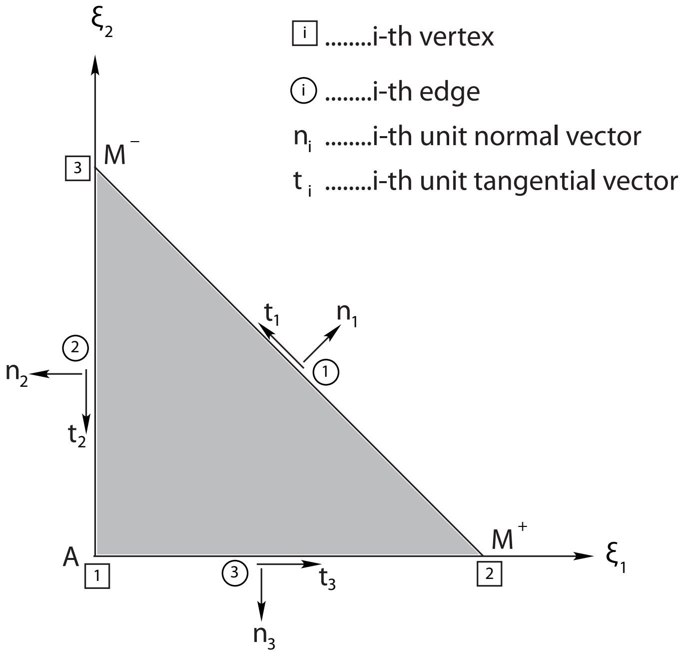

Figure 4.1: Phase fraction space notation used in the text.

### 4.2.2 Free energy

The specific Helmholtz free energy, a function of small strain $\varepsilon$, temperature $T$ and internal variables $\boldsymbol{\xi}$ is decomposed into the following additive parts

$$\phi(\varepsilon, T, \boldsymbol{\xi}) = \phi_E(\varepsilon, \boldsymbol{\xi}) + \phi_C(T, \boldsymbol{\xi}) + \phi_I(\boldsymbol{\xi}) + \phi_T(T) \tag{4.1}$$

where $\phi_E$ is the elastic energy, $\phi_C$ is the chemical energy, $\phi_I$ is the temperature-independent interaction energy, and $\phi_T$ is the phase-independent thermal energy. These are chosen to

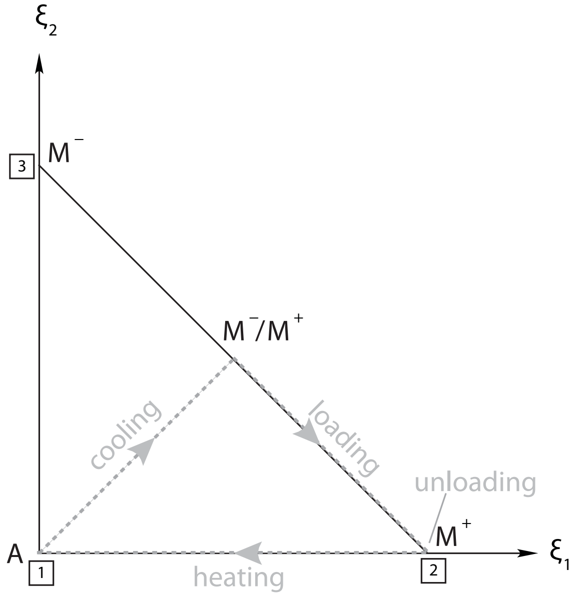

Figure 4.2: Transformation path exhibiting the shape memory effect.

be

$$
\begin{aligned}
\phi_E(\varepsilon, \boldsymbol{\xi}) &= \frac{\beta E}{\varrho} \left[\varepsilon - (\xi_1 - \xi_2)\beta\right]^2 \\
\phi_C(T, \boldsymbol{\xi}) &= -(T - T_R)(\xi_1 + \xi_2)\Delta s \\
\phi_I(\boldsymbol{\xi}) &= c_I(1 - \xi_1 - \xi_2)(\xi_1 + \xi_2) + c_{II}(\xi_1 - \xi_2)^2 \\
\phi_T(T) &= (c_0 - s_0)(T - T_R) - c_0 T \, ln\left(\frac{T}{T_R}\right) \qquad (4.2)
\end{aligned}
$$

In the above, $T_R$ is a reference transformation temperature, $\Delta s$ is the specific entropy change from austenite to martensite which is related to the latent heat of transformation and is a negative constant, and $s_0$ and $c_0$ are material constants representing the phase-independent specific entropy and specific heat respectively. The elasticity modulus $E$ used is that of austenite (i.e $E = E_A$), density is represented by $\rho$, while $\beta$ is the transformation strain (see Figure 2.2 for definition in the asymmetric superelastic case). The constants

$c_I$ and $c_{II}$ allow the adjustment of the isothermal slope of the pseudoelastic as well as the low-temperature transformation path (detwinning) enabling thus a stable or unstable mechanical behavior, as will be discussed subsequently.

Satisfaction of the non-negativity of entropy production for the system (see [5]) leads to the following relations

$$\begin{aligned} s &= -\phi_{,T} = s_0 + (\xi_1 + \xi_2)\Delta s + c_0\, ln \left(\frac{T}{T_R}\right) \\ \sigma &= \rho\phi_{,\varepsilon} = E\left[\varepsilon - (\xi_1 - \xi_2)\,\beta\right] \\ \boldsymbol{\mu}\boldsymbol{\cdot}\dot{\boldsymbol{\xi}} &= -\phi_{,\boldsymbol{\xi}}\boldsymbol{\cdot}\dot{\boldsymbol{\xi}} \geq 0; \quad \boldsymbol{\mu} \equiv -\phi_{,\boldsymbol{\xi}} \end{aligned} \tag{4.3}$$

where $\boldsymbol{\mu}$ is the chemical driving force with components given by

$$\begin{aligned} \mu_1 &= \frac{E\beta}{\rho}\left[\varepsilon - (\xi_1 - \xi_2)\,\beta\right] + \Delta s\,(T - T_R) - c_I\,(1 - 2\xi_1 - 2\xi_2) - 2c_{II}\,(\xi_1 - \xi_2) \\ \mu_2 &= -\frac{E\beta}{\rho}\left[\varepsilon - (\xi_1 - \xi_2)\,\beta\right] + \Delta s\,(T - T_R) - c_I\,(1 - 2\xi_1 - 2\xi_2) + 2c_{II}\,(\xi_1 - \xi_2) \end{aligned} \tag{4.4}$$

### 4.2.3 Kinetic law

The kinetic law adopted confines phase evolution to occur in the direction of the chemical driving force, while keeping phase fractions within the admissible region described in Section 4.2.1.

For convenience, the unit vector $\boldsymbol{m}$ is defined depending on the current phase fraction values and the direction of the chemical driving force. If the phase fraction coordinates reside in the interior of the admissible region then

$$\boldsymbol{m} = \boldsymbol{\mu}/\|\mu\| \tag{4.5}$$

where $\|\mu\| \equiv \sqrt{\boldsymbol{\mu} \bullet \boldsymbol{\mu}}$. If the phase fraction coordinates reside on an edge (but not a corner) of the admissible region, then

$$\boldsymbol{m} = \begin{cases} \boldsymbol{\mu}/\|\mu\| & \text{if} \quad \boldsymbol{\mu} \bullet \boldsymbol{n}^{(i)} < 0 \\ \boldsymbol{t}^{(i)} & \text{if} \quad \boldsymbol{\mu} \bullet \boldsymbol{n}^{(i)} \geq 0 \end{cases} \tag{4.6}$$

Please consult Figure 4.1 for notation of unit normals $\boldsymbol{n}^{(i)}$ and unit tangents $\boldsymbol{t}^{(i)}$ used here. Finally, in the case where the current phase fraction resides in a corner of the admissible region, then

$$\boldsymbol{m} = \begin{cases} \boldsymbol{\mu}/\|\mu\| & \text{if} \quad \boldsymbol{\mu} \bullet \boldsymbol{n}^{(i)} < 0 \quad \text{and} \quad \boldsymbol{\mu} \bullet \boldsymbol{n}^{(j)} < 0 \\ \boldsymbol{t}^{(k)} & \text{if} \quad \boldsymbol{\mu} \bullet \boldsymbol{n}^{(k)} \geq 0 \quad \text{and} \quad \boldsymbol{\mu} \bullet \boldsymbol{t}^{(k)} > 0 \quad \text{for} \quad k = i \quad \text{or} \quad j \\ \boldsymbol{0} & \text{otherwise} \end{cases} \tag{4.7}$$

From the above it is clear that, in general, the unit vector $\boldsymbol{m}$ points in the direction of the chemical driving force $\boldsymbol{\mu}$, unless some phase fraction reaches a maximum (i.e. $\xi_1$ and/or $\xi_2$ and/or $\xi_3 = 1$ ) and $\boldsymbol{\mu}$ still points outwards of the admissible zone. In those cases, $\boldsymbol{m}$ points along the corresponding edge if $\boldsymbol{\mu}$ has a component along that edge, otherwise it is defined as zero ($\boldsymbol{0}$).

Now, the kinetic law is defined as

$$\dot{\boldsymbol{\xi}} = \begin{cases} \mathbf{0} & \text{if} \quad \boldsymbol{\mu} \bullet \boldsymbol{m} < \mu_c \quad \text{(no transformation)} \\ k\boldsymbol{m} & \text{if} \quad \boldsymbol{\mu} \bullet \boldsymbol{m} = \mu_c \quad \text{(transformation)} \end{cases} \tag{4.8}$$

The parameter $\mu_c$ (critical driving force) is introduced to model the hysteretic behavior of the material and is a positive constant. Also, $k$ is a positive quantity (because of the last of Equations 4.3), the calculation of which is to be described bellow. In contrast to [4], there is no ”stiffness” appearing in the second equation above, since rate effects are not considered. Essentially this kinetic law evolves the phase fraction if the magnitude of the driving force (or its component defined by $\boldsymbol{\mu} \bullet \boldsymbol{m}$ if constrained on an edge or corner) exceeds the critical value $\mu_c$. Thus, in quasi-static conditions considered here, during transformation it is $\boldsymbol{\mu} \bullet \boldsymbol{m} = \mu_c$. This leads to a consistency condition, namely

$$\dot{\boldsymbol{\mu}} \bullet \boldsymbol{m} = \mathbf{0} \tag{4.9}$$

Substitution of Equation 4.4 in the above expression, results in a differential equation for the phase fraction $\boldsymbol{\xi}$. Since during phase transformation it is $\dot{\boldsymbol{\xi}} = k\boldsymbol{m}$, one gets finally an algebraic equation to solve for $k$. More details in the numerical implementation of the model are given later.

### 4.2.4 Illustrative examples of material model behavior

A positive tangent modulus along isothermal transformation paths of the material is a desirable property that facilitates computations. This section investigates the relation between this property and the corresponding form of the free energy. It should also be noted that a positive tangent modulus is not only desirable, but is also experimentally observed in 1D SMA low temperature loading, or even at high temperature loading after some training of the material [17].

Letting, for now, the temperature-independent interaction energy $\phi_I$ be of general form, the chemical driving force can be written as

$$\begin{aligned}
\mu_1 &= \frac{E\beta}{\rho}\left[\varepsilon - \left(\xi_1 - \xi_2\right)\beta\right] + \Delta s\left(T - T_R\right) - \partial\phi_I/\partial\xi_1 \\
\mu_2 &= -\frac{E\beta}{\rho}\left[\varepsilon - \left(\xi_1 - \xi_2\right)\beta\right] + \Delta s\left(T - T_R\right) - \partial\phi_I/\partial\xi_2
\end{aligned} \tag{4.10}$$

For the rest of this subsection, the subscript $I$ in $\phi_I$ will be dropped when partial differentiation is performed, for example $\phi_{,1} \equiv \partial\phi_I/\partial\xi_1$. Now, as mentioned after (4.8), during transformation it is $\boldsymbol{\mu}\boldsymbol{\cdot}\boldsymbol{m} = \mu_c$, thus differentiating

$$\dot{\boldsymbol{\mu}}\boldsymbol{\cdot}\boldsymbol{m} = 0 \tag{4.11}$$

Combining (4.10) with (4.11) the following result is obtained

$$\dot{\varepsilon} = \frac{-\Delta s\left(m_1 - m_2\right)\dot{T} - \left[-\dfrac{E\beta^2}{\rho} - \left(\phi_{,11}m_1^2 + \phi_{,22}m_2^2 + 2\phi_{,12}m_1m_2\right)\right]}{\dfrac{E\beta}{\rho}\left(m_1 - m_2\right)} \tag{4.12}$$

Now, differentiating the stress relation from (4.3) gives for the slope of the stress-strain response

$$\frac{\dot{\sigma}}{\dot{\varepsilon}} = E\left[1 - \frac{\dot{\xi}_1 - \dot{\xi}_2}{\dot{\varepsilon}}\right] \tag{4.13}$$

Thus, the tangent modulus along isothermal transformation paths can be computed from (4.12) and (4.13) by setting $\dot{T} = 0$, i.e

$$E_t \equiv \left.\frac{\dot{\sigma}}{\dot{\varepsilon}}\right|_{\dot{T}=0} = E\left[1 - \frac{\dfrac{E\beta^2}{\rho}\left(m_1 - m_2\right)^2}{\dfrac{E\beta^2}{\rho}\left(m_1 - m_2\right)^2 - \left(\phi_{,11}m_1^2 + \phi_{,22}m_2^2 + 2\phi_{,12}m_1m_2\right)}\right] \tag{4.14}$$

From the above result, it is clear that the form of the temperature-independent interaction energy $\phi_I$ can be used to tailor the tangent modulus along the isothermal transformation paths. Requiring that $E_t > 0$ (which, as mentioned, is observed for trained SMA) is equivalent to $(\phi_{,11}m_1^2 + \phi_{,22}m_2^2 + 2\phi_{,12}m_1m_2) > 0$, since $m_1$ and $m_2$ are components of a unit vector with arbitrary direction. The above requirement can be written also as

$$\begin{vmatrix} \phi_{,11} & \phi_{,12} \\ \phi_{,21} & \phi_{,22} \end{vmatrix} \equiv det\left(H_\phi\right) > 0 \quad \text{and} \quad \phi_{,11} > 0 \tag{4.15}$$

where $H_\phi$ is the Hessian of $\phi_I\left(\xi_1, \xi_2\right)$.

For the form of $\phi_I$ adopted in (4.2) the denominator appearing in (4.14) becomes

$$\frac{E\beta^2}{\rho}\left(m_1 - m_2\right)^2 - 2\left[c_I\left(m_1 + m_2\right)^2 - c_{II}\left(m_1 - m_2\right)^2\right] \tag{4.16}$$

and it turns out that the requirement stated in (4.15) reduces to

$$c_I c_{II} < 0 \quad \text{and} \quad c_{II} - c_I > 0 \tag{4.17}$$

which also means that $c_{II} > 0 > c_I$.

In order to illustrate the way the values of $c_I$ and $c_{II}$ can be used to tailor $E_t$ in the isothermal limit, several transformation paths are considered. First, for high-temperature transformation of austenite to martensite ($A \rightarrow M^+$ or $A \rightarrow M^-$ depending if load is tensile or compressive respectively), one has $m_1 = 1$ and $m_2 = 0$ for $A \rightarrow M^+$ or $m_1 = 0$ and $m_2 = 1$ for $A \rightarrow M^-$ respectively. In both cases (4.14) gives

$$E_t^{A \rightarrow M} = E \left[ 1 - \frac{\dfrac{E\beta^2}{\rho}}{\dfrac{E\beta^2}{\rho} + 2\left(c_{II} - c_I\right)} \right] \tag{4.18}$$

On the other hand, for low temperature isothermal detwinning of martensite one has $m_1 = 1/\sqrt{2}$ and $m_2 = -1/\sqrt{2}$ (or $m_1 = -1/\sqrt{2}$ and $m_2 = 1/\sqrt{2}$ for the compressive case) and (4.14) gives

$$E_t^{M^{+/-} \rightarrow M} = E \left[ 1 - \frac{\dfrac{E\beta^2}{\rho}}{\dfrac{E\beta^2}{\rho} + 2c_{II}} \right] \tag{4.19}$$

Adopting the requirements described from (4.17) guarantees that $E_t > 0$ for all possible paths. Note, however, that since $c_{II} - c_I > c_{II}$ it is also $E_t^{A \rightarrow M} > E_t^{M^{+/-} \rightarrow M}$.

## 4.3 Implementation of model

This section gives some details on the numerical implementation of the material model presented in Section 4.3. For simplicity, only configurations with spatially uniform temperatures are considered.

### 4.3.1 Newton-Raphson Scheme

In the absence of applied external forces, i.e. for displacement or temperature imposed loading, the Principle of Virtual Work for cellular structures with one-dimensional response considered here, can be written as

$$\int \sigma\left(\varepsilon, T, \boldsymbol{\xi}\right) \delta\varepsilon \, \mathrm{d}V = 0 \tag{4.20}$$

where the integral is taken first over the thickness of each cell wall and then over the length of all cell walls for the entire structure. The internal variables $\boldsymbol{\xi}$ are functions of temperature, strain and their history, i.e $\boldsymbol{\xi} = \boldsymbol{\xi}(\varepsilon, T, t)$, where $t$ denotes the fictitious time of the problem.

After incrementing the load, a perturbed strain and temperature field is assumed, consistent with the essential boundary conditions. The equilibrium statement now is

$$\int \sigma\left(\varepsilon_\eta, T_\eta, \boldsymbol{\xi}_\eta\right) \delta\varepsilon \, \mathrm{d}V = 0 \tag{4.21}$$

where

$$\begin{aligned} \varepsilon_\eta &= \varepsilon + \eta\Delta\varepsilon \\ T_\eta &= T + \eta\Delta T \\ \boldsymbol{\xi}_\eta(\varepsilon, T) &= \boldsymbol{\xi}(\varepsilon_\eta, T_\eta) \end{aligned} \tag{4.22}$$

Linearizing about the previous equilibrium solution requires calculation of

$$\frac{d}{d\eta}\int \sigma\left(\varepsilon_\eta, T_\eta, \boldsymbol{\xi}_\eta\right)\delta\varepsilon\,\mathrm{d}V\bigg|_{\eta=0} \tag{4.23}$$

with

$$\sigma\left(\varepsilon_\eta, T_\eta, \boldsymbol{\xi}_\eta\right) = E\varepsilon_\eta - E\beta\left(\xi_{\eta 1} - \xi_{\eta 2}\right) \tag{4.24}$$

In order to calculate $\frac{d}{d\eta}\boldsymbol{\xi_\eta}$ the kinetic equation 4.8 is considered (only the nontrivial case where phase evolution occurs is discussed here). Adopting a forward Euler integration scheme between the previous equilibrium and the current perturbed state, the kinetic law gives

$$\boldsymbol{\xi}_\eta - \boldsymbol{\xi} = \Delta k\boldsymbol{m} \tag{4.25}$$

where $\Delta k \equiv \Delta t k$ and $\Delta t$ is the time increment. In a similar fashion, the consistency condition 4.9 implies

$$\left(\boldsymbol{\mu}_\eta - \boldsymbol{\mu}\right)\bullet\boldsymbol{m} = 0 \tag{4.26}$$

or

$$\begin{aligned}&\left(\frac{E\beta}{\rho}\begin{Bmatrix}1\\-1\end{Bmatrix}\left(\varepsilon_\eta-\varepsilon\right)+\Delta s\begin{Bmatrix}1\\1\end{Bmatrix}\left(T_\eta-T\right)\right.\\&+\left.\begin{bmatrix}-\dfrac{E\beta^2}{\rho}+2\left(c_I-c_{II}\right) & \dfrac{E\beta^2}{\rho}+2\left(c_I+c_{II}\right)\\ \dfrac{E\beta^2}{\rho}+2\left(c_I+c_{II}\right) & -\dfrac{E\beta^2}{\rho}+2\left(c_I-c_{II}\right)\end{bmatrix}\begin{Bmatrix}\xi_{\eta 1}-\xi_1\\ \xi_{\eta 2}-\xi_2\end{Bmatrix}\right)\bullet\boldsymbol{m}=0\end{aligned} \tag{4.27}$$

The last two equations can be combined to give

$$\Delta k = a\eta\Delta\varepsilon + b\eta\Delta T \tag{4.28}$$

with

$$\begin{aligned} & a \equiv -\frac{A}{C} \quad , \quad b \equiv -\frac{B}{C} \\ & A \equiv \frac{E\beta}{\rho}\left(m_1 - m_2\right) \quad , \quad B \equiv \Delta s\left(m_1 + m_2\right) \quad , \quad C \equiv \begin{bmatrix} m_1 & m_2 \end{bmatrix} [W] \begin{Bmatrix} m_1 \\ m_2 \end{Bmatrix} \end{aligned} \tag{4.29}$$

Therefore now

$$\boldsymbol{\xi}_\eta = \boldsymbol{\xi} + a\eta\Delta\varepsilon\boldsymbol{m} + b\Delta T\eta\boldsymbol{m} \tag{4.30}$$

and

$$\frac{d}{d\eta}\boldsymbol{\xi}_\eta = a\Delta\varepsilon + b\Delta T \tag{4.31}$$

Using this result, one may now calculate 4.23, since

$$\frac{d}{d\eta}\,\sigma\left(\varepsilon_\eta, T_\eta, \boldsymbol{\xi}_\eta\right)\Big|_{\eta=0} = E\Delta\varepsilon + \hat{a}\Delta\varepsilon + \hat{b}\Delta T \tag{4.32}$$

where the following definitions are used

$$\hat{a} \equiv E\beta\left(m_2 - m_1\right)a \quad , \quad \hat{b} \equiv E\beta\left(m_2 - m_1\right)b \tag{4.33}$$

As a consequence of the above, linearizing 4.21 about the previous equilibrium solution gives

$$\int \delta\varepsilon \left[E + \hat{a}\right] \Delta\varepsilon \,\mathrm{d}V = -\int \delta\varepsilon \left[\sigma + \hat{b}\Delta T\right] \,\mathrm{d}V \tag{4.34}$$

Upon discretization this leads to the tangent stiffness matrix $\boldsymbol{K}$, the increments in the displacive degrees of freedom $\Delta\boldsymbol{u}$ and the force vector $\boldsymbol{F}$, thus

$$\boldsymbol{K}\Delta\boldsymbol{u} = \boldsymbol{F} \tag{4.35}$$

## 4.4 Shape Memory Simulations

### 4.4.1 1D Element Simulations

A simple 1-dimensional element thermomechanical loading simulation is presented first, serving two purposes: to exhibit the shape memory behavior of the material model as well as to help verify the validity of the implementation. In order to isolate the material's behavior, only one beam element is used (the same type of element used everywhere else in this thesis) and is loaded in pure tension.

Material properties used are presented in Table 4.1. Each Gauss point of the element has 3 material integration points through the thickness since the load is uniform through the cross section.

The thermomechanical loading process modeled is shown in the strain, temperature and stress space in Figure 4.3. Initially ($t = 0$, where $t$ denotes artificial time for the Newton Raphson procedure), the temperature is below the reference one, namely $T/T_R = 0.81428$.

Keeping it fixed, the element is loaded mechanically to $\varepsilon = 0.06$ macroscopic strain using displacement control ($t = 1$). During this procedure the twinned martensite is fully detwinned. Subsequently, switching to force control the element is unloaded. At this point, there is an apparent permanent deformation of the element of $\varepsilon = 0.0572$ macroscopic strain ($t = 2$). Keeping the axial force to zero, the temperature is raised to $T/T_R = 1.17529$, resulting in the transformation of the material into austenite while erasing any apparent deformation ($t = 3$). Now, at this higher temperature, a load-unload cycle is performed ($t = 3$–$5$), demonstrating the superelastic behavior of the material model (displacement control is used again). Finally the temperature is reduced back to the initial one ($T/T_R = 0.81428$), transforming the material back to twinned martensite and bringing the element in its exact initial configuration ($t = 6$). The whole process shown in Figure 4.3 uses 3000 equal load parameter increments.

Table 4.1: Shape memory model material properties: dimensionless groups' definitions and given values

| Quantity | Dimensionless Group | Value |
|---|---|---|
| $\overline{E}$ | $E/E$ | 1 |
| $\overline{\beta}$ | $\beta$ | 0.0572 |
| $\overline{\rho}$ | $\rho/\rho$ | 1 |
| $\overline{\Delta s}$ | $\Delta s \rho T_R/E$ | -0.00155443 |
| $\overline{T_R}$ | $T_R/T_R$ | 1 |
| $\overline{c_I}$ | $c_I \rho/E$ | -0.000065 |
| $\overline{c_{II}}$ | $c_{II} \rho/E$ | 0.000027857 |
| $\overline{\mu_c}$ | $\mu_c \rho/E$ | 0.000093785714 |

For the above process, the history of the phase fractions is shown in Figure 4.4 in the $(\xi_1\,,\,\xi_2)$ space (showing phase changes during corresponding time intervals) and in

Figure 4.5 for each fraction separately with respect to time.

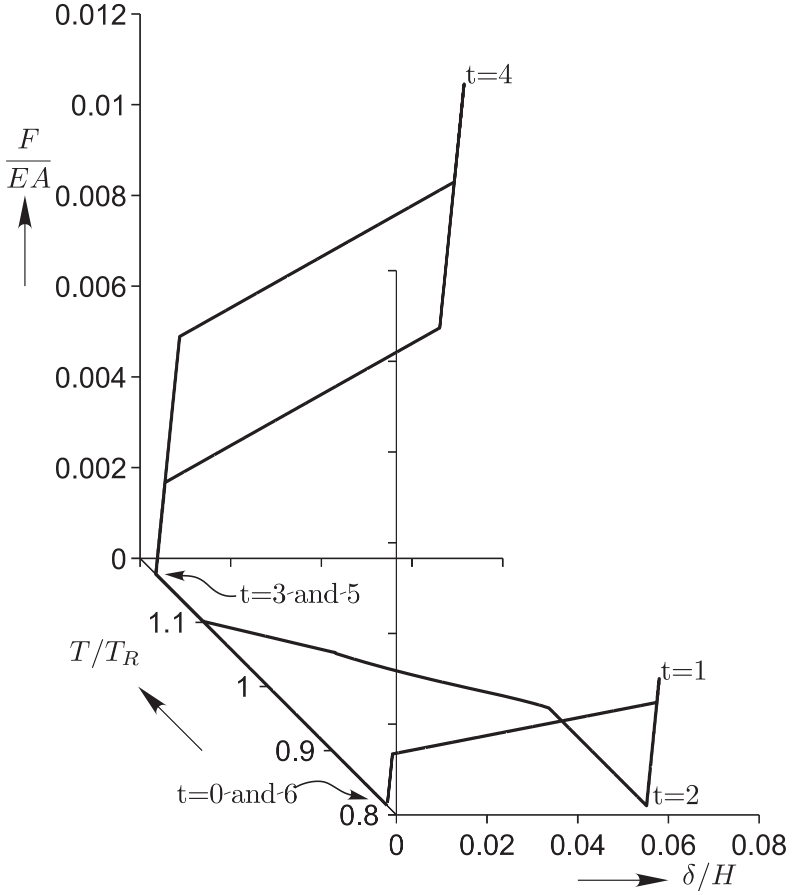

Figure 4.3: Shape memory effect and pseudoelastic response exhibited by tensile loading of one finite element.

Using the chemical driving force equations (4.4) it is easy to compute the exact stress-strain values of the initiation and saturation of transformations for both twinned martensite to detwinned one, as well as asutenite to martensite and back to austenite. These points are denoted in Figure 4.6 with capital letters A–G.

For point A, using the evolution requirement $\boldsymbol{\mu} \bullet \boldsymbol{m} = \boldsymbol{\mu_c}$ and setting $\boldsymbol{m} = \big(\sqrt{2}/2\,,\,-\sqrt{2}/2\big)$ the corresponding strain can be evaluated for $(\xi_1\,,\,\xi_2) = (0.5\,,\,0.5)$. Similarly, for point B the same equation is used with $(\xi_1\,,\,\xi_2) = (1.0\,,\,0.0)$. For the rest of the points, the reader is invited to consult Table 4.2.

Table 4.2: Initiation and saturation points for transformation due to mechanical loading of SMA material

| Point | Equilibrium equation | $(m_1\,,\,m_2)$ | $(\xi_1\,,\,\xi_2)$ | $T$ | $(\sigma\,,\,\varepsilon)$ |
|---|---|---|---|---|---|
| A | $\boldsymbol{\mu}\bullet\boldsymbol{m}=\mu_c$ | $\left(\sqrt{2}/2\,,\,-\sqrt{2}/2\right)$ | $(0.5\,,\,0.5)$ | 0.81428 | $(0.001159\,,\,0.001159)$ |
| B | $\boldsymbol{\mu}\bullet\boldsymbol{m}=\mu_c$ | $\left(\sqrt{2}/2\,,\,-\sqrt{2}/2\right)$ | $(1.0\,,\,0.0)$ | 0.81428 | $(0.002296\,,\,0.05950)$ |
| C | by design | | | | $(0.0\,,\,0.0572)$ |
| D | $\boldsymbol{\mu}\bullet\boldsymbol{m}=\mu_c$ | $(1.0\,,\,0.0)$ | $(0.0\,,\,0.0)$ | 1.17529 | $(0.005266\,,\,0.005266)$ |
| E | $\boldsymbol{\mu}\bullet\boldsymbol{m}=\mu_c$ | $(1.0\,,\,0.0)$ | $(1.0\,,\,0.0)$ | 1.17529 | $(0.008676\,,\,0.06587)$ |
| F | $\boldsymbol{\mu}\bullet\boldsymbol{m}=-\mu_c$ | $(1.0\,,\,0.0)$ | $(1.0\,,\,0.0)$ | 1.17529 | $(0.005397\,,\,0.06260)$ |
| G | $\boldsymbol{\mu}\bullet\boldsymbol{m}=-\mu_c$ | $(1.0\,,\,0.0)$ | $(0.0\,,\,0.0)$ | 1.17529 | $(0.001988\,,\,0.001988)$ |

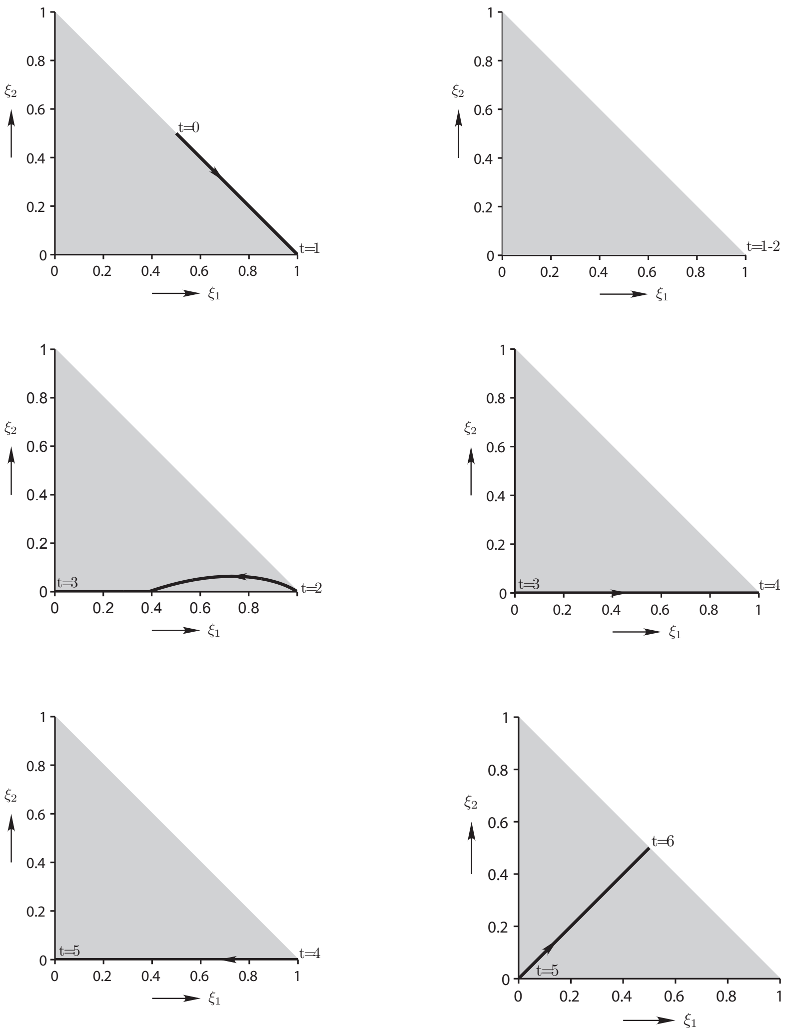

Figure 4.4: Phase fractions history presented in phase fraction space, during thermomechanical process described in Figure 4.3.

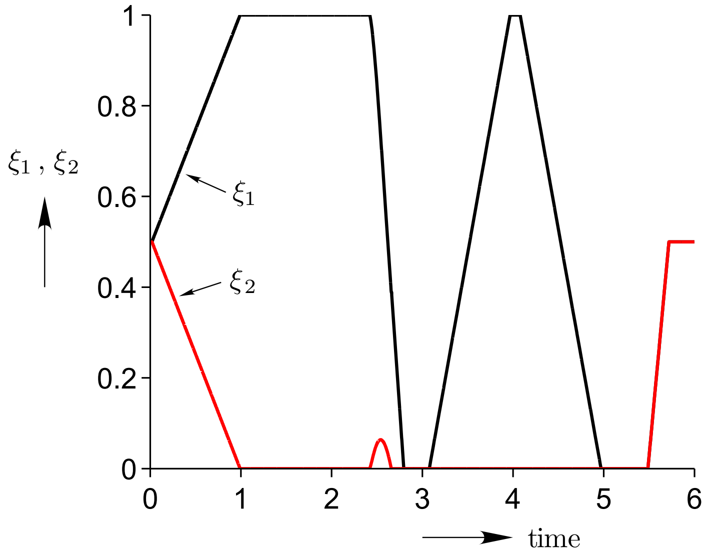

Figure 4.5: Phase fractions history during process presented in Figure 4.3.

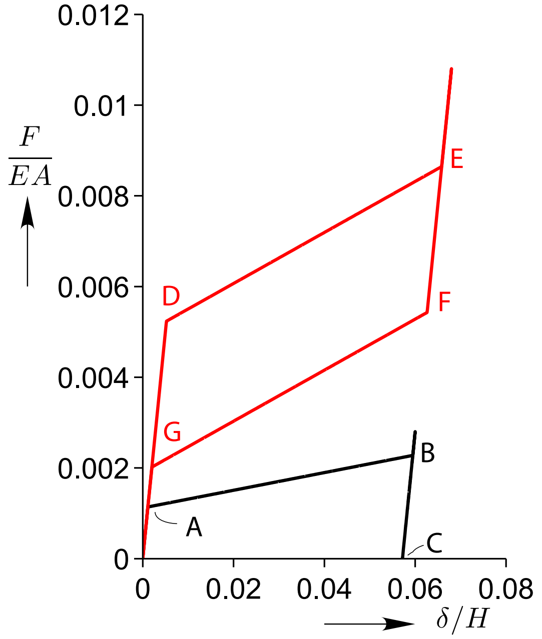

Figure 4.6: Stress-strain response of 1 element in tension for two different temperatures. Curve with letters A,B,C corresponds to detwinning of martensite, while D,E,F,G is at a higher temperature (pseudoelastic behavior).

### 4.4.2 Honeycomb Structures Simulations

As illustrative simulations of a shape memory alloy cellular structure, two cases are considered. First, the principal solution for a hexagonal honeycomb undergoing the same thermomechanical process as the one described in Section 4.4.1 is calculated. Then, the simulation is repeated for a finite size SMA honeycomb structure (the $4 \times 7\frac{1}{2}$ used in the superelastic case), in order to simulate the response along the same thermomechanical loading cycle.

#### Principal Solution

As an illustrative example of a shape memory alloy cellular solid, the principal solution for a hexagonal honeycomb is considered undergoing the same thermomechanical process as the one described in Section 4.4.1. The result is presented in Figure 4.7.

Since only the principal solution of the honeycomb is of interest, a quarter of its unit cell is modeled (see inset of Figure 4.7) with 50 elements per wall length $L$. The same structural model introduced in Chapter II is used. The top and bottom nodes of the cell are controlled following the sequential displacement and force control pattern used in the 1D problem considered above. Material properties used are presented in Table 4.1. For the whole process 9000 loading increments are used. Each element's Gauss point uses 51 material integration points through the thickness of the beam.

The result of the simulation is presented in Figure 4.7. The high temperature isothermal response is similar to what has been presented earlier in Chapter II. The loading portion of the low temperature part of the simulation resembles that of a superelastic case with modified material properties. This should not be a surprising finding, since, if the reasonable assumption of monotonic material loading is made, the relevant part of the SMA constitutive law (namely, part (0,0)-A-B of curve in Figure 4.6) can be represented by the loading part of a superelastic response (i.e, part (0,0)-D-E of curve in Figure 4.6, but with modified properties so that $D \equiv A$ and $E \equiv B$).

For the chosen material parameters and temperature, once unloaded there is an apparent permanent deformation. That is erased during heating, while cooling brings the model exactly to its initial state.

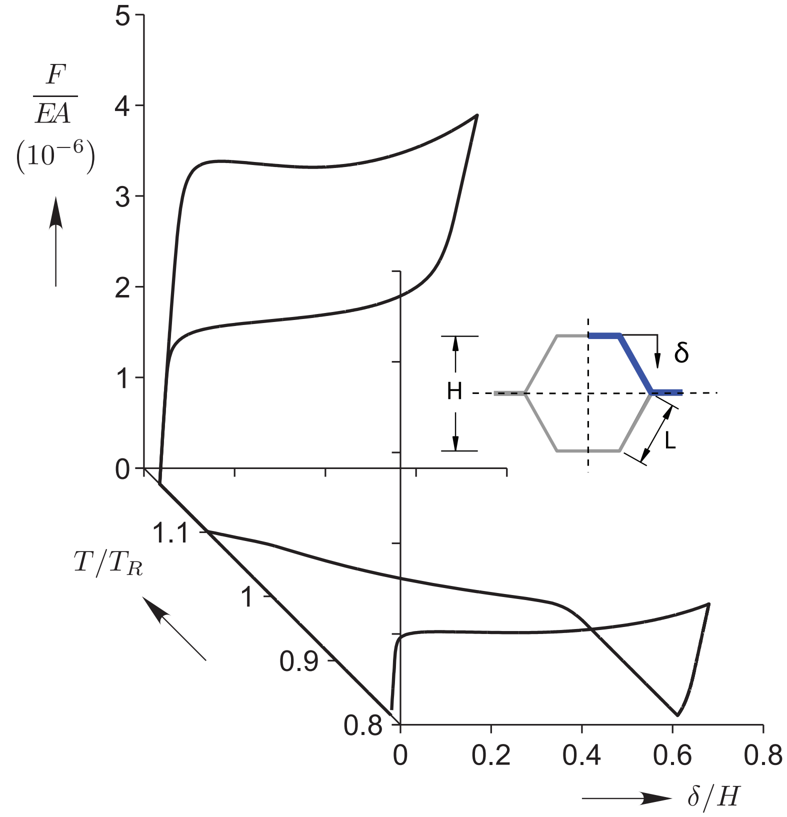

Figure 4.7: Shape memory effect and pseudoelastic response for the principal solution of a hexagonal honeycomb. One quarter of the unit cell is modeled.

### Response of finite honeycomb

A finite $4 \times 7\frac{1}{2}$ specimen is modeled in the same thermomechanical process the quarter cell underwent above. The result is shown in Figure 4.8. Deformed configurations of the honeycomb at instances depicted with a numbered tag in this plot, appear in Figures 4.9,4.10 and 4.11. This time, fewer degrees of freedom were used, namely 10 elements per wall length $L$, to reduce computational time. The lower temperature response was verified with a similar calculation but with 4 times as many elements, while the higher temperature portion was replicated with sufficient accuracy using a superelastic model from Chapter II.

The undulations in the loading path of the superelastic response were observed in Chapter II as well, but are exaggerated here because of the scaling in the plotting axes. Initially the specimen deforms in a uniform configuration (see Figure 4.11, instance 11). However the structure soon departs from the principal solution and the deformation localizes at top row of cells (see Figure 4.11, instance 12). It should be noted that, as was the case in Chapter II, the principal path was abandoned without the need of introducing imperfections in the model. The presence of internal variables introduces numerical imperfections that are sufficient to drive the solution along a bifurcated path. Finally, at higher macroscopic strains, the response reattaches to the principal path (see Figure 4.11, instance 13).

A similar behavior is observed in the low temperature loading path (Figure 4.9). Even the disappearance of the deviation from the homogeneous solution at high macroscopic strains is repeated here. The transformation during heating is occurring with a homogeneous deformation mode for the honeycomb (Figure 4.10).

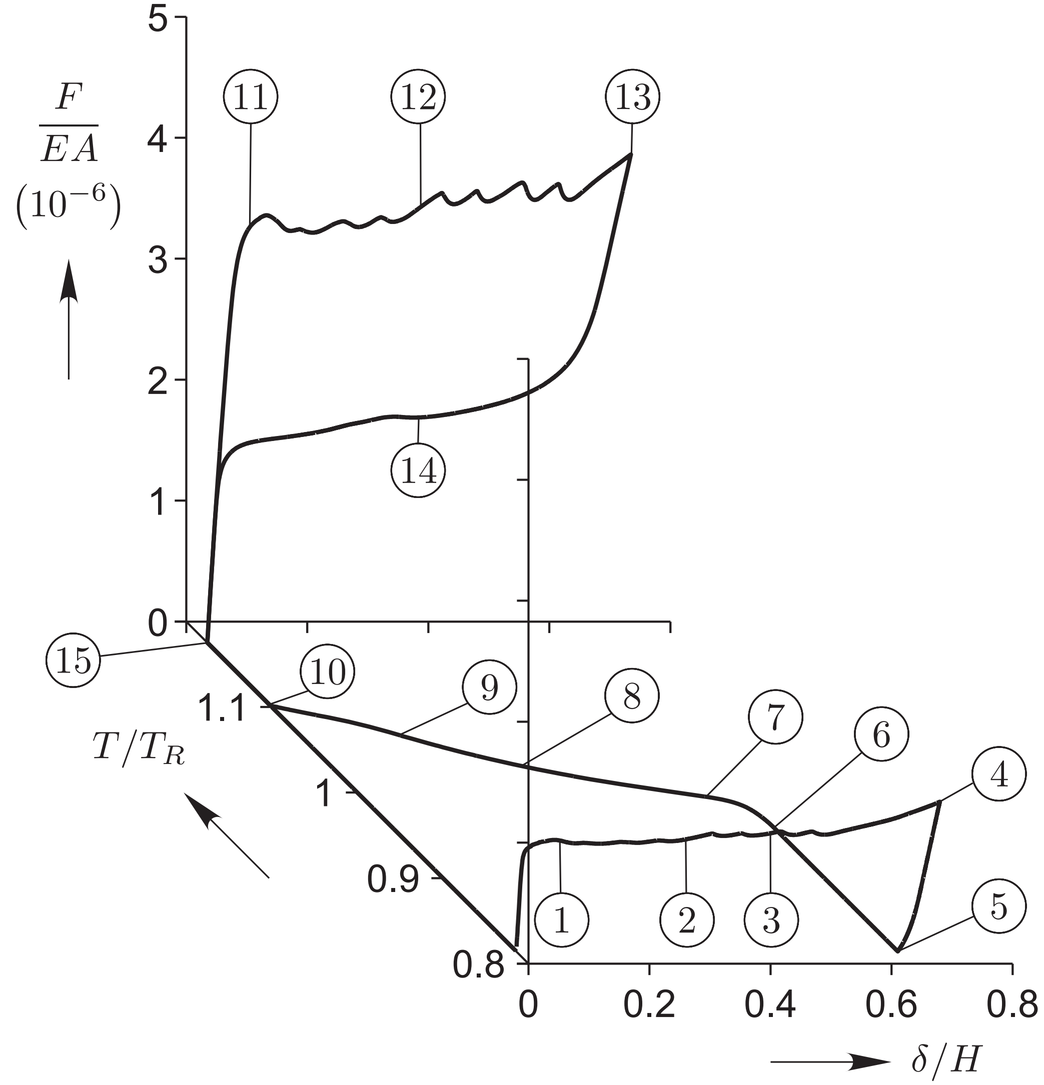

Figure 4.8: Shape memory effect and pseudoelastic response for a $4 \times 7\frac{1}{2}$ hexagonal honeycomb. Numbered tags appearing in figure correspond to instances were the honeycomb's deformed configuration is depicted (see Figures 4.9– 4.11).

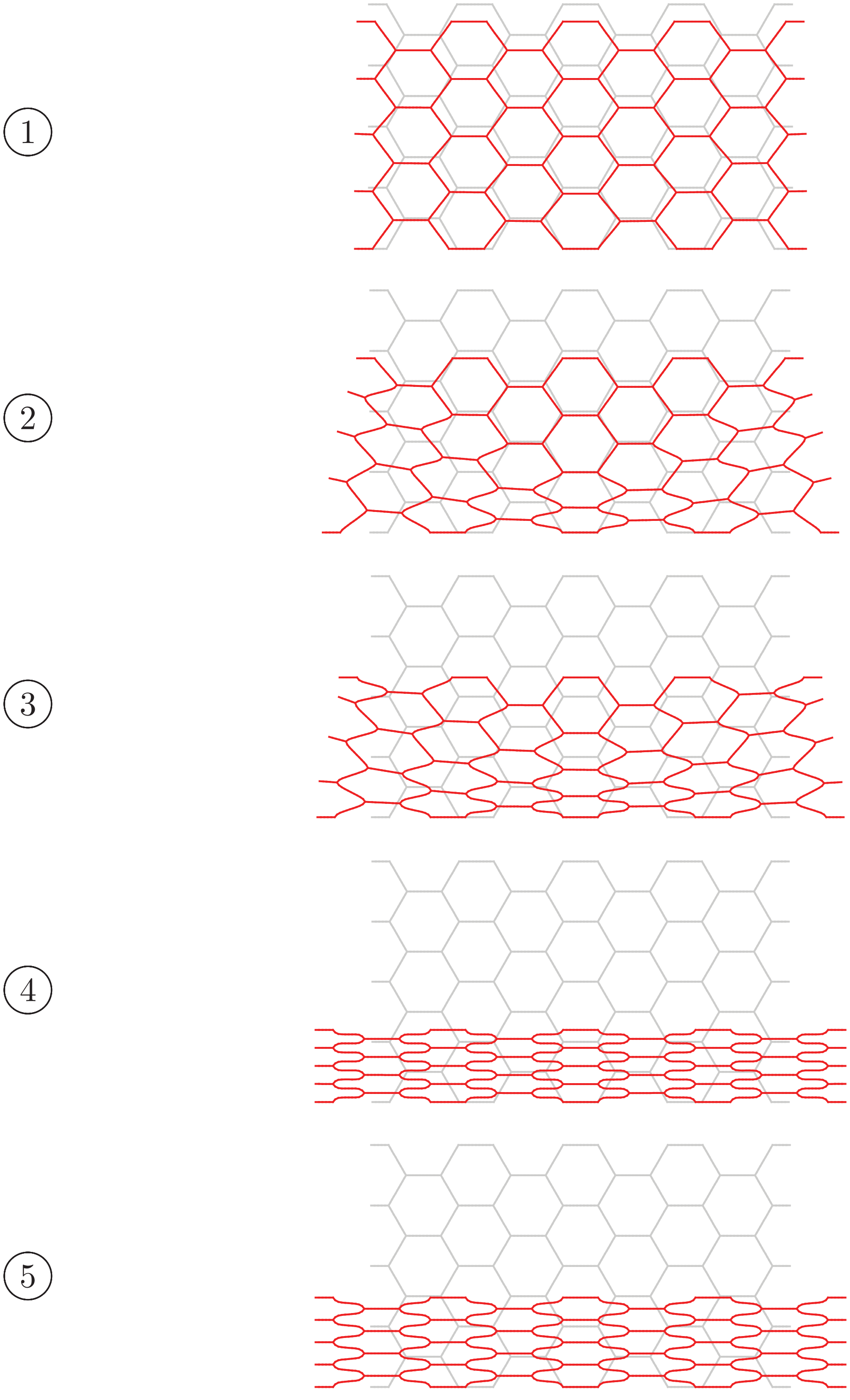

Figure 4.9: Honeycomb deformed configurations for instances 1–5, as these are defined with numbered tags in Figure 4.8.

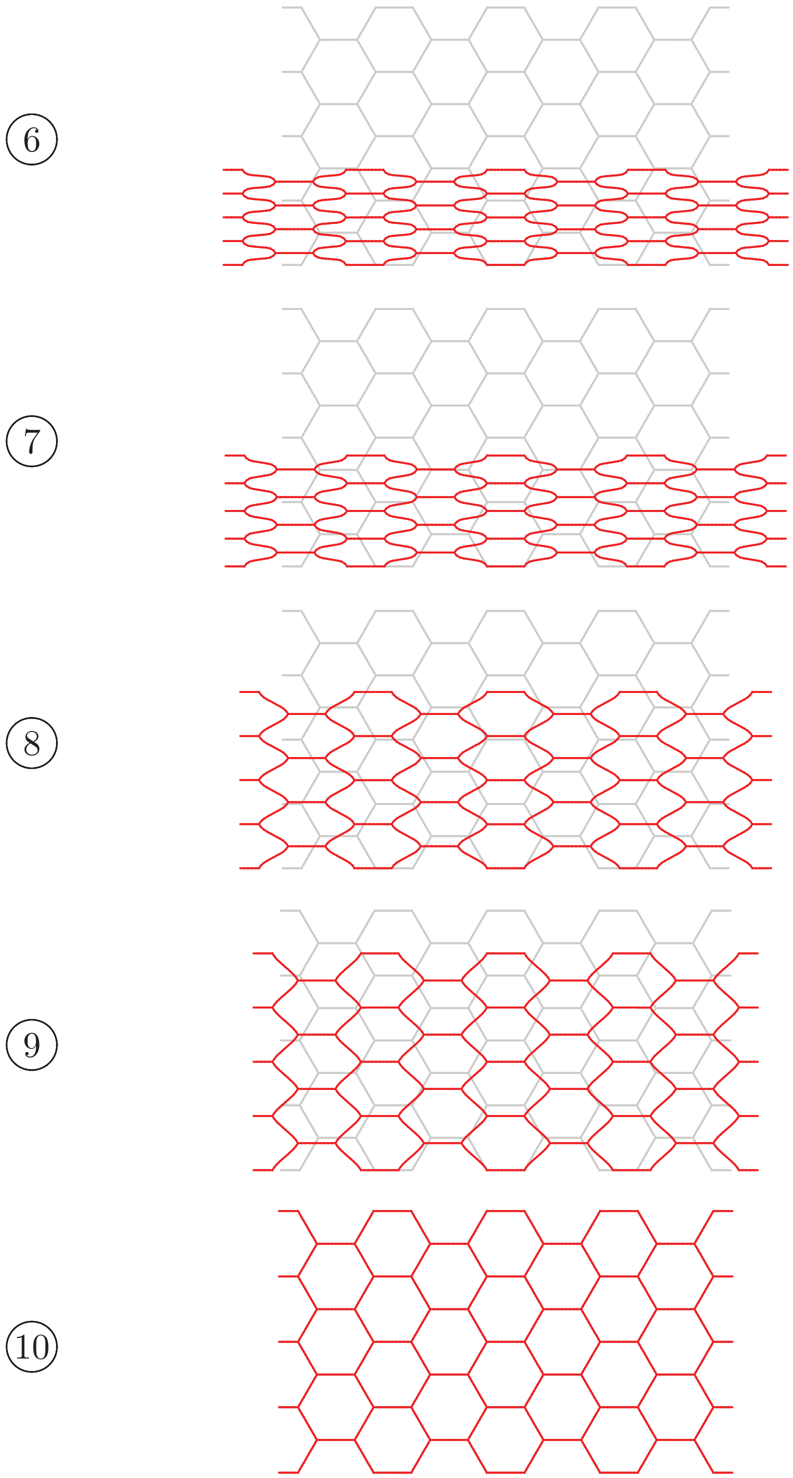

Figure 4.10: Honeycomb deformed configurations for instances 6–10, as these are defined with numbered tags in Figure 4.8.

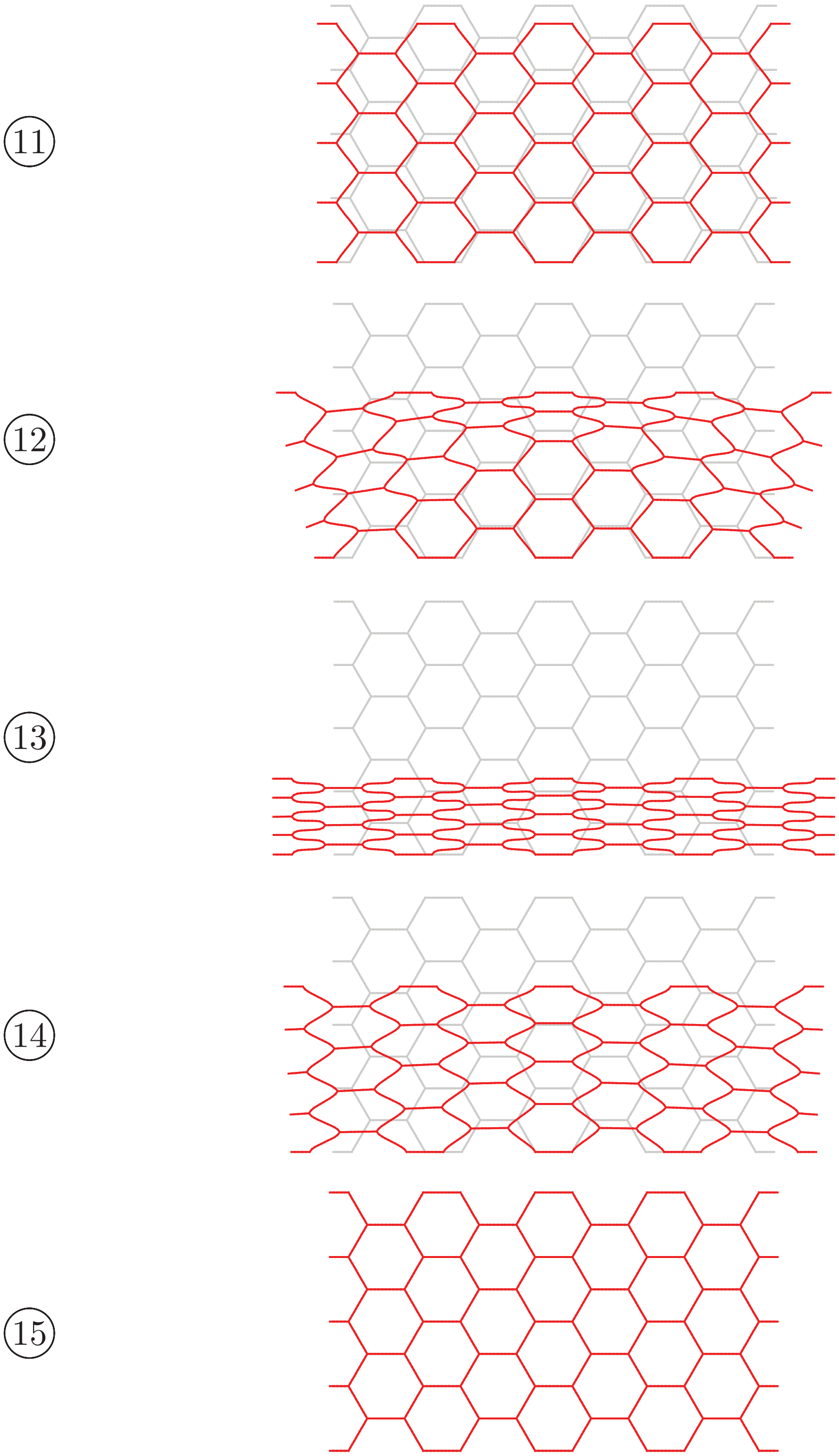

Figure 4.11: Honeycomb deformed configurations for instances 11–15, as these are defined with numbered tags in Figure 4.8.

# Chapter V

# Summary and Conclusions

The recently discovered method for bonding NiTi strips has enabled the fabrication of thin-walled SMA honeycomb, enhansing the shape memory and superelastic properties of the material. The high surface area per mass cellular architecture results in remarkable improvement (over the monolithic case) of the macroscopic superelastic and shape memory effect, as recent experiments on SMA honeycomb specimens have shown. In this work, a theoretical framework has been proposed to model the response of SMA honeycombs exhibiting either superelastic or the shape memory effect.

## 5.1 Superelastic Behavior of SMA Honeycombs and Design Considerations

In the first part of this work an in-depth numerical study of the response of hexagonal SMA honeycombs subjected to large macroscopic strain, isothermal compression of varying amplitudes is presented. The load orientation follows that used in recent experiments. Simulation and stability analyses were performed using a standard incremental algorithm in a finite element-based simulation tool with large displacement, small strain (nonlinear) kinematics, and an isothermal superelastic SMA material model. The study showed how key parameters of the local uniaxial constitutive law, such as nucleation strain, phase transformation tangent modulus, and hysteresis amplitude, influence principal responses of the bulk honeycomb (of infinite extent) and finite honeycombs with initially perfect and imperfect geometries. An investigation of the stability of the periodic unit-cell solution for the infinite structure using Bloch waves provided a key to understanding the response of finite size specimens, which showed interesting transitions from regular (almost periodic) deformations to localized cell deformations and then back to regular patterns upon continuous loading (or unloading) paths.

It was found that bifurcation points at the onset $\lambda_c$ and termination $\lambda_C$ of instability, i.e., the critical points of an unstable region in the primary path of the cell-periodic solutions, were associated with long wavelength modes for all cases considered, while intermediate unstable equilibrium points were associated with an array of finite wavelength modes. These rather remarkable potential changes of stability of the macroscopic response — due to the SMA's inherent softening during stress-induced phase transformation and then stiffening upon phase saturation — has important implications, since they can cause equilibrium solutions to deviate from the periodic, or nearly periodic, configurations for significant portions of their loading path.

Also, it has been demonstrated that our simulation tool can be well calibrated to experimental results, using a material model that captures the uniaxial tension-compression asymmetry (necessary to properly capture the dominate bending effects of cell walls) and modeling some frictional effects at the loading platens. Although the local stress-strain response of the parent material was not known, the calibrated material model exhibits some expected features for trained NiTi SMA.

Beside capturing the overall mechanical response, the simulation tool presented has obvious utility to capture deformed configurations to identify worst case stresses/strains. This helps to quantify the local-to-global strain amplification (structural performance) and determine potential failure locations (structural reliability). Such a parameter study has been performed in Chapter III. There it was found that selection of the geometric characteristics of the unit cell can substantially affect the performance of the whole structure. For example, a standard hexagonal honeycomb with $r = \sqrt{3}/3$ and $t/h = 0.04$ can absorb kinetic energy of $W/EV_{mat} = 5 * 10^{-6}$. However a honeycomb with aspect ratio of $r = 1.5$ and $t/h = 0.03$ can improve that figure to $W/EV_{mat} = 7.5 * 10^{-6}$ while keeping the maximum reaction force to the same safe level.

Future work could follow several paths. An altered load orientation may reveal more interesting features of the response and stability properties of the SMA honeycombs. Investigation of other unit cell shapes, like rhombic and corrugated geometries would be another possible research direction. However, in corrugated unit cells, modeling of contact has to be included in the stability calculations when using the Bloch wave method. Combined with a potential material-level properties tailoring, designs that are much more efficient for energy absorption.

## 5.2 Shape Memory Effect in SMA Honeycombs

A 1D constitutive model has been introduced for thermomechanical response of cell walls, based on [4], which allows for modeling of the material's transformation paths. By using this model, in conjunction with cell wall kinematics presented in Chapter II, a finite sized SMA honeycomb's full thermomechanical load cycle has been simulated with the same mesh density used for the superelastic model.

The macroscopic stress-strain response of a simulated finite honeycomb showed that the essential characteristics of the shape memory effect are credibly captured. The high temperature behavior was, as expected, identical to what the superelastic model would predict. The structure soon starts deviating from the principal solution path as the macroscopic strain increases, only to rejoin to it as compression keeps increasing. Qualitatively, the same behavior was observed in the lower temperature loading path. Of course, loading and unloading at low temperatures leaves the honeycomb with some apparent permanent deformation (homogeneous), which is erased as the temperature is increased. Throughout the heating process, the honeycomb's deformation mode remains homogeneous, since the local uniaxial behavior of the material is stable during this process.

It should be noted, though, that the current formulation is constrained to be symmetric in tension-compression and it always has $E_t^{A \to M} > E_t^{M^{+/-} \to M}$. Asymmetry can be easily introduced, but with the current model $E_t^{A \to M} < E_t^{M^{+/-} \to M}$ cannot be achieved without destabilizing the transformation path along some $\boldsymbol{\xi}$ directions.

However, before tackling these problems, a more robust integration of the constitutive equation should be pursued. Future work could include an investigation of the benefits of having an implicit integration method, as well as a subsequent generalization of the model to enable fully tailoring to experimental data.

## Appendix A

# Performance of cells using different metrics

The parameter study presented in ChapterIII is performed using maximization of energy absorption per unit cell's material volume as the goal. Here, results are presented for maximizing absorbed energy per unit overall volume (i.e volume of whole cell, including vacancies of it). These are more useful in space constrained applications.

Incidentally, the results point towards an optimal design that has very similar characteristics to the one suggested from results in Chapter III. Therefore, aiming at high aspect ratios $r$ is almost always beneficial, while, again, the $\theta = +30^\circ$ cell is superior to others.

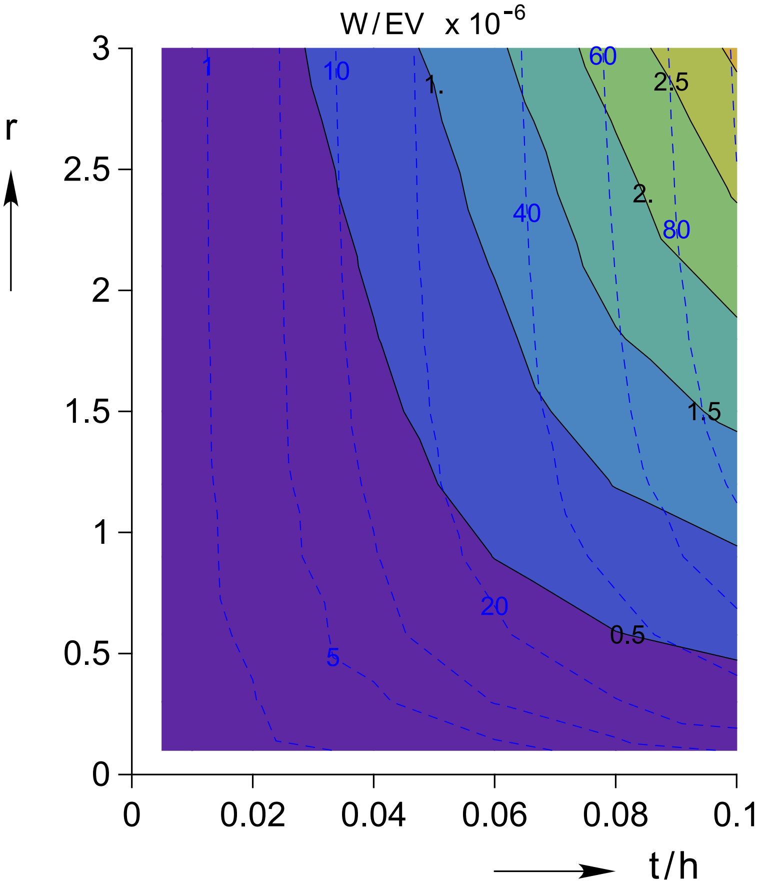

Figure A.1: Design chart with energy absorption per unit volume for cells with $\theta = 15°$. Limiting local strain value of $\varepsilon_{max} = 0.025$ is assumed.

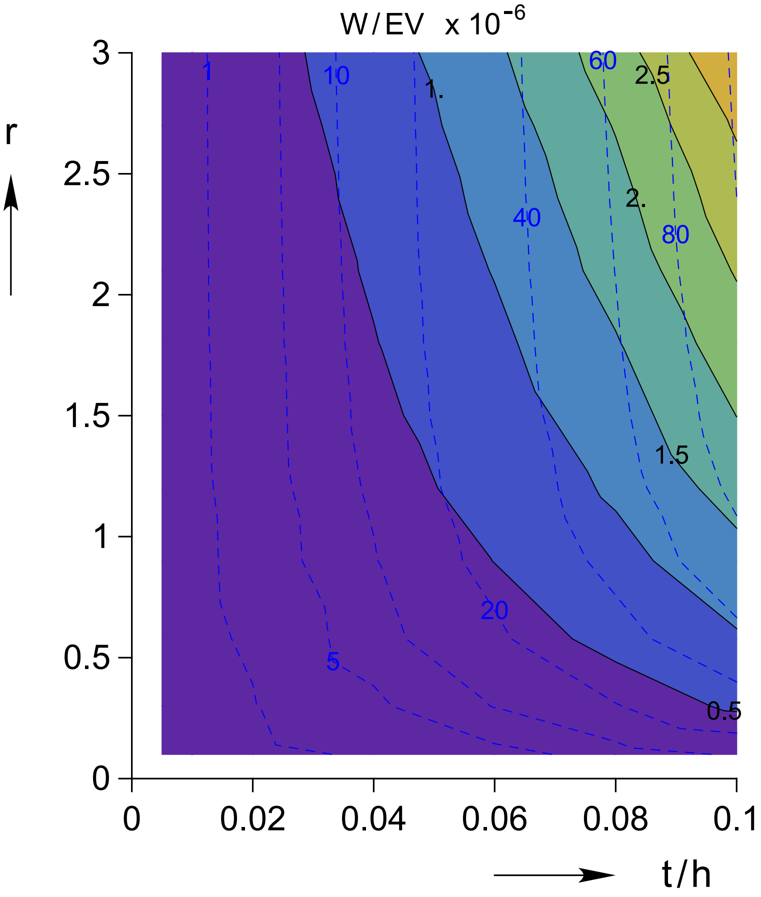

Figure A.2: Design chart with energy absorption per unit volume for cells with $\theta = 15°$. Limiting local strain value of $\varepsilon_{max} = 0.050$ is assumed.

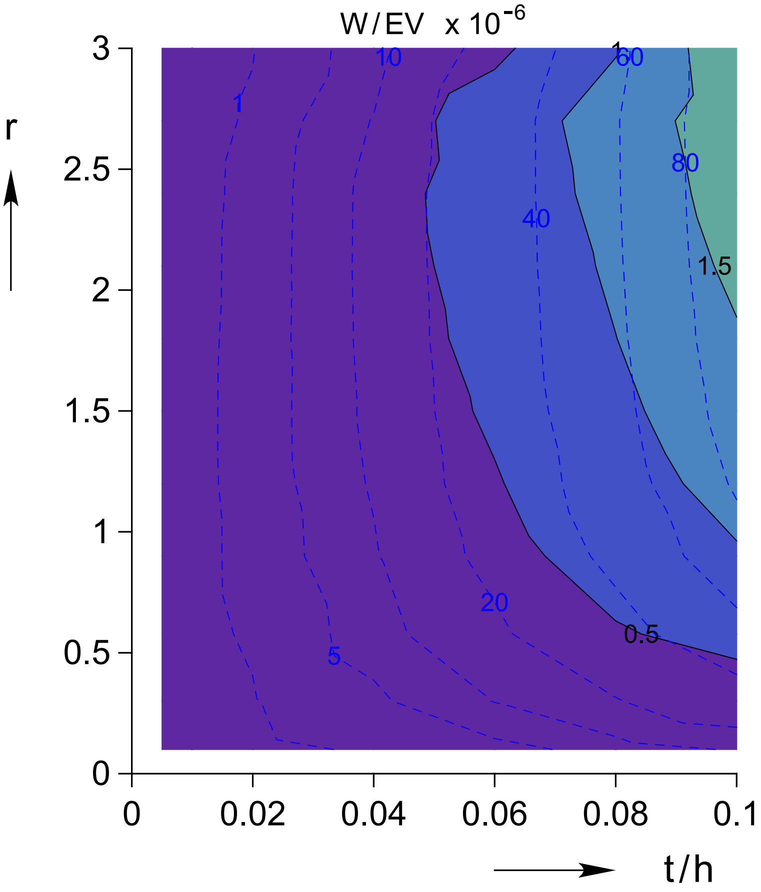

Figure A.3: Design chart with energy absorption per unit volume for cells with $\theta = -15°$. Limiting local strain value of $\varepsilon_{max} = 0.025$ is assumed.

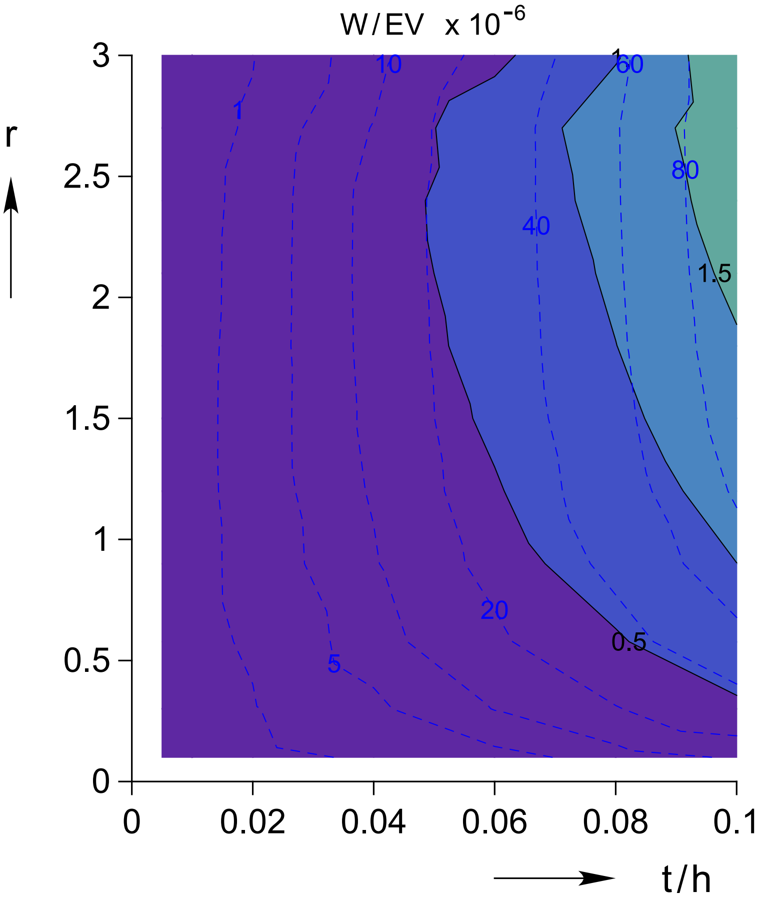

Figure A.4: Design chart with energy absorption per unit volume for cells with $\theta = -15°$. Limiting local strain value of $\varepsilon_{max} = 0.050$ is assumed.

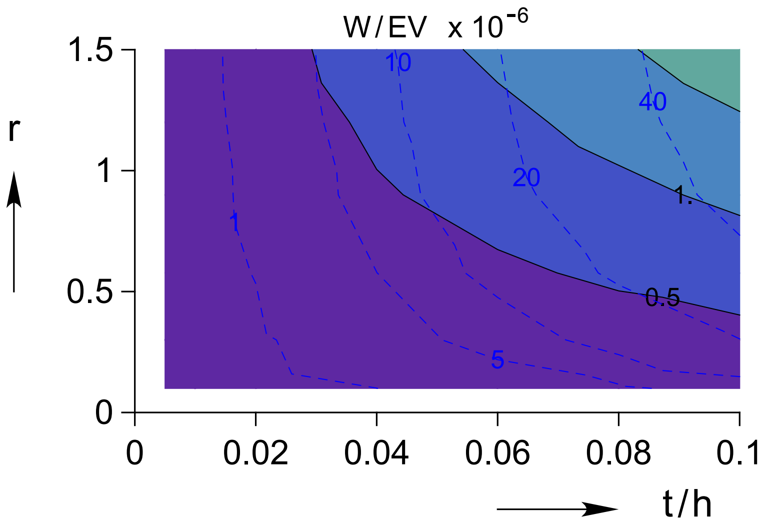

Figure A.5: Design chart with energy absorption per unit volume for cells with $\theta = 30°$. Limiting local strain value of $\varepsilon_{max} = 0.025$ is assumed.

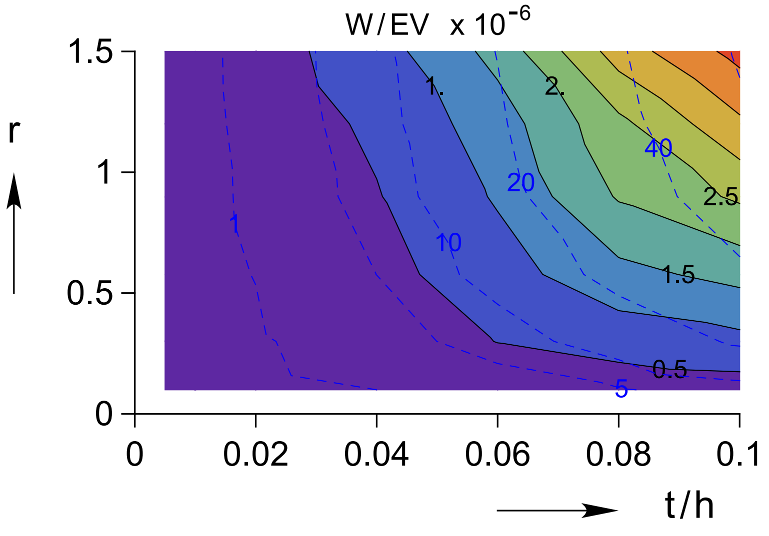

Figure A.6: Design chart with energy absorption per unit volume for cells with $\theta = 30°$. Limiting local strain value of $\varepsilon_{max} = 0.050$ is assumed.

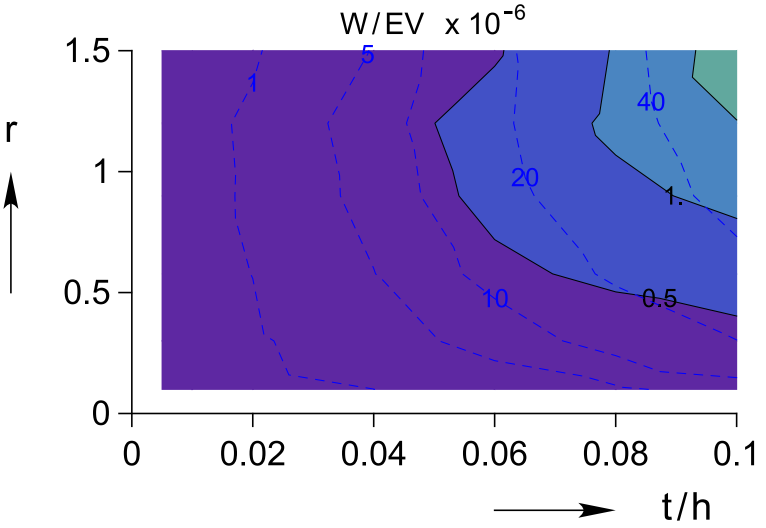

Figure A.7: Design chart with energy absorption per unit volume for cells with $\theta = -30°$. Limiting local strain value of $\varepsilon_{max} = 0.025$ is assumed.

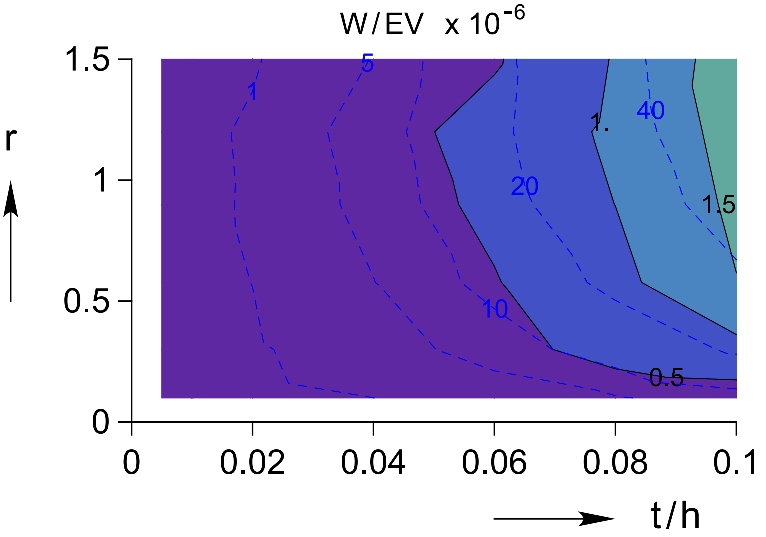

Figure A.8: Design chart with energy absorption per unit volume for cells with $\theta = -30°$. Limiting local strain value of $\varepsilon_{max} = 0.050$ is assumed.

Along with energy absorption, the poisson ratio is of interest. The instantaneous poisson ratio, defined here as the current horizontal expansion over the honeycomb's vertical compression, changes during loading-unloading of the honeycomb. The value at the instance of the critical $\delta/H$ (i.e. the maximum allowable compression of the honeycomb by considering limiting local strain, as well as stability and contact issues, see Chapter III), is plotted in Figures A.9–A.16. This information could be crucial for a multi-functional design or if operation in a confined area is required. For example, by combining two honeycombs with negative and positive poisson ratios, a given ratio (even zero) can be achieved.

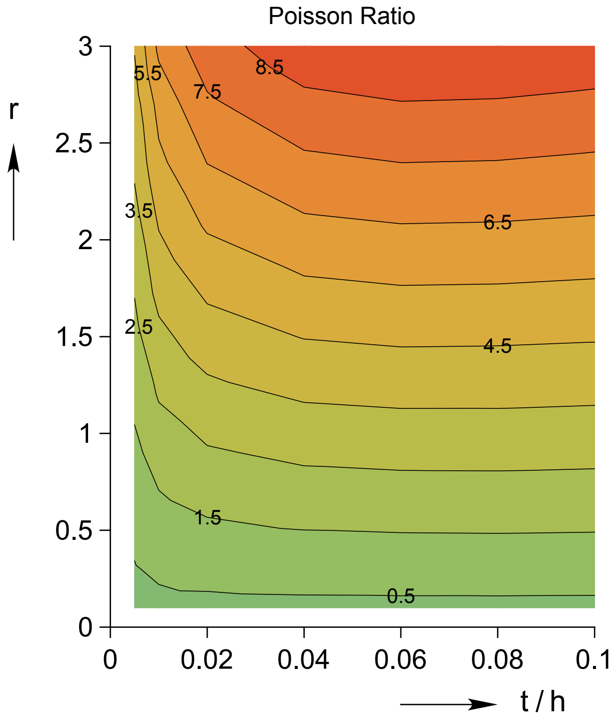

Figure A.9: Design chart with poisson ratio at $\delta/H|_{crit}$ for cells with $\theta = 15°$. Limiting local strain value of $\varepsilon_{max} = 0.025$ is assumed.

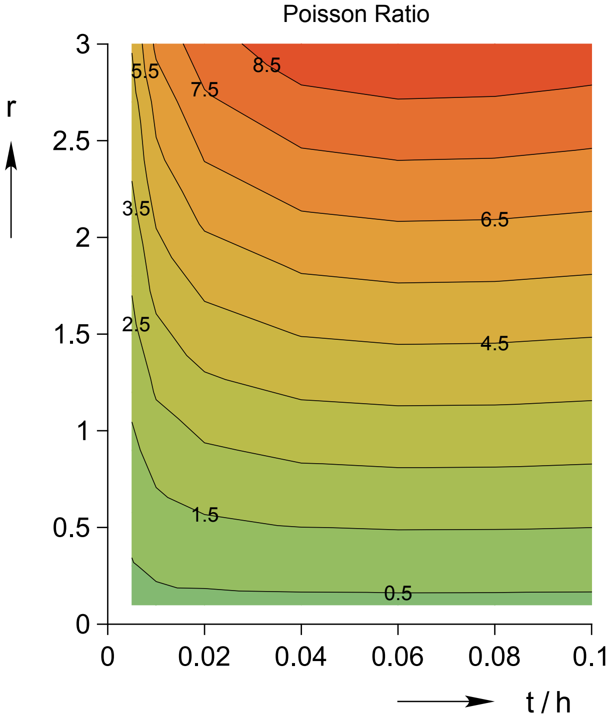

Figure A.10: Design chart with poisson ratio at $\delta/H|_{crit}$ for cells with $\theta = 15°$. Limiting local strain value of $\varepsilon_{max} = 0.050$ is assumed.

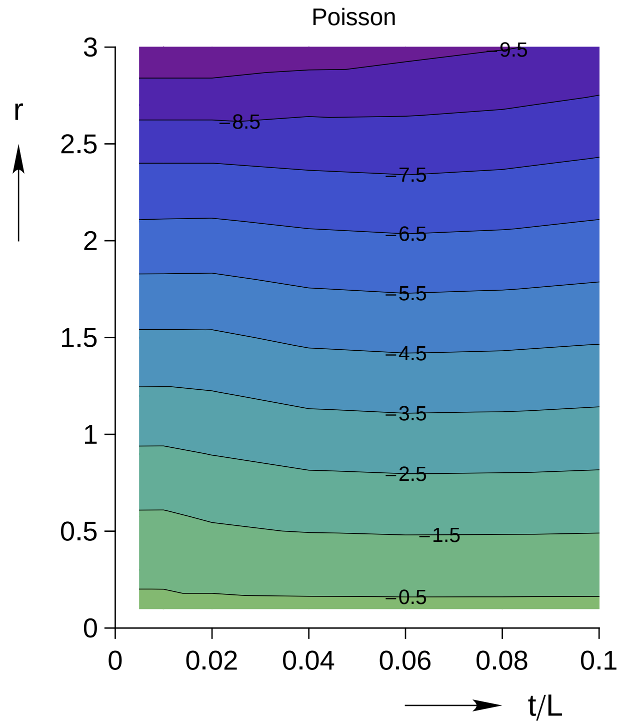

Figure A.11: Design chart with poisson ratio at $\delta/H|_{crit}$ for cells with $\theta = -15°$. Limiting local strain value of $\varepsilon_{max} = 0.025$ is assumed.

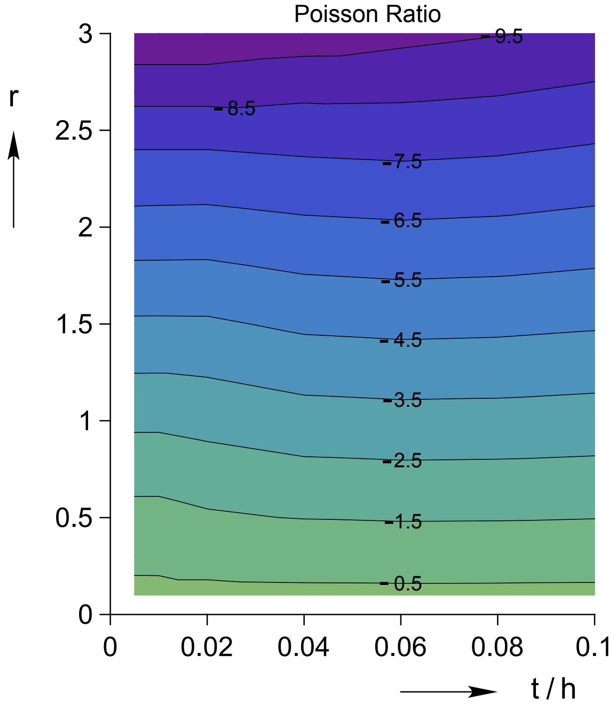

Figure A.12: Design chart with poisson ratio at $\delta/H|_{crit}$ for cells with $\theta = -15°$. Limiting local strain value of $\varepsilon_{max} = 0.050$ is assumed.

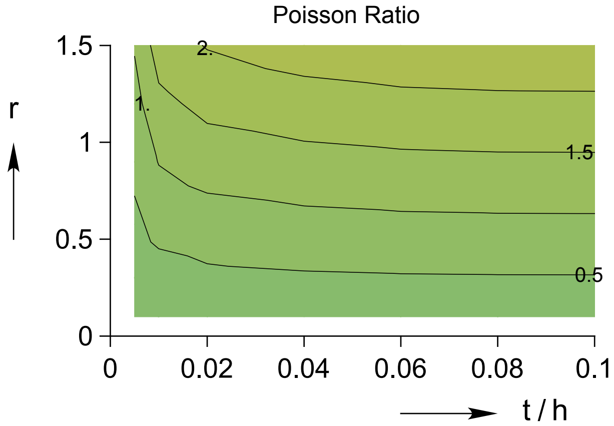

Figure A.13: Design chart with poisson ratio at $\delta/H|_{crit}$ for cells with $\theta = 30°$. Limiting local strain value of $\varepsilon_{max} = 0.025$ is assumed.

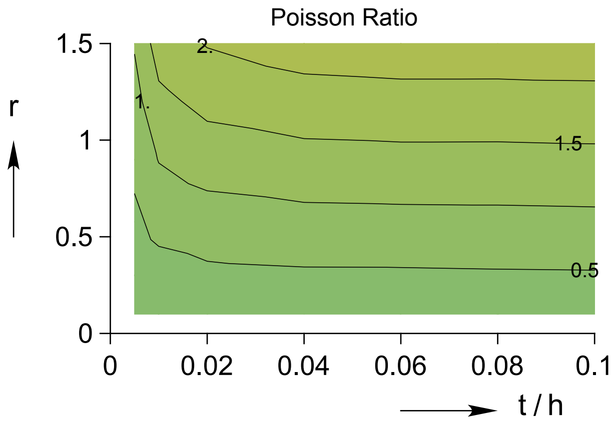

Figure A.14: Design chart with poisson ratio at $\delta/H|_{crit}$ for cells with $\theta = 30°$. Limiting local strain value of $\varepsilon_{max} = 0.050$ is assumed.

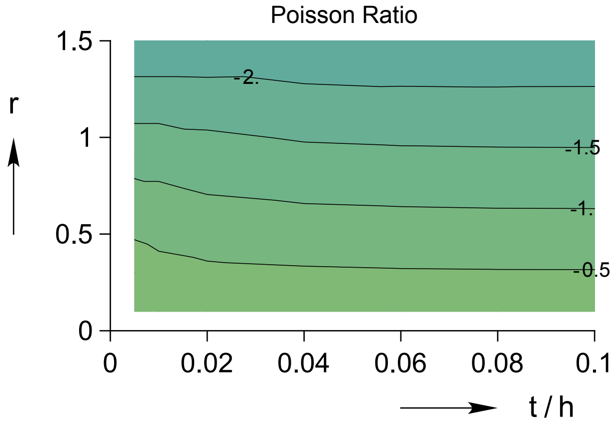

Figure A.15: Design chart with poisson ratio at $\delta/H|_{crit}$ for cells with $\theta = -30°$. Limiting local strain value of $\varepsilon_{max} = 0.025$ is assumed.

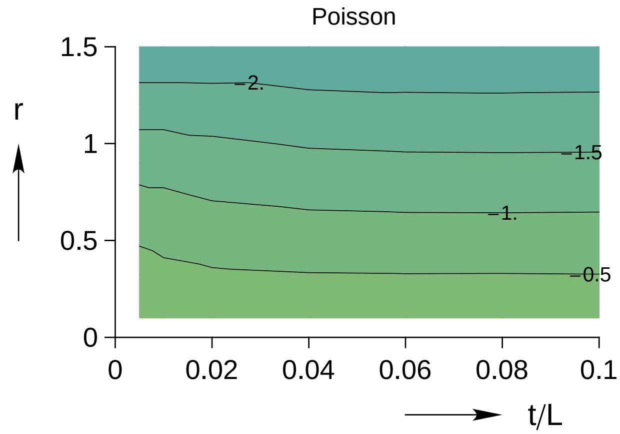

Figure A.16: Design chart with poisson ratio at $\delta/H|_{crit}$ for cells with $\theta = -30°$. Limiting local strain value of $\varepsilon_{max} = 0.050$ is assumed.

# Bibliography

[1] R. Ahluwalia, T. Lookman, A. Saxena, and R. Albers. "Landau theory for shape memory polycrystals.,". *Acta Materialia*, 52:209–218, 2004.

[2] L. Anand and M. E. Gurtin. "Thermal effects in the superelasticity of crystalline shape-memory materials,". *Journal of the Mechanics and Physics of Solids*, 51(6):1015–1058, 2004.

[3] M. Ashby, A. Evans, N. Fleck, L. Gibson, J. Hutchinson, and H. Wadley. *Metals Foams: A Design Guide*, Butterworth–Heinemann, Boston, MA, 1st edition, 2000.

[4] Bi-Chiau Chang, J. A. Shaw, and M. A. Iadicola. "Thermodynamics of Shape Memory Alloy Wire: Modeling, Experiments, and Application,". *Continuum Mech. Thermodynamics*, 18:83–118, 2006.

[5] Bernard D. Coleman and Morton E. Gurtin. "Thermodynamics with Internal State Variables,". *The Journal of Chemical Physics*, 47(2):597–613, 1967.

[6] FEAP, *User Manual*. University of California at Berkeley (Civil and Environmental Engineering) and the University of Michigan (Aerospace Engineering), 7.5 edition, 2005.

[7] Yuval Freed, Jacob Aboudi, and Rivka Gilat. "Investigation of shape memory alloy honeycombs by means of a micromechanical analysis,". *Modelling and Simulation in Materials Science and Engineering*, 16(5):055002 (22pp), 2008.

[8] K. Gall, H. Sehitoglu, Y. Chumlyakov, and I. Kireeva. "Tension-Compression Asymmetry of the Stress-Strain Response in Aged Single Crystal and Polycrystalline NiTi,". *Acta Materialia*, 47(4):1203–1217, 1999.

[9] G. Geymonat, S. Mueller, and N. Triantafyllidis. "Homogenization of Nonlinearly Elastic Materials, Microscopic Bifurcation and Macroscopic Loss of Rank-One Convexity,". *Archive of Rational Mechanics and Analysis*, 122:231–290, 1993.

[10] L. J. Gibson and M. F. Ashby. *Cellular Solids: Structure and Properties*, Cambridge Solid State Series, Cambridge University Press, Cambridge, UK, 2nd edition, 1997.

[11] D. S. Grummon, J. A. Shaw, and A. Gremillet. "Low-Density Open-cell Foams in the NiTi System,". *Applied Physics Letters*, 82(16):2727–2729, 2002.

[12] D.S. Grummon, J.A. Shaw, and J. Foltz. “Fabrication of Cellular Shape Memory Alloy Materials by Reactive Eutectic Brazing Using Niobium,”. *Materials Science and Engineering, A*, 438-440:1113–1118, Nov. 2006.

[13] G. Hall and S. Govindjee. “Application of a partially relaxed shape memory free energy function to estimate the phase diagram and predict global microstructural evolution,”. *Journal of the Mechanics and Physics of Solids*, 50:501–530, 2002.

[14] Mohammed R. Hassan, Fabrizio L. Scarpa, and Nik Abdullah Mohamed. “Shape memory alloys honeycomb: design and properties,”. In Dimitris C. Lagoudas, editor, *Proceedings of SPIE: Smart Structures and Materials 2004: Active Materials: Behavior and Mechanics*, volume 5387, pages 557–564. SPIE, 2004.

[15] R. Hill. “A General Theory of Uniqueness and Stability in Elastic-Plastic Solids,”. *Journal of the Mechanics and Physics of Solids*, 6:236–249, 1958.

[16] X. Huang, G. Ackland, and K. Rabe. “Crystal structures and shape memory behaviour of NiTi,”. *Nat. Mater. Lett.*, 2:307–311, 2003.

[17] M. Iadicola and J. Shaw. “The effect of uniaxial cyclic deformation on the evolution of phase transformation fronts in pseudoelastic NiTi wire,”. *Jounral of intelligent material systems and structures*, 13:143–155, 2002.

[18] M. A. Iadicola and J. A. Shaw. “Rate and Thermal Sensitivities of Unstable Transformation Behavior in a Shape Memory Alloy,”. *International Journal of Plasticity*, 20:577–605, 2004.

[19] D. C. Lagoudas and E. L. Vandygriff. “Processing and characterization of NiTi porous SMA by elevated pressure sintering,,”. *Journal of Intelligent Material Systems and Structures*, 13:837–850, 1997.

[20] B.-Y. Li, L.-J. Rong, X.-H. Luo, and Li Y.-Y. “Transformation Behavior of Sintered Porous NiTi Alloys,”. *Metallurgical and Materials Transactions*, 30A:2753–2756, 1999.

[21] T. J. Lim and D. L. McDowell. “Cyclic thermomechanical behavior of a polycrystalline pseudoelastic shape memory alloy.,”. *Journal of the Mechanics and Physics of Solids*, 50(3):651–676, 2002.

[22] P. A. Michailidis, N. Triantafyllidis, J. A. Shaw, and D. S. Grummon. “Superelasticity and stability of a shape memory alloy hexagonal honeycomb under in-plane compression,”. *International Journal of Solids and Structures*, 46:2724–2738, 2009.

[23] Yoji Okabe, Shu Minakuchi, Nobuo Shiraishi, Ken Murakami, and Nobuo Takeda. “Smart Honeycomb Sandwich Panels With Damage Detection and Shape Recovery Functions,”. *Advanced Composite Materials*, 17:41–56, March 2008.

[24] S. Papka and S. Kyriakides. “In-plane compressive response of crushing of honeycomb.,”. *Journal of the mechanics and physics of solids*, 42:1499–1532, 1994.

[25] J. A. Shaw. “A thermomechanical model for a 1-D shape memory alloy with propagating instabilities,”. *International Journal of Solids and Structures*, 56(5):1275–1305, 1997.

[26] J. A. Shaw, D. S. Grummon, and J. Foltz. “Superelastic NiTi Honeycombs: Fabrication and Experiments,”. *Smart Materials and Structures*, 16:S170–S178, 2007.

[27] J. A. Shaw and S. Kyriakides. “Thermomechanical Aspects of NiTi,”. *Journal of the Mechanics and Physics of Solids*, 43(8):1243–1281, 1995.

[28] J. A. Shaw and S. Kyriakides. “On the Nucleation and Propagation of Phase Transformation Fronts in a NiTi Alloy,”. *Acta Materialia*, 45(2):683–700, 1997.

[29] John A. Shaw, Chris Churchill, Nicolas Triantafyllidis, Petros Michailidis, David Grummon, and John Foltz. “Shape memory alloy honeycombs: Experiments and simulation,”. In *Proceedings of the AIAA/ASME/ASCE/AHS/ASC Structures, Structural Dynamics and Materials Conference*, volume 1, pages 428 – 436, Waikiki, HI, United States, 2007.

[30] N. Triantafyllidis, M. D. Nestorović, and M. W. Schraad. “Failure Surfaces for Finitely Strained Two-Phase Periodic Solids Under Arbitrary Plane Strains,”. *Journal of Applied Mechanics*, 73:505–515, 2006.

[31] N. Triantafyllidis and S. K. Samanta. “Bending effects on flow localization in metallic sheets,”. *Proceedings of the Royal Society of London*, A406:205–226, 1986.

[32] N. Triantafyllidis and W. C. Schnaidt. “Comparison of microscopic and macroscopic instabilities in a class of two-dimensional periodic composites.,”. *Journal of The Mechanics and Physics of Solids*, 41:1533–1565, 1993.

[33] N. Triantafyllidis and M. W. Schraad. “Onset of failure in aluminum honeycombs under general in-plane loading,”. *Journal of The Mechanics and Physics of Solids*, 46:1089–1124, 1998.

[34] Y. Ye, C. Chan, and K. Ho. “Structural and electronic properties of te martensitic alloys TiNi, TiPd, and TiPt.,”. *Phys. Rev. B*, 56(7):3678–3689, 1997.